Characterisation of collisionless shocks in tenuous plasma

Contact *hahmed02@qub.ac.uk*

H. Ahmed, D. Doria, E.Ianni, G. Sarri, R. Prasad,
K. Quinn, I. Kourakis and M. Borghesi
Centre for Plasma Physics, Queen' s University Belfast, Belfast, BT7 1NN, U.K

L. Romagnani
LULI, École Polytechnique, CNRS, CEA, UPMC, route de Saclay, 91128 Palaiseau, France

M.Cerchez, A.L.Lindemann, O.Willi
Institute for Laser and Plasma Physics, University of Düsseldorf, Germany

Introduction

Collisionless shocks are among the most interesting phenomena in plasma physics, since they play a fundamental role in many astrophysical scenarios such as the generation of highly energetic particles and cosmic rays during supernova explosions [1, 2]. There are two possibilities for collisionless shocks formation in unmagnetized plasma; electrostatic shocks [3, 4] and Weibel mediated shocks [5]; As a result of progress in laser technology, now it is possible to replicate the astrophysically relevant conditions in laboratory and the study of these phenomena has received great attention in last decade [2]. The relation of collisionless shocks with other non linear entities (such as ion acoustic solitons (IAS) [4], in acoustic solitary waves [6] and phase space electron-holes [7],etc) also plays a vital role for many astrophysical phenomena [1]. In a laser plasma context, collisionless shocks were observed following the interaction of fast expanding plasma with a solid obstacle. However the observation was carried out employing optical probes, which did not allow to resolve the shock structure and therefore to distinguish between the different possible shock typologies [3]. More recently, collisionless shocks have been observed by employing proton projection imaging (PPI) techniques, which resolve the front with simultaneous measurement of propagation velocity, associated electric field with high temporal and spatial resolution [4,8].

In this report, we present the experimental observation of propagating laser driven electrostatic shocks in tenuous plasma. These shocks are generated by the expansion of warm plasma into a rarefied ionized background [9], and characterized using laser accelerated protons as a charged particle probe [10]. This particular generation scenario has been proven to be of direct relevance to a wide range of possible applications which include laser-driven particle acceleration [12] and inertial confinement fusion [13].

Experimental Setup

The experiment was carried out using the VULCAN laser system at RAL. The schematic of the experimental setup is shown in figure1. The CPA pulse of duration ~1ps, focused by an off axis (f/3) parabola to an intensity ~5x10^{19} W/cm^2, onto 20µm Au target (proton target), is used to produce the proton probe beam. A ~1 ns pulse was focused onto a Au stripe target of thickness 50µm and width 700µm with an incidence of 45° with an intensity ~10^{15} W/cm^2. The set-up was enclosed in a gas cell filled by nitrogen at pressure between 10^{-1}-10^{-4}mbar. The proton imaging technique was the main diagnostic employed to detect and characterize the shock waves propagating in the low density plasma resulting from background ionization. The distance between the proton target and the shock target was l=4 mm and the distance between the shock target and the proton detector was L=3.6cm, giving a projection magnification M=(l+L)/l~10. The proton beam, after having probed the plasma, was recorded on a stack of several layers of dosimetrically calibrated radio chromic Films (RCF). Additionally, Nomarski Interferometry was employed to characterize the laser ablated plasma.

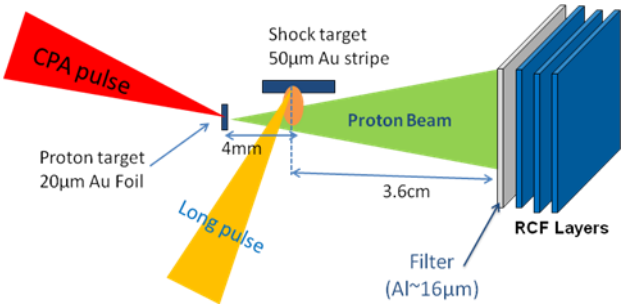

Figure 1: Schematic of the experimental setup.

Results and Discussion

Data exemplifying the features observed by PPI is shown in figure 2. As a rule of thumb the electric fields are directed from the regions of a lighter blue color compared to the background (zones of reduced probe proton flux) towards the regions of darker blue color (increased flux). A pronounced modulation in the probe proton density, revealing a strongly modulated field distribution is observed at ~1mm from the target. This modulation is interpreted as a shock structure propagating in the tenuous plasma. The shock has average radius of curvature ~ 700µm and thickness δR ~ 50-100 µm and expands with approximately spherical symmetry from the target.

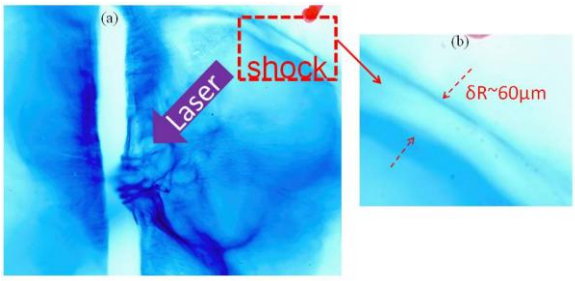

Figure2: (a) Proton Image of the interaction of nanosecond pulse with 50µm thick Au stripe, showing shock structure created by the expansion of laser-ablating plasma into tenuous plasma at 350ps after the interaction. b) Zoom of observed structure.

The observed proton density modulation reveals an electric field which changes sign across the shock [4]. The proton density modulation can be related to deflecting transverse electric field by [8]

$$E = -\frac{(2 \in pM)}{eLb} \times \int {\delta np}/{np}\, dX$$

Where $\delta n_p = n_p - n_{pu}$ with n_p and n_{pu} perturbed and unperturbed density, ε_p is the proton energy, M is the magnification, L is the distance between interaction region and detector; and b is the region of non zero charge density crossed by protons given by $b = 2[(R + \delta R/2)^2 - R^2]^{1/2}$ with R the radius of the structure and δR its thickness. The proton density modulation profile is shown in figure 3(a) and the electric field profile at the shock front is shown in figure 3(b), having amplitude 3×10^7 V/m. We interpret the data within the framework of the nonlinear wave description based on the KdV equation.

$$\partial_t u + u\partial_x u + \beta \partial_{xxx} u = 0$$

The second term on the left hand side is associated with nonlinearity, which causes wave steepening and the third term is associated with wave dispersion. The competing action of nonlinearity and wave dispersion leads to the formation of IAS. The proton density modulation and electric field profiles of IAS predicted by KdV equation [4], are in qualitative agreement with the experimentally observed profiles shown in figure 3(a) and (b).

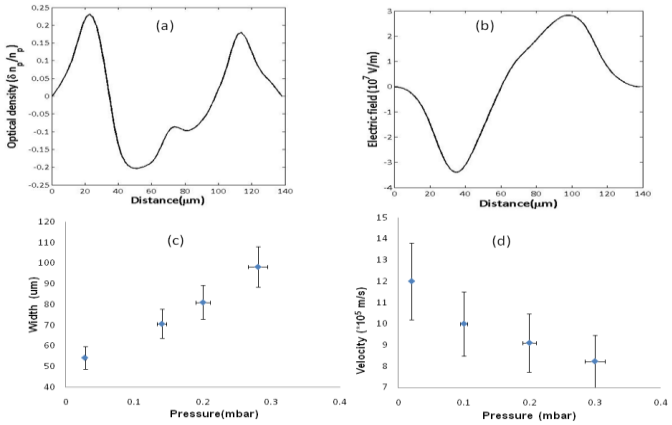

Figure 3: (a) Proton density line out across the ion acoustic soliton (IAS) (b) reconstructed electric field associated with shock structure, (c) Variation of velocity and (d) the width versus the tenuous plasma pressure.

We note that the observed shock structure must be collisionless and is likely to be nonmagnetized. It has recently been shown that the presence of rarefied background plasma can forbid magnetic field generation, leading to a purely electrostatic evolution of the plasma, and to an electrostatic shock at the expanding plasma front [10]. In order to verify whether the shock is collisionless, we estimated the various particle mean free paths in the background plasma and compare them to the measured shock front widths. In order to do so, it is assumed that the background gas (nitrogen) is fully ionized, and ion charge state to be Z=7 and the ion mass (in units of proton mass) to be μ=14. For mean free estimations we use the highest experimental pressure employed i.e 3×10^{-1}mbar. At this pressure, the ion and electron density are $ni \sim 1.5 \times 10^{16}$cm^{-3} and $ne \sim Zni \sim 1 \times 10^{17}$cm^{-3} respectively. An electron temperature can also be estimated from the balance of the electrostatic and thermal energy of the electrons in the shock, giving $k_B T_e \sim e\,E\,(\delta R/2) \sim 1$ keV. Using these estimations, the electron-electron, electron-ion, and ion-ion mean free paths are of several cm or more and, therefore, are much larger than the shock width which is in the range $\delta R \sim 50$–100μm, ruling out the possibility that the observed shocks have a collisional character [4].

The time of flight arrangement of proton probing resulting from a multilayer RCF detector and the broad spectral content of the proton beam provided multi-frame capabilities of the proton probing within a single laser shot. The proton probing timing can be calculated by

$$\tau = \tau_o + \left[\frac{l}{c} \times \left(\frac{2\,\epsilon_p}{m_p c^2}\right)^{-1/2}\right]$$

Where τ_o is the optical delay between the two laser pulses, ε_p and m_p are the energy of protons and mass of proton respectively. Thus proton beams will cross the interaction area at different times and, the shock propagation velocity can therefore be measured in a single laser shot, as different shock front position in consecutive RCF layers will be observed, corresponding to different probing times.

As an example, the shock structure moves with 8×10^5m/sec at 0.3mbar pressure of the ambient gas, with the velocity varying for different pressures (i.e different plasma density when ionized). The variation of velocity versus the background pressure is shown in figure 3(c). The shock velocity decreases as the background plasma pressure is increased. As the PPI technique resolves the shock front, the width of the shock structure can also be measured. The width of the shock also varies with the background plasma pressure as shown in figure 3(b), decreasing with the increase of background pressure. The relation between the shock velocity and its spatial width is in agreement with the theoretical interpretation of IA KdV solitons (i.e. narrower solitons are faster and vice versa)

Due to the qualitative agreement of theory and observations, in addition to correlation between velocity and width variations, it is inferred that the observed excitations are ion-acoustic shocks.

In some shots at the highest pressures employed, the shock front displayed periodical modulations, which points to the development of an instability. While the interpretation of this data is still ongoing, it is interesting to note the qualitative resemblance with situations found during the development of supernova remnants [2]. Among the possible causes for the development of the instability, we are currently considering Rayleigh-Taylor (RT) or the effects of an increased dispersion in the tenuous plasma, which can cause imbalance in competing action of nonlinearity and dispersion.

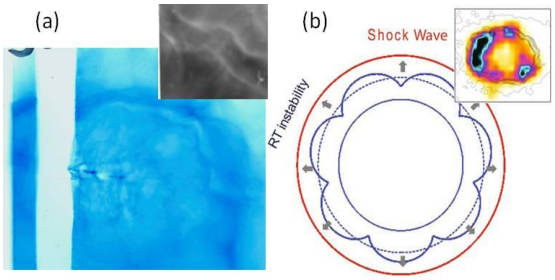

Figure 4: (a) Proton radiograph of an ion acoustic soliton, RT Instability in the soliton front at ~1mm from the focal spot is clear and the inset shows a zoom-in view of the instability front (b) Schematic view of the shock waves and in the inset: X-ray and optical image of supernova remnant SNR extracted from [2].

Conclusions

The electrostatic shock launched by the expansion of dense plasma into tenuous plasma, has been observed and characterized by means of the proton projection imaging technique. The employment of the proton projection imaging allows the simultaneous measurement of the spatial profile, electric field distribution and propagation velocity of a shock with a high temporal (~ps) and spatial (~μm) resolution. The shock width and velocity variation as a function of the background gas pressure has been observed. The reconstructed electric field profile qualitatively agrees with the theoretical predicated pattern of IAS.

Acknowledgements

We acknowledge support of the CLF beam access funding from STFC. We also acknowledge the support from AWE plc and the ELI project.

References

1. R.Z.Sagdeev and C.F.Kennel., Sci.Am.264, 106 (1991).
2. B. A. Remington et al., Science, 284, 1488 (1999); S.V. Bulanov et al., Eur. Phys. J.D.555, 483 (2009) ; Y. Uchiyama et al., Nature (London) 449, 576 (2007).
3. A.R. Bell et al., Phys. Rev. A. 38, 1363 (1998).
4. L. Romagnani et al., Phys. Rev. Lett. 101,025004 (2008).
5. Y. Kuramitsu et al., Phys. Rev. Lett. 106, 175002 (2011).
6. H. Washimi and T. Taninti et al., Phys. Rev. Lett. 17, 996 (1966).
7. G. Sarri et al., Phys. Plasmas, 17, 010701 (2010).
8. G. Sarri et al. New J. Phys. 12 ,045006 (2010).
9. S.O.Dean et al., Phys. Rev. Lett. 27, 487 (1971).
10. M. Borghesi et al., Plasma Phys. Control. Fusion, 43, A267 (2001); M. Borghesi et al., Plasma Phys. Control. Fusion, 50, 124040 (2008); L. Romagnani et al., Laser Part.Beams, 26, 241 (2008).
11. G.Sarri et al. PRL, 107,025003 (2011).
12. P. Mora, Phys. Rev. Lett. 90,185002 (2003).
13. M.Tabak et al., Phys. Plasmas, 1,1626 (1994).

The effect of using multiple laser pulses on the angular distribution of laser accelerated proton beams.

Contact *ceri.brenner@stfc.ac.uk*

C. M. Brenner*, D. C. Carroll, M. N. Quinn, P. McKenna

SUPA, Department of Physics,
University of Strathclyde,
Glasgow, G4 0NG, U.K.

K. Markey, K. L. Lancaster, A. P. L. Robinson, J. S. Green, D. Neely,

**Central Laser Facility, Rutherford Appleton Laboratory,*
Didcot, OX11 0WX, U.K.

M. Gunther, K. Harres, F. Nurnberg, M. Roth

Institut fur Kernphysik, Technische Universitat Darmstadt,
64289 Darmstadt, Germany

S. Kar, M. Zepf,

School of Mathematics and Physics, Queen's University Belfast,
Belfast, BT7 1NN, U.K.

Introduction

Research into laser driven proton acceleration has been a very active area of laser plasma physics ever since the first observations of MeV proton beams produced using the interaction of an intense laser pulse with a solid foil target were reported just over a decade ago [1-3]. Since then, a great deal of effort has gone into understanding the acceleration mechanisms, with the view that one can optimise and control this interaction through careful selection of the target and laser parameters. Signature qualities of laser accelerated proton beams which make them markedly different from conventionally sourced proton beams include ultra-short pulse duration (ps), high single shot brightness (~10^{11} protons per bunch) and small source size (~ μm). These qualities mean that laser accelerated protons are well suited for applications such as proton heating [4-6], radiography [7] and probing of electric fields [8] for example. However, qualities such as the proton flux and angular distribution need to be improved upon before these, and other, applications can be fully realised.

Reported here are the results of an experimental campaign in which two, relativistically intense laser pulses are incident on a solid foil with a very fine temporal separation of a few picoseconds. Encouraged by previous numerical investigations [9] of double-pulse laser acceleration of protons, which predict a significant enhancement in the proton flux and thus laser-to-proton conversion efficiency, we investigated this technique experimentally using the Vulcan laser system in double-pulse mode [10].

For the laser intensities used in this campaign, Target Normal Sheath Acceleration (TNSA) [11] is considered to be the dominant mechanism behind the acceleration process. Upon interaction with a pre-formed plasma on the front surface of a target foil, the large electromagnetic fields of the laser pulse act to accelerate electrons up to relativistic energies into the target. A charge separation exists as soon as some of those electrons penetrate through to the rear surface of the target foil, leaving behind a strong, electrostatic sheath field (TV/m) which then ionises the atoms and accelerates the ions on the rear surface up to multi-MeV energies over micron scale lengths. Double-pulse acceleration is an advanced form of TNSA, in that it relies on the same principle of sheath formation and acceleration of ions from the rear surface.

The first pulse is intense enough to initiate multi-species TNSA from the rear surface. Repulsion between the carbon front and the protons in its vicinity results in a modulation of the proton phase space in the plasma expansion at the rear of the target. A structure is formed in the proton population which is made up of a dense region of slower protons sitting behind an exponentially decreasing distribution of higher energy protons. The second pulse drives an increase in the hot electron temperature and 1D PIC simulations [10] have shown that the strongest accelerating field is generated at the interface of the two proton density layers, thus leading to the formation of a rarefaction wave as protons in the slow dense layer surge forward.

Commonly, sheath accelerated protons beams can be characterised as having a centrally peaked dose distribution, with an almost Gaussian-like drop off in proton flux in the wings of the beam, thus leading to strong variations in proton dose across the delivered beam [12,13]. This compares badly to the top-hat dose profile of conventionally sourced proton beams, which is far more desirable for most applications. We report here on how, along with enhancement of the laser-to-proton conversion efficiency (as reported by Markey et al [10]), the double-pulse acceleration technique can also be used to improve and change the distribution of the proton beam in the detector plane.

Experimental set-up

The experiment was performed using the 1054 nm, petawatt arm of the Vulcan laser system at the Central Laser Facility, Rutherford Appleton Laboratory. A plasma mirror [14] was used in order to increase the nanosecond laser contrast to better than 10^{-8}, which was necessary to ensure that pre-plasma formation on the front surface of the target was negligible before the arrival of the first pulse. The focusability of the laser spot after the plasma mirror degrades over the pulse separations of the delays used here, and so to preserve the intensity ratio the focal spot was defocused away from tight focus.

The Vulcan laser system was set-up to generate double pulses with temporal separations of a few picoseconds. This was achieved with the introduction of a half-wave plate and polarizing beam cube into the beam between the picosecond and the nanosecond stretcher. The orientation of the half-wave plate was used to control the intensity ratio between the first and second pulse. Both pulses were retro-reflected using roof prisms, with one of these mounted on a translation stage in order to introduce a controllable, temporal delay into the double pulse structure. The polarisations of the pulses were then matched before being brought onto the same alignment using a non-polarising cube. By interfering the 100 fs pulses from the seed oscillator and observing the interference, the zero position of the relative path length between the two pulses was established to within 50 fs.

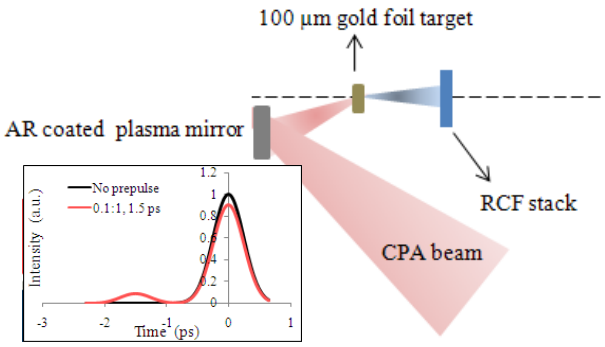

Figure 1: Schematic of the experimental arrangement showing the main diagnostic used. A plasma mirror was incorporated into the setup in order to produce a high contrast laser pulse. The incident angle of the laser onto the target was 40° to the target normal and the RCF stack was positioned 35 ± 1 mm from the target foil, centered to the laser axis height. Inlaid is the single pulse intensity profile and an example of a double pulse profile with a delay of 1.5 ps.

Laser pulses of duration ~700 fs and intensity ratio, $I_{initial}$: I_{main}, of 1:10 were delivered on to target containing a total energy (regardless of the time delay) of ~130 J. The beam was focussed onto the target at 40° incidence, in p-polarised geometry.The area of irradiation was increased to ~ 30 µm so as to lower the effective intensity on target with the intention of decreasing the maximum energy of the accelerated proton beam to within the energy region of interest (5-25 MeV) whilst maintaining the maximum laser energy available for absorption. Therefore, the intensity of the initial pulse was ~ 3.2 x 10^{18} W/cm^2, yielding a peak intensity of ~ 2.9 x 10^{19} W/cm^2 in the main drive pulse.

Planar, gold foil targets of thickness 100 µm were irradiated using a temporally shaped laser intensity profile with delays (t_{delay}) of 0 ps, 0.75 ps, 1.5 ps and 2.5 ps between the pulses. The beams of accelerated ions were compared using a suite of diagnostics, which included Thomson parabola ion spectrometers, however the main diagnostic employed to record the dose delivered by forward accelerated proton beams was a stack of radiochromic film (RCF). The 50 mm x 50 mm RCF stacks were centered along the target normal axis and positioned 35 ± 1 mm from the target. A slot was machined into the RCF films to allow a clear path through which particles could pass and then be sampled by ion spectrometers which sat behind the RCF stack. This diagnostic was designed to provide information on the angular and energy distribution of the proton beam within the energy region of interest and as such, the majority of the results reported here have been obtained using the RCF stacks.

Results

Example radiochromic film pieces, irradiated by the proton beams produced using the double-pulse technique with varying delays between the pulses, are shown in figure 2. Features common to all of the proton beams generated under this regime of double pulse laser acceleration include a maximum proton energy of approximately 14 MeV (± 2 MeV depending on the pulse separation) and an exponentially decreasing proton dose spectrum, as described in Markey et al [10]. A proton spectrum extracted from a stack of RCF will give the integrated dose, for each proton energy bin, deposited across the film. However, another important quality of the beam that is easily extracted from the RCF stacks is the angular distribution of the proton beam dose.

Initial analysis of the footprint left by the proton beams in the RCF (see figure 2), suggests that the improvement in the overall dosage in the beam when using the double pulse technique is not the only effect. For shots taken with a double pulse profile, one observes a smoothing of the dose deposition across the diameter of the beam accompanied by a steadier decrease in the proton beam width with proton energy as compared to the single pulse (t_{delay} = 0 ps) case. This effect is particularly significant when a 0.75 ps delay between the pulses is employed (see figure 2).

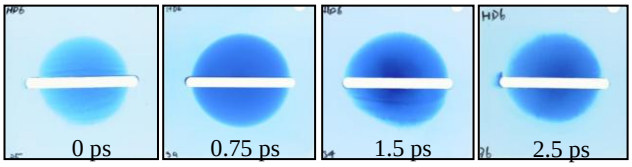

Figure 2: Example pieces of RCF irradiated with a proton beam produced by using (left to right) the single pulse and the double pulse technique with temporal separation of 0.75 ps, 1.5 ps and 2.5 ps respectively, with a 100 µm thick Au foil target. The proton energy that this piece represents is 7.3 ± 0.2 MeV.

Within a typical laser accelerated proton beam, the angular envelope of the protons tends to decrease with increasing proton energy [1,15,16]. This is a consequence of the combination of Liouville's theorem applied to a beam of particles and that, in the framework of the TNSA mechanism, the highest energy protons are accelerated when the sheath field is strongest, which coincides with when the emission area is a minimum [16,17]. However, because the protons are accelerated normal to the contours of the sheath [18], it also follows that the trajectory of the protons, and hence the spatial profile of the beam, is heavily dependent on the shape of the sheath and its evolution during the acceleration process. One can observe the effect of a change in the sheath shape by measurement of the proton beam divergence with proton energy. To illustrate the effect of using the double pulse technique on the divergence of the entire proton beam, a plot of the half-angle width of the proton beam against proton energy has been produced for both data sets (see figure 3).

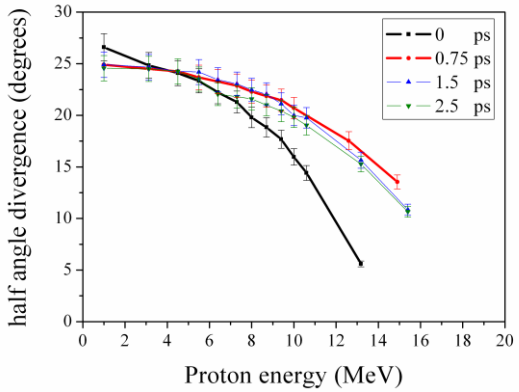

Figure 3: Half angle envelope divergence of the beam plotted against proton energy. The corresponding delay between the pulses is given in the legends.

Comparing the shape of the divergence graphs for that of a single pulse (highlighted in black) with the optimum double-pulse delay for angular distribution (highlighted in red), one can see that with a double pulse, the decrease in the half angle width of the beam is at a much slower rate. For proton energies up to

10 MeV, an almost plateau-like region emerges in the divergence when a double pulse is employed, before dropping off steadily, to approximately half the initial width of the beam. Between proton energies of 1 MeV < E_p < 10 MeV, the half-angle width decreases by 40 ± 5 % when a single pulse is employed. Whereas when a double pulse is employed, it only decreases by 16.9 ± 8.0 % at a pulse delay of 0.75 ps. Furthermore, the width of the higher energy component of the beam is significantly larger than when a single pulse is employed. In each instance of using a double pulse, the beam width has increased significantly for energies more than 10 MeV and has more than doubled for proton energies more than 12 MeV.

Examining the spatial profile of the beam in more detail, line-outs of the dose maps for the proton beams were taken in order to compare the dose distribution across the beam that results from the single pulse acceleration technique and the double pulse acceleration technique (see figure 4).

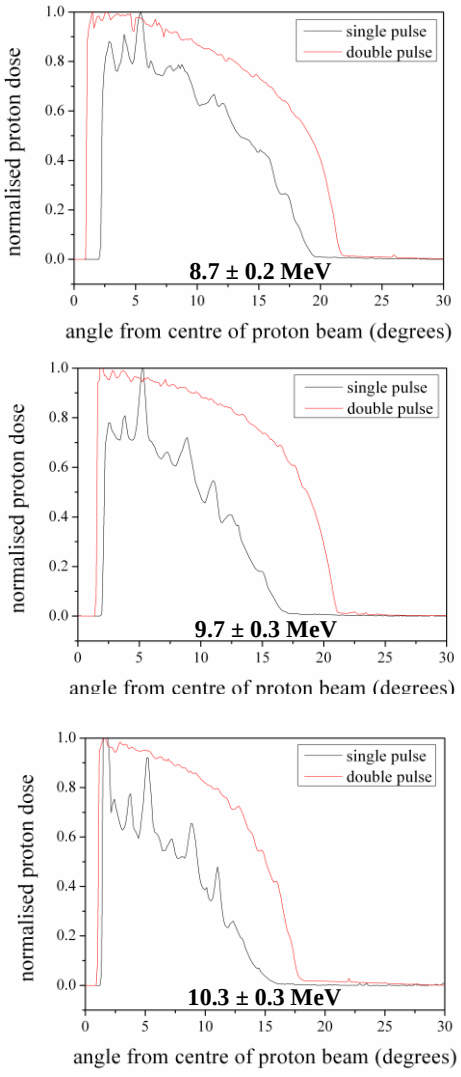

Figure 4: Normalised dose map profiles for three energy bands, taken from proton beams produced using a single pulse and a double pulse with delay of 0.75 ps.

For each energy band shown, the double pulse accelerated proton beam dose profiles contained at least twice as much proton dose, therefore normalised dose profiles have been presented, so that the distribution of the proton dose across the beam is more easily compared. The profiles were extracted from the top half of the beam, above the machined slit, as seen in figure 5 and the 0° point was taken as being the centre of the beam.

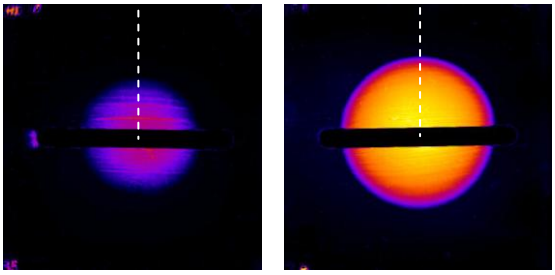

Figure 5: Example dose map images for single pulse (left) and double pulse (right) accelerated protons of energy 8.7 ± 0.2 MeV are shown using the same colour scale.

It is interesting to note the change in the distribution of the proton flux when the double pulse mechanism is employed. The proton flux is more evenly spread and a much larger proportion of the proton flux is found in the wings of the beam compared to the single pulse accelerated proton beam. The shape of the dose profile for the double pulse accelerated proton beam begins to approach that of a top-hat profile for the higher energy components of the beam, which is clearly evident from the dose profiles for protons of energy ~ 10 MeV (see figure 4). For the single pulse accelerated beam, it seems as though there is a significant amount of structure in the dose maps (see figures 4 and 5) and this makes the double-pulse accelerated dose profiles appear much smoother in comparison. It is likely that the features seen in the single pulse dose maps emanate from ridge-like structures on the target's rear surface and it is these ridges that have been imprinted into the beam, similar to what has been observed previously with micro-grooved targets [19]. However, the very smooth profile of the double pulse accelerated proton dose map is not the result of more ideal target surface conditions, as these targets were of similar surface quality, and so we conclude that the apparent beam smoothing is a result of the double-pulse technique.

Discussion

Markey et al [10] made note that the proton flux enhancement resulting from the double pulse technique, as observed experimentally by a Thomson parabola spectrometer, was more pronounced at 12° to the laser axis as compared to the spectrometer placed along the target normal axis. This work goes some way to explaining this observation, in that it shows that the double pulse technique appears to have a significant effect not only on the integrated flux of protons, but also on how those protons are distributed across the beam. As can be seen in figure 4, for the double pulse accelerated beam, the proton dose remains above 80% of the maximum within angles up to 15° from the centre of the beam. This will be beneficial for proton heating and imaging applications where a more uniform dose profile is required.

In the double laser pulse acceleration mechanism, the generation of an enhanced accelerating field after a sufficient amount of plasma expansion on the rear surface has already occurred also supports our observations whereby imperfections on the rear surface are smoothed out and that the proton flux is more widely spread across the beam. It is likely to be the result, in part, of the pre-expansion on the rear surface and the fact that the highest accelerating gradient is found at the boundary of the two proton distributions, rather than at the plasma-vaccum interface, which gives rise to a smoother, more evenly distributed transverse sheath density profile. 2D simulations are currently underway in order to decipher the underlining mechanisms behind the observed enhancement in the angular

distribution and the changes in the envelope divergence of the proton beam.

In the studies carried out by Carroll et al [20], they reported the use of a model which maps the resulting divergence versus proton energy graph for a given input sheath field spatial distribution on the rear surface of the target. The shape of the divergence graph resulting from a gaussian shaped sheath is remarkably similiar to that of the double pulse accelerated divergence graphs (see figure 3), in that it displays the plateau-like region followed by a fast drop-off. Whereas the single pulse divergence graph appears to be a convolution of the divergence graphs resulting from an inverse parabolic and a gaussian shaped sheath as given in reference [20]. As a result, this suggests that the effect of the double pulse interaction here is to change the shape of the sheath field on the rear surface to one that is more gaussian-like than the characterisitic shape of a single pulse generated sheath.

The double-pulse mechanism of laser acceleration has already proven [9,10] to be a way in which one can enhance the properties of the proton beam produced. As it is an optically based method, rather than reliant on target engineering, it is much better suited for high repetition rate laser systems. This technique is very promising and suggests that temporal shaping of the laser pulse would be a useful feature in the design of a laser-proton source for applicative use.

Conclusions

We have demonstrated the effect on the angular distribution of a laser accelerated proton beam when a double-pulse profile is introduced into the interacting laser pulse. In particular, our results show that, with the double-pulse configuration, the envelope divergence of the proton beam decreases much slower with proton energy compared to the single-pulse accelerated proton beam divergence. We have compared this result to the model used by Carroll et al [20] to deduce that the sheath profile becomes more Gaussian shaped with the use of a double-pulse laser profile. Furthermore, the distribution of the proton flux changes when a double pulse is employed. There is an increased proportion of protons in the wings of the beam, making the dose profile appear more top-hat like, accompanied by a visible decrease in the appearance of structure in the dose maps which results in high quality, smooth proton beams.

These preliminary results merit further investigation using multi-dimensional simulations of double pulse acceleration in order to fully resolve the underlining reason for the improvement in the angular distribution and the changes in the beam divergence as seen here. It is hoped that further investigation into this effect will lead to optimisation of the enhancement.

Acknowledgements

The authors would like to acknowledge the expert support of the laser, engineering and target fabrication staff of the Central Laser Facility. This work was supported by the UK Engineering and Physical Sciences Research Council (grant number EP/E035728/1 and EP/E48668/1) and the Bundesministerium fur Bildung and Forshung, BMBF, support code 06 DA 90441.

References

1. R. A. Snavely *et al.*, Physical Review Letters **85,** 2945 (2000).
2. E. L. Clark *et al.*, Physical Review Letters **84,** 670 (2000).
3. A. Maksimchuk *et al.*, Physical Review Letters **84,** 4108 (2000).
4. M. Roth *et al.*, Physical Review Letters **86,** 436 (2001).
5. E. Lefebvre, M. Carrie, and R. Nuter, Comptes Rendus Physique **10,** 197 (2009).
6. A. Pelka *et al.*, Physical Review Letters **105,** (2010).
7. J. A. Cobble *et al.*, Journal of Applied Physics **92,** 1775 (2002).
8. L. Romagnani *et al.*, Laser and Particle Beams **26,** 241 (2008).
9. A. P. L. Robinson, D. Neely, P. McKenna, and R. G. Evans, Plasma Physics and Controlled Fusion **49,** 373 (2007).
10. K. Markey *et al.*, Physical Review Letters **105,** (2010).
11. S. C. Wilks *et al.*, Physics of Plasmas **8,** 542 (2001).
12. J. Fuchs *et al.*, Physical Review Letters **91,** (2003).
13. L. Romagnani *et al.*, Physical Review Letters **95,** (2005).
14. B. Dromey, S. Kar, M. Zepf, and P. Foster, Review of Scientific Instruments **75,** 645 (2004).
15. E. Brambrink *et al.*, Physical Review Letters **96,** (2006).
16. T. E. Cowan *et al.*, Physical Review Letters **92,** (2004).
17. M. Borghesi *et al.*, Fusion Science and Technology **49,** 412 (2006).
18. J. Fuchs *et al.*, Physical Review Letters **91,** (2003).
19. F. Nurnberg *et al.*, Review of Scientific Instruments **80,** (2009).
20. D. C. Carroll *et al.*, Physical Review e **76,** (2007).

Implications of primary and secondary sources of debris for ultrathin targets on Vulcan Petawatt

Contact *david.carroll@strath.ac.uk*

D. C. Carroll, D. A. MacLellan, G. Scott* and P. McKenna

SUPA, Department of Physics, University of Strathclyde, Glasgow G4 0NG, UK

S. Kar, R. Prasad, K. F. Kakolee, H. Ahmed, D. Doria and M. Borghesi

School of Mathematics and Physics, Queen's University Belfast, Belfast BT7 1NN

M. Notley, R. Heathcote, D. Neely

**Central Laser Facility, STFC Rutherford Appleton Laboratory, Oxfordshire OX11 0QX, UK*

Introduction

The interaction environment of laser-solid interactions is becoming of greater interest to the research community. As high repetition rate high power laser projects, such as ELI [1] and HiPER [2], develop a concern that has come to the fore is the effect of residual plasma and debris in the interaction region on the survival of subsequent targets injected into the area. With laser-plasma ion acceleration research pushing for the thinnest targets [3,4], going from previous micron thickness now down to nanometres, targets have are also more fragile.

During a recent experiment in Target Area Petawatt (TAP) ultrathin targets down to the 10's of nanometre range were shot. An issue that arose during the experiment was the survivability of targets during multi-shot cycles of the target chamber. This report describes how the issue was identified to be debris hitting the targets waiting to be shot and how this issue was resolved.

Experiment Setup

The experiment was performed using the Vulcan laser in TAP, delivering pulses of 1.053 µm wavelength light, with an energy of up to 200 J (on target) and duration equal to 1 ps, FWHM. The p-polarized pulses were focused to an 8 µm diameter FWHM spot. The majority of the targets were 10nm and 25nm C with a few above 100 nm Al. A Cu frame was used to support the targets (see figure 1) as they were sufficiently thin that they could not be free-standing. Two different set-ups were used during the experiment, initially the setup included a plasma mirror but this was removed during the later stages of the experiment. The main diagnostic for the experiment was stacks of dosimetry film which included in their mount design a sheet of lead to protect stacks on the mount that were not being used during the shot (i.e. for multi-shot cycle of the chamber). The laser incident angle on target was either at 0 degrees (relative to target normal) with the plasma mirror (PM) or at 2 degrees when the PM was not being used.

The problem: target survivability

During the latter stages of the experiment, where the setup had been changed to accommodate shots without the plasma mirror in place, target survivability became an issue when the vast majority of the targets were ultrathin (below 100 nm thick). The target wheel was typically loaded with 4 targets for a 4 shot pump down cycle of the target chamber. However, not all targets were surviving on the wheel long enough to be shot, resulting in an unexpected shortening of the planned shot sequence as the chamber had to be let-up to replace the lost targets. The initial solution was to load 6 targets (maximum possible whilst keeping a reasonable separation between the targets) onto the target wheel. Typically 2-3 targets were lost during a pump-down cycle, with the worst case being the loss of all 5 other targets after the first shot. Note that the foils themselves did not survive, but the Cu frame of these lost targets was unaffected.

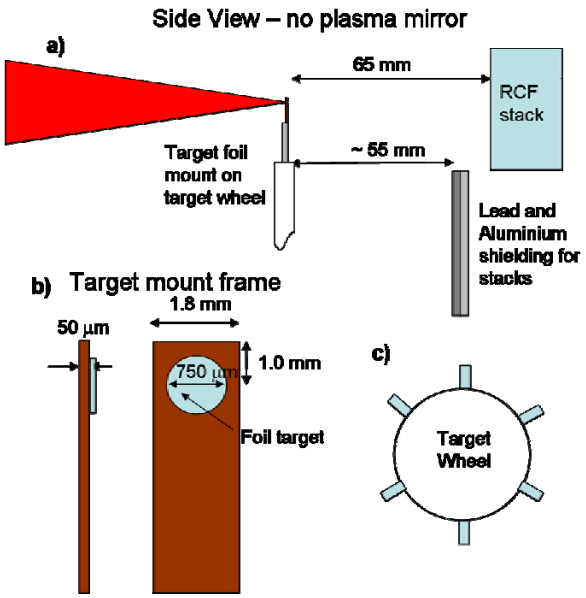

Figure 1: a) shows the basic experiment set-up. b) The specifications of the Cu frame which the ultrathin foils are mounted on. c) Shows a sketch of the target wheel and the rough equal spacing for 6 targets.

Eliminating pump down as a cause of the target loss

The initial thought as to what was causing the loss of targets was the pumping down of the chamber itself. This has in the past caused thin targets and filters to be damaged or lost during experiments. The slow pump down sequence available in the vacuum controls was used to minimize this risk. However, the loss of targets continued. To confirm that targets were surviving the slow pump down a camera was setup with a x2 magnification looking at the target front surface. This enabled the targets to be checked once the pump down had finished. It was found that the targets were surviving the pump down but were still be lost during the shots.

Debris sources

As the Cu frame supporting the shot target was typically destroyed during the interaction (even though the laser was not hitting the frame directly), it was suggested that target and frame debris was destroying the neighbouring targets. However, this does not account for the loss of targets on the other side of the target wheel.

After studying the setup (and photos of the earlier setup with plasma mirror) we came to the conclusion that there are two

major distinct sources of debris in the interaction environment of the experiment.

The first source is debris from the target and the more massive supporting Cu frame. This theory is supported by the observation of Cu deposition on the plasma mirror, see figure 2, and the fact that the Cu is deposited within a well defined area around the target normal axis. Typically the whole top part of the Cu frame where the target foil would be mounted is observed to be missing. The reason for the Cu frame being destroyed is uncertain at present as the frame is ~320 μm from the laser focus spot, however it is likely due to the lateral expansion of the plasma

The second source of debris arises from the lead radiation shielding for the RCF stacks, as a thin coating of lead was observed to be on the target wheel side which was facing the shielding. This is a secondary debris source generated from debris from the target (including Cu frame) hitting the shield. This is also supported by the observation of discolouration of the surface of the lead stack shield and is also observed for the lead shielding used during the plasma mirror setup shown in figure 2.

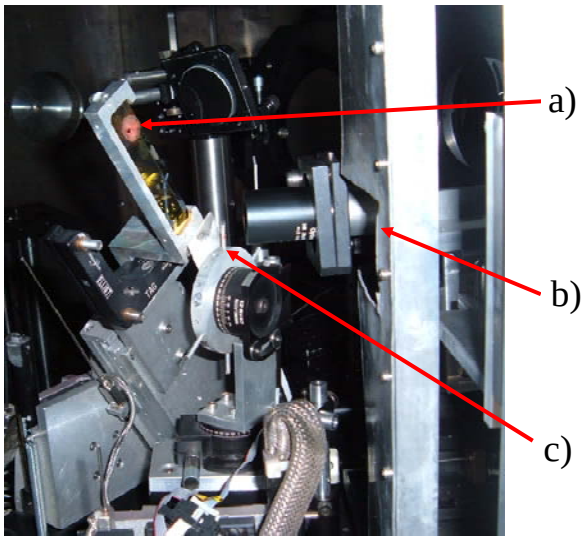

Figure 2: Photo of experiment setup when the plasma mirror was being used. This shows the target wheel which is used to mount multiple targets on. a) The plasma mirror in this photo clearly shows Cu debris deposited on the surface which comes from the Cu frame that the ultrathin foil is mounted on. Note that the debris region on the plasma mirror at 33 mm from target is roughly 10-15 mm across for the highest concentrations. b) The lead shielding around the gap left for the stacks is discoloured; this was also observed in the setup without plasma mirror and is from either coating or ablation of the surface by target debris. c) Stalk which the Cu frame is attached to mounted on the target wheel

Hypothesis of target destruction

An interpretation of the available evidence points to targets being destroyed by target debris bouncing off the lead shield back towards the target wheel, with additional debris ablated from the stack shield surface. In the setup without the plasma mirror the stack shield is perpendicular to the target normal axis. This means that debris emitted along the target normal axis will hit and be reflected back along this axis. As the debris would be coming roughly along a direction perpendicular to the target surface in this case, the Cu frame mounts of the targets would offer minimal protection. For the setup with the plasma mirror the lead shield was at an angle to the target normal axis, see figure 2, which means any debris reflected from the shield is unlikely to return back along the target normal axis and hit any other targets.

Testing of hypothesis and protecting targets

To test the hypothesis that debris is coming back towards the target wheel from the stack shielding, and also with the aim of protecting any remaining targets, a PTFE plastic shield was put in place as shown in figure 3. The top edge of the PTFE was placed roughly half-way down the stalk holding the target in the top position and was 1 cm from target. The initial test resulted in debris from the stack being prevented from reaching the target wheel. The debris deposited on the PTFE can clearly be seen in figure 3. For this pump down one target was lost, which was the neighbour of a shot target. This was either from debris coming from the side or possibly target debris hitting the top of the PTFE shield and bouncing back. At the top of the PTFE on the target wheel side debris deposition was observed which indicated that the PTFE shield was too high.

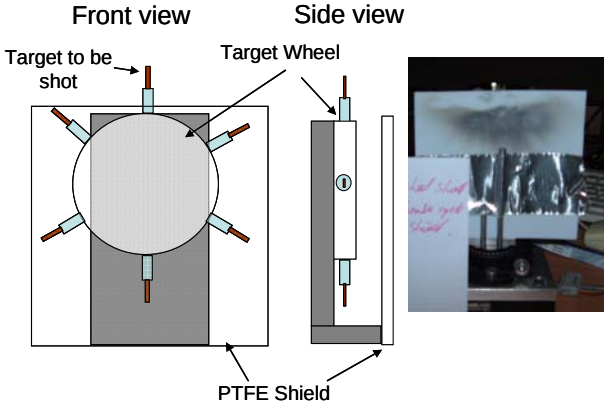

Figure 3: The left side shows a schematic of the PTFE debris shield put in place to protect the targets. Note that the top edge of the shield should be low enough to avoid target debris hitting it and bouncing back as this defeats the purpose of the shield. The right side shows the debris shield after a single pump down. The debris deposited coming from the stack direction can clearly be seen on the white PTFE.

A second attempt involved positioning the PTFE shield top edge roughly level with the bottom of the stalk, with a similar horizontal distance from the target. During this pump down no targets were destroyed other than those directly shot by the laser.

Conclusions

In conclusion we find that even though ultrathin targets themselves may not produce significant debris when irradiated by a high power laser pulse, the frames supporting the targets must also be considered. The debris from the target frame was found to be generating secondary debris when hitting a soft material, lead, and resulting in the destruction of the very fragile neighbouring ultrathin foil targets. This was a significant problem as it was slowing down the rate of shots because the chamber had to be cycled sooner than planned to replace these targets. This also added significant pressure to the target fabrication team who were struggling to keep up with the demand for targets needed to replace those lost. A simple and quick solution implemented on the experiment involved positioning a PTFE shield that enabled primary debris from the main target to propagate away from the target wheel, but blocked any reflected and secondary debris coming back and hitting the targets waiting to be shot.

This is an issue which has not arisen previously as target foils typically used on experiments in TAP are thicker and less fragile. These measurements also raise concern about the possible sources of secondary debris arising from the use of ‘soft’ materials such as lead in close proximity to the main

laser-solid interaction. Any experiments that expect to use ultrathin targets should take these findings into consideration during planning of the experiment.

Acknowledgements

We acknowledge the expert support of the staff at the Central Laser Facility of the Rutherford Appleton Laboratory. This work is supported by EPSRC (Grants No. EP/E048668/1 and No. EP/E035728/1).

References

1. http://www.extreme-light-infrastructure.eu/A reference
2. http://www.hiper-laser.org/
3. D. Neely *et al.* Appl. Phys. Lett. **89**, 021502 (2006)
4. A. Henig *et al.* Phys. Rev. Lett. **103** 245003 (2009)

Effects of laser pulse parameters on TNSA proton acceleration

Contact:*mireille.coury@strath.ac.uk

M. Coury*, D. C. Carroll, X. H. Yuan[1], C. M. Brenner[2], R. J. Gray, M. N. Quinn, O. Tresca and P. McKenna
Department of physics, University of Strathclyde, SUPA, Glasgow G4 0NG, UK
[1] *Present Address: State Key Laboratory of Transient Optics and Photonics, Xiâan Institute of Optics and Precision Mechanics,Chinese Academy of Sciences, Xiâan 710119,China*
[2] *also with Central Laser Facility, STFC RAL, Oxfordshire OX11 0QX, UK*

K. L. Lancaster, A.P.L. Robinson and D. Neely
Central Laser Facility, STFC RAL, Oxfordshire OX11 0QX, UK

M. Burza and C.-G. Wahlström
Department of Physics, Lund University, P.O. Box 118, S-22100 Lund, Sweden

Y. T. Li and X. X. Lin
Beijing National Laboratory of Condensed Matter Physics Institute of Physics, CAS, Beijing 100190, China

INTRODUCTION

Generation of MeV ion beams, following the interaction of high intensity laser pulses with solid targets, has been actively studied by many international groups since the discovery of the phenomenon[1,2]. The ion acceleration mechanism from the target rear, referred to as target normal sheath acceleration (TNSA)[3], is the dominant acceleration process for relativistic laser intensities and target thicknesses of $\sim$100 μm used in this study. High power laser systems generate ultra-bright, low emittance multi-MeV proton beams[4]. The high beam quality has potential for applications in proton radiography[5], medicine[6] and fusion studies[7]. During the laser-solid interaction, a large number of relativistic electrons is generated and propagate through the solid target. The electron beam forms, at the rear-surface, a dense plasma sheath with a $\sim$ TV/m field which lasts for a period of the order of the laser pulse duration. This field ionizes the target surface atoms and accelerates ions in the direction normal to the surface. Since the protons, originating from contamination layers, are accelerated in this electrostatic field, maximizing the coupling of laser energy into electrons is crucial to optimising the proton energies.
In this report, we present experimental results obtained using the Vulcan Petawatt laser demonstrating the dependency of the maximum proton energy and laser-to-ion energy conversion efficiency on the laser pulse energy and focal spot size.

EXPERIMENTAL SETUP

The Vulcan Petawatt laser provides p-polarized laser pulses with energies up to 400 J , and pulse duration of $\sim$ 1 ps, at a wavelength λ of 1.054 μm. The laser pulse was focused onto the target at an incident angle of 23°, using an f/3 off-axis parabolic mirror (OAP). Peak intensities, I_L, up to 6×10^{20} W/cm^2 were delivered on target, as the laser energy, E_L, is $\sim$ 30 % of the total laser energy. The layered targets used are 2 mm $\times$ 2 mm foils of a 100 μm Al as a generation and propagation layer, a 5 μm Cu sandwiched fluorescent layer and a 1 μm Al layer. Monochromatic and spatially resolved two-dimensional (2D) images of the of the Cu Kα X-ray emission are recorded using an imaging system consisting of a spherically bent Bragg crystal that images emission from the fluorescent layer near the target rear-surface onto a FujiFilm BAS image plate detector. The magnification is set to 10, giving a spatial resolution of 20 μm, and the crystal angle is set at 1.31° satisfying the Bragg condition in the second diffraction order for Cu Kα at 8.048 keV[8].
The Proton beam spatial and energy distributions are measured using radiochromic films (RCF)[9]. The RCF stack (HD 810) are positioned 4 cm away from the rear of the target and cover an energy range from 1.2 MeV up to 40 MeV .

EXPERIMENTAL RESULTS

Two experimental scans were performed to investigate the effect of the laser energy on the relativistic electron beam and consequently on the TNSA generated proton beam. One scan, referred as to the energy scan, consists of varying E_L from $\sim$ 3 to 150 J at a fixed laser spot diameter of $\phi \sim 8$ μm. The second scan, referred as to the focus scan, consists of defocusing ϕ from $\sim$ 8 to 100 μm at a fixed $E_L \sim 150$ J.
Figure 1 presents the measured maximum proton energy E_{max} and laser-to-ion energy conversion efficiency obtained for both scans. Experimental results show a greater maximum proton energy, E_{max}, for the focus scan compared with the energy scan, at the same laser intensity. A similar trend is observed for conversion efficiency. The FWHM of the Cu Kα source size, used to infer the rear sheath diameter, shown in Figure 2, varies

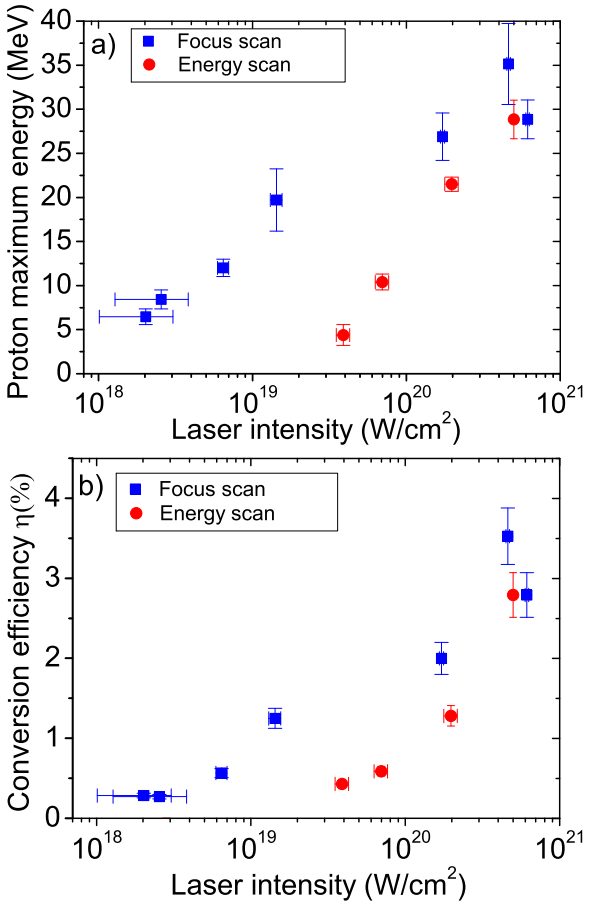

Figure 1: a) Proton maximum energy E_{max} as a function of laser intensity. b) Laser-to-ion energy conversion efficiency as a function of laser intensity.

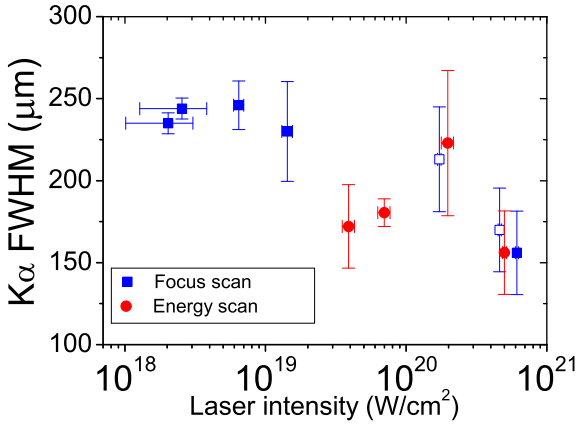

Figure 2: Cu Kα FWHM as a function of laser intensity. No signal was recorded at $I_L \sim 2\text{x}10^{20}$ and $5\text{x}10^{20}$ W/cm^2, missing values (open blue square) are extrapolated from the recorded data.

from $\sim$ 250 to 180 μm with increasing laser intensities for the focus scan. Results from the energy scan show a FWHM $\sim$ 180 μm.

SUMMARY

The results clearly show that the maximum proton energy cannot be defined in terms of laser pulse intensity alone and that laser pulse energy plays a key role. At a given intensity, large energy defocused irradiation results in considerably higher energy protons than the equivalent intensity for lower energy tight focus irradiation. Modelling is presently underway to determine the functional dependencies on the laser pulse parameters.

ACKNOWLEDGMENTS

This work was supported by the Engineering and Physical Sciences Research Council (grant numbers EP/E048668/1 and EP/E035728/1). We acknowledge the support and contribution of the Target Preparation Laboratory, Vulcan laser staff and the Engineering workshop at CLF, RAL and discussions with Dr B. Ersfeld (University of Strathclyde).

REFERENCES

[1]E. L. Clark, K. Krushelnick, J. R. Davies, M. Zepf, M. Tatarakis, F. N. Beg, A. Machacek, P. A. Norreys, M. I. K. Santala, I. Watts, and A. E. Dangor, Phys. Rev. Lett. **84**, 670 (2000).

[2]R. A. Snavely, M. H. Key, S. P. Hatchett, T. E. Cowan, M. Roth, T. W. Phillips, M. A. Stoyer, E. A. Henry, T. C. Sangster, M. S. Singh, S. C. Wilks, A. MacKinnon, A. Offenberger, D. M. Pennington, K. Yasuike, A. B. Langdon, B. F. Lasinski, J. Johnson, M. D. Perry, and E. M. Campbell, Phys. Rev. Lett. **85**, 2945 (2000).

[3]S. C. Wilks, A. B. Langdon, T. E. Cowan, M. Roth, M. Singh, S. Hatchett, M. H. Key, D. Pennington, A. MacKinnon, and R. A. Snavely, Phys. Plasmas **8**, 542 (2001).

[4]T. E. Cowan, J. Fuchs, H. Ruhl, A. Kemp, P. Audebert, M. Roth, R. Stephens, I. Barton, A. Blazevic, E. Brambrink, J. Cobble, J. Fernández, J.-C. Gauthier, M. Geissel, M. Hegelich, J. Kaae, S. Karsch, G. P. Le Sage, S. Letzring, M. Manclossi, S. Meyroneinc, A. Newkirk, H. Pépin, and N. Renard-LeGalloudec, Phys. Rev. Lett. **92**, 204801 (2004).

[5]M. Borghesi, D. H. Campbell, A. Schiavi, M. G. Haines, O. Willi, A. J. MacKinnon, P. Patel, L. A. Gizzi, M. Galimberti, R. J. Clarke, F. Pegoraro, H. Ruhl, and S. Bulanov, Phys. Plasmas **9**, 2214 (2002).

[6]C.-M. C. Ma, R. L. Maughan, and C. G. Orton, Med. Phys. **33**, 571 (2006).

[7]M. Roth, T. E. Cowan, M. H. Key, S. P. Hatchett, C. Brown, W. Fountain, J. Johnson, D. M. Pennington, R. A. Snavely, S. C. Wilks, K. Yasuike, H. Ruhl, F. Pegoraro, S. V. Bulanov, E. M. Campbell, M. D. Perry, and H. Powell, Phys. Rev. Lett. **86**, 436 (2001).

[8]J. A. Koch, Y. Aglitskiy, C. Brown, T. Cowan, R. Freeman, S. Hatchett, G. Holland, M. Key, A. MacKinnon, J. Seely, R. Snavely, and R. Stephens, Rev. Sci. Instrum. **74**, 2130 (2003).

[9]F. Nürnberg, M. Schollmeier, E. Brambrink, A. Blažević, D. C. Carroll, K. Flippo, D. C. Gautier, M. G. el, K. Harres, B. M. Hegelich, O. Lundh, K. Markey, P. McKenna, D. Neely, J. Schreiber, and M. Roth, Rev. Sci. Instrum. **80**, 033301 (2009).

Features of ion acceleration from ultra-thin foils on Vulcan Petawatt

Contact *nicholas.dover08@imperial.ac.uk*

N.P. Dover, C.A.J. Palmer, M.J.V. Streeter, S.R. Nagel and Z. Najmudin

Blackett Laboratory, Imperial College London, London SW7 2BZ, U.K.

R. Heathcote, M.M. Notley, G. Scott and D. Neely

Central Laser Facility, Rutherford-Appleton Laboratory Chilton, Oxon, OX11 0QX, U.K.

B. Albertazzi, M. Nakatsutsumi and J. Fuchs

LULI, École Polytechnique, CNRS, CEA, UPMC, route de Saclay, 91128 Palaiseau, France

H. Ahmed, K.F. Kakolee, S. Kar, R. Prasad, M. Zepf and M. Borghesi

Centre for Plasma Physics, Queen2s University Belfast, Belfast, BT7 1NN, U.K

D.C. Carroll, D.A. MacLellan and P. McKenna

Department of Physics, SUPA, University of Strathclyde, Glasgow G4 0NG, UK

A. Kon, M. Tampo and R. Kodama

Graduate School of Engineering, Osaka, 565-0871, Japan

P. Hilz and J. Schreiber

Max-Planck-Institut für Quanten Optik, Garching, Germany

Introduction

During the last decade there has been a great deal of experimental, numerical and theoretical research into the understanding and improvement of laser-plasma energetic ion accelerators. Until recently, the majority of research focused on sheath acceleration, which relies on the laser heating up electrons at the laser-plasma interface to a high temperature [1-2]. These fast electrons then propagate through the overdense target, and, as they exit the rear of the plasma, create space-charge fields along the plasma-vacuum interface. These electric fields are quasi-static, and cause the proton and ion species to expand into the vacuum, creating a highly laminar, low emittance hadron beams. However, the heating of the electrons, and hence the ions, by high intensity lasers scale poorly with intensity [3-4]. This may limit the applicability of this scheme for certain applications, such as hadron therapy.

Hence, an ion acceleration scheme that can achieve higher energies and scales well with increasing intensity is desirable. Furthermore, for many applications, it is vital to have a beam with high charge at high energy, as opposed to the broad exponentially decreasing spectrum typically produced by sheath acceleration. For this reason, there has recently been considerable interest in investigating acceleration regimes utilising ultra-thin nanometre scale targets. These have become viable not only due to advances in target manufacture but also due to recent improvements in laser technology, in particular improvement in the contrast of the pulses, which is the ratio of main pulse intensity to pre-pulse intensity,

The most actively investigated scheme is to harness the radiation pressure of the laser to directly accelerate overdense plasma; radiation pressure acceleration (RPA) [4-8]. RPA is often split into two phases. The first is called hole-boring acceleration, where the high-intensity laser bores a hole into an overdense plasmas and accelerates ions at this boring interface in the same way as in other collisionless electrostatic shocks. The second phase is light-sail acceleration in which the plasma acts like a solar sail, and is directly pushed forward as a thin slab. Simulations of RPA have predicted beams with exceptionally small energy spreads and promising intensity scaling. Unfortunately, despite a number of recent experiments in conditions apparently suitable for RPA, the high quality beams promised have not yet been achieved. Recent studies have found clear signatures of RPA [9], but laser-plasma instabilities, imperfections in laser conditions, and three-dimensional effects have conspired to limit the efficient acceleration of ions with this scheme at currently available laser intensities.

For radiation to exert a pressure on plasma, the plasma must remain opaque to the plasma. However, due to the small initial thickness of the targets, the use of Vulcan Petawatt length pulses causes the plasma to heat up and expand prior to the arrival of the high intensity peak of the laser pulse. If the density of the plasma drops below the relativistic critical density before the pulse reaches maximal intensity, the radiation pressure scheme ceases to be applicable. It has been shown in numerical simulations and experiments that there can then be considerable acceleration of ions and protons in this relativistic transparency regime, in which, after an initial hole-boring phase, the laser bulk heats the electron population in the target, which then transfers its energy further to the energetic ion species [10-12].

The experiment summarised here was designed to investigate proton and ion acceleration from ultra-thin targets in conditions suitable for radiation pressure acceleration using the Vulcan Petawatt laser, providing a higher energy and intensity at a longer pulse length than that of the experimental work published thus far on RPA. This report provides an update on the preliminary analysis of the experiment thus far. Further analysis and numerical simulation is still ongoing to more comprehensively investigate the interaction and acceleration processes.

Experimental setup

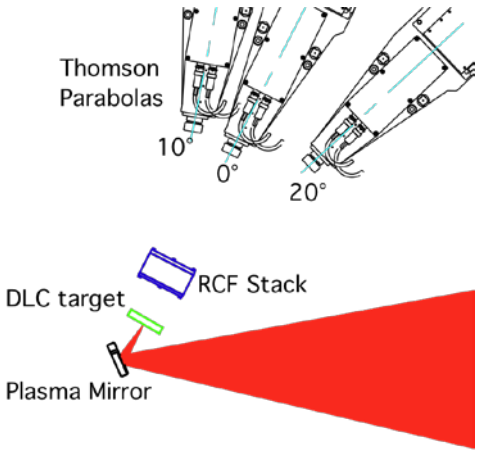

Figure 1. Experimental setup

The experiment was performed using the Vulcan Petawatt laser system at Rutherford Appleton Laboratory. The pulse contained (430 ± 70) J before the compressor, and a pulse length after the compressor of approximately 700 fs FWHM. The beam was focused to a focal spot of 8 μm FWHM, with 35% of the energy in the FWHM. A plasma mirror was used, at intensity on the

plasma mirror of 3×10^{14} Wcm^{-2}, in order to improve the contrast to an estimated 10^{-10}. The improvement to the contrast was to try to minimise the "blowing-up" the target before the arrival of the main pulse by the laser prepulse. The throughput of the compressor and parabola was measured with calorimetry to be 43%. The throughput of the plasma mirror was tested in linear polarisation, both *s* and *p*, and was found to be 72% and 69% respectively. For part of the experiment, the beam was circularly polarised by inserting a ½ and a ¼ waveplate into the beam before the plasma mirror. The combination of waveplates allowed the differences in reflectivity in *s* and *p* polarisation to be accounted for, in order to give circular polarisation after the plasma mirror. The intensity averaged over the FWHM was estimated to be 2.4×10^{20} Wcm^{-2}, equivalent to $a_0 \sim 14$.

The laser pulse was focused onto diamond-like-carbon (DLC) foils at normal incidence. DLC foils have been widely used recently when investigating ultra-thin targets in laser-plasma interactions due to their high tensile strength, heat resistance and mechanical stability. DLC targets of density 2.7 g/cc were used with thicknesses between 5 and 500 nm.

The energetic proton beams were measured using two different types of diagnostics. A radiochromic film (RCF) stack was placed approximately 10.6 cm directly behind the target. The stack contained alternating layers of Gafchromic HD-810 radiochromic dosimetry film and iron of differing thicknesses, allowing the extraction of information regarding the proton beam profile and crude energy spectrum of the proton beam. The RCF stack was split into an upper and lower half, with a 7 mm slit between them, to allow rear diagnostic access. Thomson parabola (TP) spectrometers were placed at 0, 10 and 20° from the target normal direction, at a distance of 76, 80, and 104 cm respectively. These spectrometers use collinear electric and magnetic fields to disperse ions spectrally and also separate them by the ion specific charge to mass ratio, allowing the extraction of proton and ion energy spectra with fine energy resolution. A pinhole was placed in front of the entrance to the 0, 10 and 20° spectrometers, with diameters of 50, 50 and 100 μm respectively. The pinhole size is determined by a trade-off between signal to noise ratio and spectral resolution.

Results

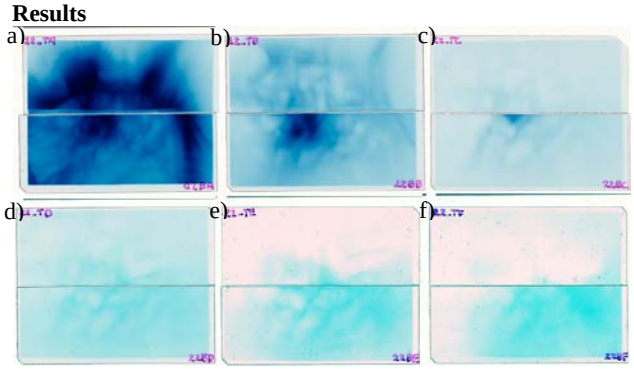

Figure 2. Example of RCF scans for a 5 nm DLC target. From a) to f), the energy corresponding to each layer is 4, 8, 14, and 20, 24 and 30 MeV respectively, where d-f) have been individually contrast enhanced to see detail. There was a gap of 7 mm between the top and bottom pieces.

An example of the RCF data is shown in figure 2. Darkening of the RCF indicates the regions of higher energy deposition. Note that heavy ions would be stopped in the aluminium light shield placed in front of this stack, and so these features can be attributed to protons alone. A number of different structures are apparent in the proton beam profiles. Firstly there is a clear ring structure at the edge of the profiles, which is present at the lowest energy film in the stack, but disappears quickly at higher energies. Then, there is a central beam with a very small divergence (~5°), which has a different energy distribution compared to the ring structure – it is still clearly visible up to higher energies, and usually brighter at 8 MeV than at 4 MeV. There are also some highly filamentary structures that cover most of the RCF film and have again a different energy spectrum from the other two features. Finally, up to 30 MeV (figure 1 e), it is possible to see a smooth, broad signal pointing off-axis to the right. These four different features have different structures and different energy spectra, indicating that the protons have been accelerated via different mechanisms.

The Thomson spectrometers, placed in the slit between the top and bottom half of the RCF stack, and placed at 0, 10 and 20°, allowed for a more detailed look at the energy spectrum at different parts of the beam, for protons as well as the carbon species. By matching up features on the RCF with the spectra from the Thomson spectrometers it is possible to extract more information to diagnose the acceleration mechanisms at each location.

Low Energy Ring

A ring was visible on almost all of the shots regardless of target thickness. The apex angle of the ring was never less than 30°, and always only visible on the 1st RCF piece in the stack, corresponding to 4 MeV protons. As the next layer corresponds to ~8 MeV, this indicates an extremely high flux, low energy proton emission. With very thin targets, the ring sometimes appeared to have some angular edges and corners, instead of a smooth annular ring, as seen in figure 3.

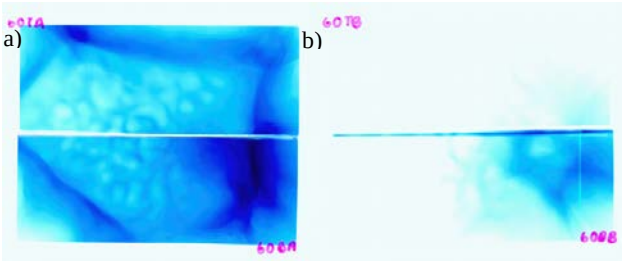

Figure 3. RCF stack layers at 4 MeV (a) and 8 MeV (b) for a 10 nm foil shot with circular polarisation. The ring structure here appears non-annular in shape, with some straight edges and sharp corners. A higher energy central beam is still visible, but pointed away from target axis.

Filamentary structure

The filamentary structures were seen very clearly for the 5 and 10 nm foils, and still somewhat visible on the 20 nm foils. The next thinnest target shot was a 100 nm foil, for which there was no filamentary structure visible. Due to the quickly spatially varying nature of the filamentary structure, it is difficult to determine whether the Thomson spectrometers were sampling a part of the high flux filament, or the low flux region in the centre of the 'bubbles'. As can be seen in figure 2 (d), the protons in the filaments reach over 20 MeV.

Non-thermal, peaked proton beam

A 'central' beam was seen for all thicknesses, but the characteristics of the beam varied with thickness. A very clear difference was seen between 20 nm foils and 100 nm foils. For the 20 nm foil and below, the beam always has a very low divergence (~ 5°), shows variation in position with respect to target normal, and occasionally has some structure (see, for example, the beam in figure 3). However, even when it is slightly structured, it is visibly different to the filamentation, being localised and with a higher flux. The central beam is visible for thicknesses down to 5 nm, although at 5 nm it was only present for 1 out of 3 shots. The two shots that did not see the beam were shot 2 weeks after the first 5 nm foil, and could be indicative of a worsening contrast during the run. At thicknesses of 100 nm and above, a beam is often seen with a

larger divergence (> 20°), and does not exhibit as much structure.

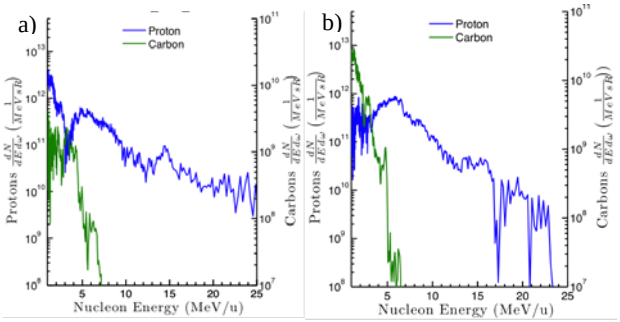

Figure 4. Energy spectra from the Thomson parabola diagnostic for a) 10 nm DLC (the same shot as seen in figure 2) and b) 100 nm DLC target, both shot at focus with circular polarisation.

From figure 2, it can be seen that for this shot, the low divergence central beam was pointed centrally, approximately where the 0° Thomson was positioned. The retrieved proton and carbon energy spectra are seen plotted in figure 4 a). The proton spectrum indicates a high flux, low energy component up to 2.5 MeV, then a further high flux peak in the spectrum at 6 MeV which decreases exponentially to 25 MeV, agreeing well with the features seen on the RCF. The carbon spectrum extends up to about 6 MeV/u (total energy ~70 MeV). The carbon signal therefore drops off for approximately the same velocity of ions as for the peak in the proton spectrum. A similar spectrum can be seen in figure 4(b), which is for a 100 nm target, and corresponds to the same location as a central beam on the RCF. Again, the carbon spectrum extends up to the same velocity at which the proton signals peaks. On all shots where a central beam overlapped with the Thomson parabola, a similar feature was seen.

Low flux high temperature smooth proton beam

The final feature, which was seen on almost all shots from 5 to 500 nm, is the low flux, smooth and divergent off-axis beam similar to that seen in figure 2 (e) and figure 5 (c-d). The maximum energy in this beam did vary with thickness, being maximum for 10 and 20 nm foils, and smallest for 5 and 500 nm foils.

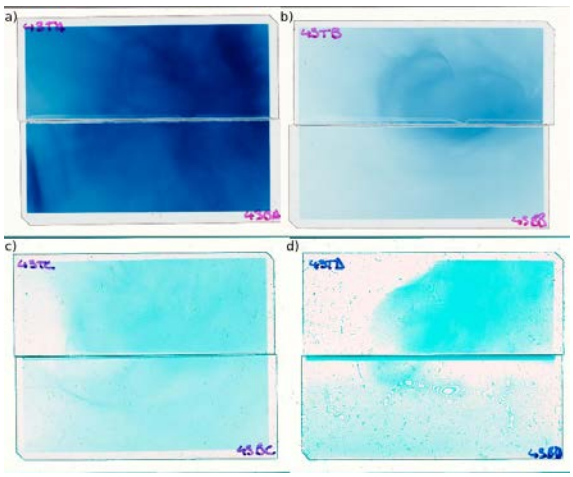

Figure 5. RCF films at a) 4 MeV, b) 8 MeV, c) 14 MeV and d) 20 MeV for a 20 nm DLC and a linearly polarised pulse. Both c) and d) have been contrast enhanced to see low flux detail.

The beam was also evident on the Thompson spectrometers. For example, the beam in figure 5 is very smooth and pointed up and to the right, only partly overlapping with the central beam. The edge of this low flux beam is seen in both the 0° and 20° Thomson spectrometers. Figure 6 (a) shows the relative proton signals in all 3 spectrometers. Above 10 MeV the proton signal for TP1 (0°) and TP3 (-20°) look very similar, decreasing with the same temperature to similar maximum energies. However, below 10 MeV very different signals are evident in the two different spectrometers. This would suggest that the 0° spectrometer sees a combination of the low flux high-energy beam, and a higher energy, narrower bandwidth (Non-thermal peaked) peak, whereas at -20° only the low flux high-energy beam is seen. The 10° spectrometer shows a thermal, but lower temperature proton beam reaching a lower maximum energy. Further differences are seen in the carbon spectra, where the 0° spectrometer sees a much higher flux of particles accelerated to 3-4 MeV/u than the off-axis spectrometers. This is seen on all shots with a peaked proton beam measured by the Thomson spectrometer.

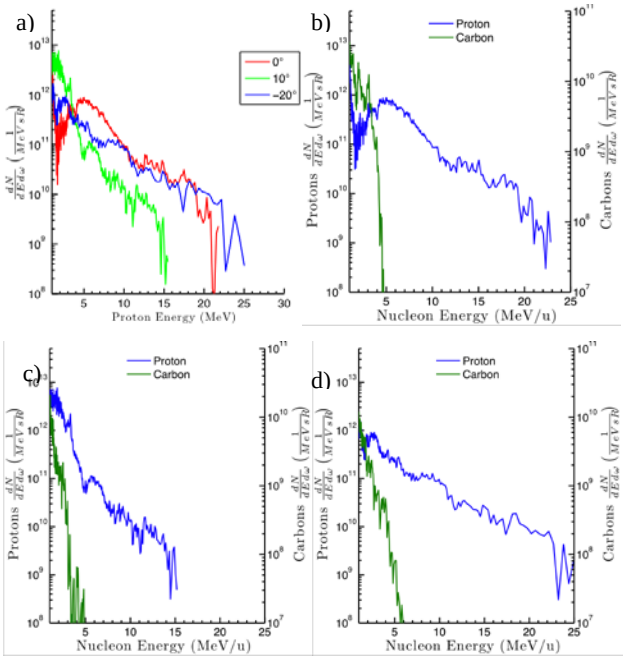

Figure 6. Energy spectra for protons and carbons from the same shot as figure 5. The variation in proton spectra (TP1 = 0°, TP2 = 10°, TP3 = 20°) is shown in a), followed by the relative proton and carbon spectra for b) 0°, c) 10°, and d) 20°.

Ion acceleration mechanisms

The ion and proton diagnostics therefore show a variety of different ion features with markedly different proton and carbon spectral properties. Some of the structures were consistent throughout the parameter scan undertaken on the experiment, whilst some varied. Due to the comparatively long length and high energy in the laser pulse it is expected that the target will expand quickly due to electron heating during the rising slope of the laser pulse, which results in a reducing density. If the target remains over-dense long enough, the laser pulse can exert a pressure on the front surface of the target and some radiation pressure type acceleration can take place. However, if the target becomes transparent to the radiation before the highest intensity part of the pulse, then direct radiation pressure acceleration of the target cannot take place, and the interaction becomes underdense.

Two papers recently published have numerically investigated the interaction of an ultra-intense laser with DLCs in very similar laser conditions to those in this experiment, using 2D and 3D particle-in-cell simulation [11-12]. Very high energy carbon beams (> 40 MeV/u) are predicted to be accelerated in the relativistic transparency regime at an optimum thickness, which was found in the simulations to be between 50-120 nm. It is also proposed that for the thinnest targets, 5-10 nm DLC, quasi-monoenergetic carbon beams can be produced via the

acceleration of ion solitary waves, which are a result of the formation of an ion density spike at the laser-plasma interface before the target becomes relativistically underdense. This quasi-monoenergetic feature was amplified by using circular polarisation. For all thicknesses, the comparatively low charge density combined with the lower mass to charge ratio of the proton species compared to the carbon species results in the proton species being pushed out in front of the carbon species.

Due to the similarities between the numerical simulations carried out and the experimental conditions in this experiment, it is instructive to compare our results with those predicted in the above publications. Firstly, in this experiment the predicted 40 MeV/u carbon beams were not observed. The maximum carbon energy seen on the experiment was ~ 8 MeV/u. The carbon beams were significantly lower energy for the 500 nm targets, but were similar for 5, 10, 20 and 100 nm, and did not vary much between circular and linear polarisation. However, the 5 and 10 nm target interactions do show some similarities with those predicted [10], achieving similar maximum energies to those predicted and occasionally showing non-thermal spectra (see carbon spectra in 4 a)). Furthermore, in the experiment a non-thermal peaked proton signal was seen for all thicknesses except 500 nm. This is consistent with the proton species being pushed out in front of the expanding carbon species in the 'self cleaning' process. The peak energy of the non-thermal peaked part of the proton beam did not vary much with polarisation or thickness, suggesting that in all cases the carbon species expanded at a similar rate. This is consistent with the lack of variance in the maximum carbon energies.

A further similarity with the relativistic transparency regime is in the prediction of peak energies off-axis. For linear polarisation, the beam is predicted to be off-axis in the direction along the polarisation direction. In the experiment, a low flux high temperature proton beam was seen off-axis on many shots, reaching higher energies than those in the non-thermal peaked feature. Furthermore, the carbon beam captured in the Thomson parabolas also was generally higher in the 20° spectrometer than the other two.

Apart from the central non-thermal peaked beam and the low flux high temperature beam, we also observed two other effects in the experiment – a ring structure which was consistent for all thicknesses and always at very low energies, and a filamentation structure which only appeared for 5 and 10 nm foils. The origin of the ring may be from a hollow jet due to channel formation after the target becomes relativistically underdense. The ponderomotive force will push electrons out of the focal spot, forming a channel, and a hollow jet is formed at the edge of the plasma along the walls of the channel. This feature can be seen on transverse shadowgraphy images taken of the interaction, and has been observed in a previous experiment using Vulcan Petawatt with similar targets. Finally, the filamentation seen for the 5 and 10 nm foils has also been seen on a similar previous experiment and has been attributed to Rayleigh-Taylor instabilities during the overdense phase of the interaction. The radiation acts as a light fluid pushing against the denser fluid of the target, resulting in the instability growth and a break-up of the target. This break-up is maintained throughout the underdense phase of the interaction, resulting in the bubble shapes visible in figure 2.

Conclusion

Preliminary analysis of the interaction of the Vulcan Petawatt laser with nm-scale carbon targets has been performed to investigate the different mechanisms that can accelerate protons and carbon ions. Multiple features were observed, including 1) low energy ring structures, due to channel formation as the target becomes underdense; 2) filamentation for 5 and 10 nm targets due to the Rayleigh-Taylor instability; 3) central non-thermal peaked proton beams due to 'self cleaning' of the lower charge density proton species; 4) a smooth off-axis proton beam going to high energies but with a characteristic low flux, possibly related to the post-acceleration in the relativistic transparency regime. Further analysis includes extracting spectra from different regions in the RCF stack, further investigation of the low energy ring from analysing transverse probe images, confirming calibration of the image plate diagnostic, and performing numerical 2D PIC simulations to further understand the interaction. By gaining a deeper understanding of the acceleration mechanisms, further experiments should be in a better position to optimise the experimental parameters needed to reach high proton and carbon energies with higher efficiencies.

Acknowledgements

The authors acknowledge the assistance of the Central Laser Facility staff at the Rutherford Appleton Laboratory in carrying out this work. This work was supported by the Laser Induced Beams of Radiation and their Applications (LIBRA) programme, which is funded by EPSRC.

References

1. Clark, E.L. et al., *Physical Review Letters*, **84**(4), 670-673 (2000)
2. Snavely, R.A. et al., *Physical Review Letters*, **85**(14), 2945-2948 (2000)
3. Wilks, S. C, et al. *Physical Review Letters*, **69**(9), 1383-1386 (1992)
4. Beg, F.N, et al. *Physics of Plasmas* **4**(2), 447-457 (1997)
5. Esirkepov, T. et al., *Physical Review Letters*, **92**(17), 175003 (2004)
6. Robinson, A.P.L. et al., *New Journal of Physics*, **10**, 013021 (2008).
7. Qiao, B. et al., *Physical Review Letters*, **102**(14), 145002 (2009).
8. Liseykina, T.V. et al., *Plasma Physics and Controlled Fusion*, **51**(12), 124033 (2008)
9. Henig, A. et al., *Physical Review Letters*, **103**(24), 245003 (2009)
10. Yin, L. et al., *Physics of Plasmas*, **18**, 063103 (2011)
11. Yin, L. et al., *Physics of Plasmas*, **18**, 053103 (2011)
12. Henig, A. et al., *Physical Review Letters*, **103**(4), 045002 (2009)

Effects of Density Scale Length on Critical Surface Morphology Via Measurements of Laser Specular Reflectivity

Contact:*ross.gray@strath.ac.uk*

R. J. Gray and P. McKenna
SUPA, Department of Physics, University of Strathclyde, Glasgow, G4 0NG, UK

C. R. D. Brown and D. J. Hoarty
Atomic Weapons Establishment, Aldermaston, Reading, Berkshire RG7 4PR, UK

T. Kampfer, K. S. Schulze and I. Uschmann
Institut fur Optik und Quantenelektronik, Friedrich-Schiller-Universitat Jena, Max-Wien-Platz 1, D-07743 Jena, Germany and Helmholtz-Institut Jena, Helmholtzweg 4, D-07743 Jena, Germany

O. Culfa, R. J. Dance, A. K. Rossall, E. Wagennaars and N. Woolsey
University of York, York Plasma Institute, Department of Physics, York, YO10 5DD, UK

N. Booth and K. L. Lancaster
Central Laser Facility, STFC Rutherford Appleton Laboratory, Didcot, Oxfordshire, OX11 0QX, UK

S.A. Pikuz
Moscow State University, Department of Physics, Vorobyevy Gory, Moscow, 117822, Russia

I. Introduction

The potential applications of intense laser-plasma science include fusion energy[1], oncology[2], accelerator technology and defense. The future development of these applications require, not only a thorough understanding of the bulk transport physics but also a detailed knowledge of the complex laser-plasma interaction at the front surface of the target. Increased understanding in this area could lead to source optimisation and improved coupling efficiency into the plasma.

High power lasers often have significant levels of amplified spontaneous emission which drives preplasma expansion on the front surface of the target. The density profile of this plasma has significant implications for the laser energy absorption and laser-electron coupling as well as introducing a number of nonlinear optical and collective plasma effects. Given that the plasma responds to the presence of the laser pulse and laser pulse propagation is in turn effected by the preplasma, the underlying physics can very quickly become intractably difficult to deconvolve. With the aid of both hydrodynamic and Particle in Cell (PIC) simulations many insights have been gained in this area. Conversly, direct experimental measurements of the front surface have been limited by the lack of effective techniques which can probe not only the underdense region but also the region of the relativistically corrected critical density surface. Previously published results which relate the reflected laser energy to the density scale length are restricted to a qualitative comparison for a given parameter scan[3,4].

In this Report we present experimental results in which the spatial distribution of the laser, reflected from the relativistic critical surface is measured at two different plasma density scale lengths. The divergence of the reflected laser beam is found to be related to the plasma density scale length. Using these results we demonstrate a novel experimental technique which provides a measure of the plasma density profile in the region of the relativistically corrected critical density.

II. Experimental Setup

The experiment was conducted on the Vulcan Petawatt laser facility at the Rutherford Appleton Laboratory. A 1 ps, 1054 nm pulse was generated with energy on target of 175 J and a contrast of 10^9 on the nanosecond time scale[5].

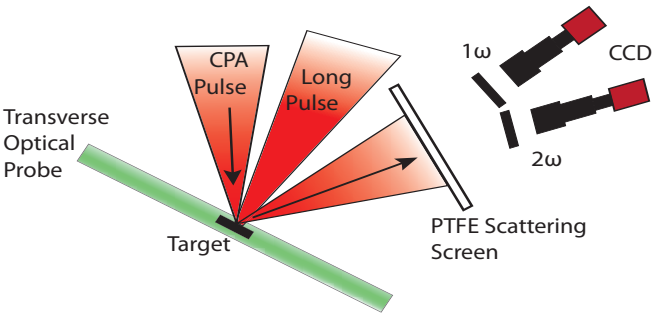

FIG. 1: Top view of experimental setup

The laser was focused by a f/3 OAP to a spot of ≈8 μm in diameter with a Gaussian spatial-intensity profile. In addition to the main CPA picosecond laser pulse a second (long pulse) laser with a 5 ns pulse duration and 6 J in the beam was used to generate a controlled 1D plasma expansion on the front surface of the target, prior to the

arrival of the short pulse. The long pulse laser was timed to arrive on target 1.5 ns before the short pulse.

The addition of a phase plate in the long pulse beam path produces a 270 μm focal spot with a top hat spatial-intensity profile. This configuration drives an approximately 1D shock, and plasma expansion. The combination of the very high contrast short pulse and the long pulse laser facilitates a high level of control over the front surface plasma density scale length. A transverse optical probe is used to image the plasma expansion on the front surface of the target. The probe beam was timed to coincide with the arrival of the short pulse laser on target. A schematic of the setup is shown in Fig.1.

In all of the shots presented here the target front surface consisted of a coating of plastic (5-15 μm thick).

The spatial profile of the laser pulse, specularly reflected from the critical surface, is measured using a PTFE scattering screen which is viewed in transmission with a CCD camera. The CCD has a zoom lens to image the screen and is filtered using a 1054nm bandpass filter. Further (neutral density) filtering is used to prevent saturation.

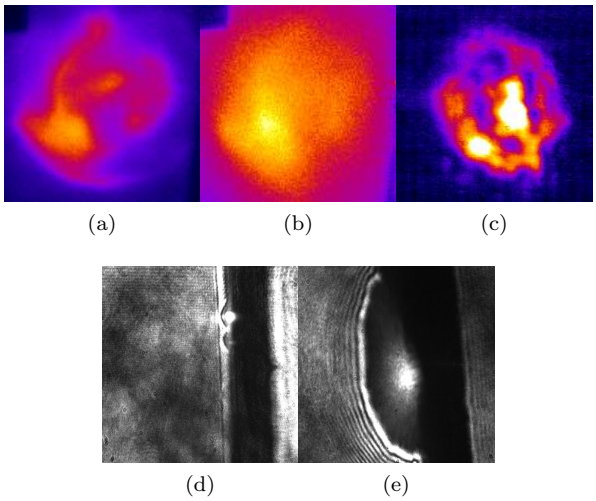

FIG. 2: Images of reflected beam hitting scattering screen (a) At short density scale length (b) At long density scale length (c) Laser spot, 100μm defocused. (d) Optical probe shadowgraphy for a typical short density scale length shot(e) Optical probe shadowgraphy for a typical long density scale length shot.

III. Results & Discussion

Example images of the reflected laser beam profile are shown in Fig.2(a) and (b) for short (no long pulse) and long (with long pulse) density scale lengths, respectively. There are distinct differences in the spatial-intensity profile between the two cases, specifically structures in the beam are smoothed out for long scale length preplasma. The similarity to the defocused laser spot, measured by replacing the target with a CCD with a microscope objective, (Fig.2(c)) is obvious and gives some confidence that the laser reflection from the critical surface is mirror-like at short density scale lengths and is modified by propagation through the underdense plasma at long density scale lengths. The mechanism which causes "smoothing" of the reflected beam is presently unknown. However, filamentation of the laser beam in the long density scale length plasma is expected, as is the formation of fine structure modulations in the critical surface[6]. Both effects are likely candidates for washing out structure in the reflected beam.

A lineout of the spatial-intensity profile is taken and a Gaussian distribution is fitted, as shown in the example in Fig.3. The effective f-number of the reflected beam is calculated using the $1/e^2$ diameter of the Gaussian fit and the distance from the target to the screen. The f-number for short density scale length preplasma is found to be 1.96±0.12, averaged over three comparable shots. At longer density scale lengths the f-number decreases to 1.54±0.1 (also averaged over three comparable shots). In both cases the reflected beam is significantly more divergent than the incoming beam which has an f-number of ≈3. That the reflected laser is found to be consistently more divergent at long density scale lengths compared to short density scale lengths indicates that the preformed, underdense plasma plays a key role in modifying the reflected laser.

Schumacher *et al*[7] investigate this effect with both PIC simulations and an analytical model. The model considers an idealised Gaussian spatial-intensity profile and treats the propagation through the preplasma, the reflection from the critical surface and the second transit through the preplasma as an optical system consisting of a lens, a mirror and a second lens. In the case of the preplasma, the "lens" is diverging as a result of the negative refractive index of the plasma. Due to the relativistic correction made to the critical density at the laser intensities used in this experiment the position of the critical surface varies along the spatial-intensity profile resulting in a curved critical surface. This effect becomes more extreme as the plasma density gradient is decreased (longer density scale length) due to the increased spatial separation of the critical surface at the wings of the pulse compared to the peak. In this way the diameter of the reflected laser beam is correlated to the density scale length of the front surface plasma and the curvature of the critical surface.

Previous experimental techniques rely on the use of a transverse optical probe beam to measure the preplasma density profile[8]. The drawback with this technique, in addition to the complicated deconvolution and setup, is that the critical density of the probe beam is significantly lower than the relativistically corrected critical density of the pump due to high degree of refraction of the optical beam near the critical density surface. The resulting measurement is restricted to the underdense region, with

the density profile of the overdense region being inferred from hydrodynamic simulations[9]. It has been shown in hydrodynamic simulations that the scale length of the underdense region, which can be optically probed, can be very different to the scale length in the region of the corrected critical density[9,10]. Instead, by measuring the divergence of the reflected light the plasma density profile is probed exactly up to the relativistic critical surface. In order to retrieve a quantitative measure of the density profile the emphasis is shifted from setting up the diagnostic in chamber and deconvolving the interferogram, via abel inversion, to applying the analytical model presented in Ref.7, which is an inherently simplier task.

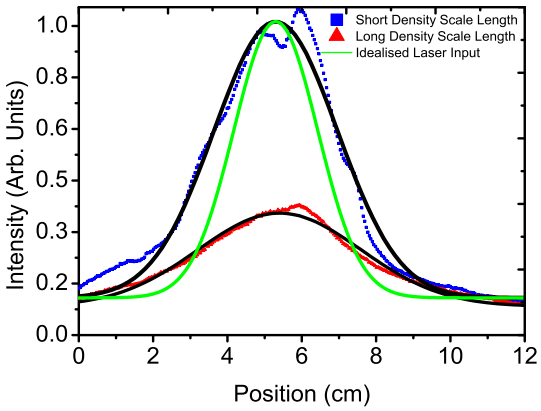

FIG. 3: Example Gaussian fits (black) to spatial-intensity profiles of reflected laser beams, for both short and long density scale lengths. Additionally, shown in green, an idealised laser profile with f-number equal to 3.

IV. Conclusion

In conclusion, we have described the application of a novel diagnostic of the front surface plasma density profile by measuring the divergence of the reflected laser spot. In principle this technique extends the measurable density range, beyond that covered by transverse optical probe interferometry, up to the relativistic critical density. The divergence of the reflected spot is found to be consistently larger at long density scale lengths. In both cases considered here (short and long density scale length) the divergence of the reflected spot is considerably larger than the incoming laser. A full quantitative analysis of these results, to determine the density scale length, is the subject of ongoing work.

[1]M. Tabak, J. Hammer, M. E. Glinsky, *et al. Phys. Plasmas*, vol. 1, no. 5, pp. 1626–1634, 1994.

[2]S. V. Bulanov, T. Z. Esirkepov, V. S. Khoroshkov, *et al. Phys. Lett. A.*, vol. 299, no. 2-3, pp. 240 – 247, 2002.

[3]A. S. Pirozhkov, I. W. Choi, J. H. Sung, *et al. Appl. Phys. Lett.*, vol. 94, no. 24, p. 241102, 2009.

[4]M. J. V. Streeter, P. S. Foster, F. H. Cameron, *et al. New. J. Phys.*, vol. 13, no. 2, p. 023041, 2011.

[5]I. Musgrave, W. Shaikh, M. Galimberti, *et al. Appl. Opt.*, vol. 49, no. 33, pp. 6558–6562, 2010.

[6]S. C. Wilks, W. L. Kruer, M. Tabak, *et al. Phys. Rev. Lett.*, vol. 69, pp. 1383–1386, Aug 1992.

[7]D. W. Schumacher, G. E. Kemp, A. Link, *et al. Phys. Plasmas*, vol. 18, no. 1, p. 013102, 2011.

[8]R. Benattar, C. Popovics, and R. Sigel *Rev. Sci. Instrum.*, vol. 50, no. 12, pp. 1583–1586, 1979.

[9]P. McKenna, D. Carroll, O. Lundh, *et al. Laser Part. Beams*, vol. 26, no. 04, pp. 591–596, 2008.

[10]D. C. Carroll, D. Batani, R. G. Evans, *et al. C. R. Phys.*, vol. 10, no. 2-3, pp. 188 – 196, 2009.

Scaling of ion spectral peaks in a hybrid RPA-TNSA regime

Contact *kkakolee01@qub.ac.uk*

K. F. Kakolee, S. Kar, D. Doria, B. Qiao, M. Geissler, B. Ramakrishna, G. Sarri, K. Quinn, M. Zepf, M. Borghesi

School of Mathematics and Physics, Queen's University of Belfast, Belfast, BT7 1NN, U. K

A. Macchi

CNR/INFM/polyLAB, Pisa, Italy
Dipartimento di Fisica "Enrico Fermi", Universit`a di Pisa, Largo B. Pontecorvo 3, I-56127 Pisa, Italy

J. Osterholz, M. Cerchez, O. Willi

Heinrich Heine-Universitat Dusseldorf, Germany.

X. Yuan, P. McKenna

SUPA, Department of Physics, University of Strathclyde, Glasgow *G4 ONG, U. K.*

Introduction

Laser-driven ion acceleration has been a rapidly progressing field of great interest since the first observations [1] of energetic ion beams from laser-irradiated foil targets. High quality ion beams have many prospective applications in scientific, technological and medical areas such as medical isotope production, tumor therapy, ultrafast radiography and laser-driven fusion [2]. For the interaction of a laser with solid-density targets, several ion acceleration mechanisms have been identified and investigated. Among them the two most discussed are Target Normal Sheath Acceleration (TNSA) and Radiation Pressure Acceleration (RPA).

Ion beams with energies of several tens of MeV have been obtained in experiments via the TNSA mechanism [1, 3, 4], where the ions are driven by the sheath fields established at the target rear surface, due to the relativistic electrons produced at the target front surface during the intense laser interaction. However, low particle density, large divergence, and almost 100% energy spread of the proton beam poses significant limitations for many of the envisioned applications, for instance hadron therapy of deep-seated cancers. By contrast, ion beam production by the radiation pressure of intense lasers has been predicted to be a promising route for accelerating large numbers of ions quasi-monoenergetically to ''relativistic'' energies (GeV/nucleon range), in a significantly more efficient manner compared to TNSA [5-7].

There are two regimes of RPA, viz. hole-boring (HB) and Light sail (LS), which have been identified by simulations and recent experimental results [8]. In the RPA mechanism, ions are accelerated by directional momentum transfer from laser to target via the laser's ponderomotive force, which acts as a snow-plow on the target front surface and launches a dense ion bunch into the target. The radiation pressure instantly pushes the electrons in the skin depth which sets a strong accelerating field for ions to follow promptly the electrons. Consequently, the laser pulse bores through the target (Hole-boring (HB) regime) where the ion front velocity (*hole boring velocity*) depends on the laser intensity (I) and target mass density (ρ). If the target thickness is less than the product of the laser pulse duration and hole boring velocity, the ions will pile up at the target rear surface before the end of the laser pulse. As the thickness of the compressed layer becomes comparable or less than the evanescence length of the ponderomotive force, the whole layer is cyclically accelerated with high efficiency for the rest of the duration of the intense laser pulse. The latter scenario of whole foil acceleration is called *light-sail* (LS) regime.

In the experiment mentioned here, both the Hole-boring (HB) and Light sail (LS) regimes of RPA have been extensively explored employing the Vulcan Petawatt laser. For thick targets, where the product of the HB velocity and the laser pulse duration is less than the target thickness, collimated ion jets were observed, emerging from the rear surface of the targets over a hydrodynamic time scale [9]. On the other hand, for sufficiently thin targets, the LS mechanism resulted in narrow band heavy ion spectra with energy up to 20 MeV/nucleon, which is discussed in this report. The scaling for ion energy is obtained by varying the laser and target parameters over several shots.

Experimental Setup

The experiment was carried out using the VULCAN Nd:glass laser, operating in chirped pulse amplification (CPA) mode. The laser wavelength and full width at half maximum (FWHM) pulse duration are 1.053 µm and 750 fs respectively. The laser was focused down on the target at near normal incidence by using an *f*/3 off-axis parabola. In order to reduce the pre-pulses and to suppress the intensity of amplified spontaneous emission, a plasma mirror was employed before the target. A schematic of the experimental setup is shown in the Fig. 1. A zero order quarter wave plate was used in the focusing beam, before the plasma mirror, in order to change the polarisation of the laser on the target. The intensity on the target was varied from 5×10^{19} W/cm^2 to 3×10^{20} W/cm^2 by increasing the laser spot size on the target, by translating the parabola along the focussing axis. Targets of various materials (Cu, Al, Au and CH) and thickness (10 µm down to 100 nm thickness) were used.

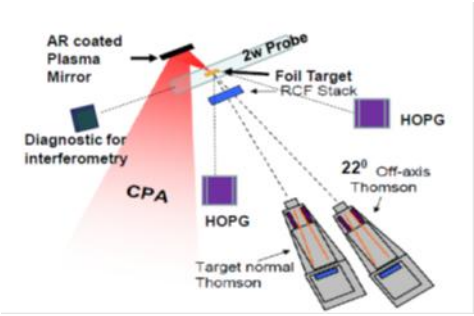

Fig 1. Schematic of the experimental set up.

Thomson Parabola Spectrometers (TP –Spec) were employed as the main diagnostic for measuring spectra of multi-MeV ions produced by the interaction. Two high resolutions TP –Spec were fielded, one along the target normal direction and the other looking at 22^0 off axis to the target normal. Image plates (IP) were used as detectors to record the spectra. IP were cross calibrated with solid state nuclear track detector (CR39) for absolute particle number determination. The energy resolved spatial flux profile of protons was diagnosed by using stacks of radiochromic films (RCF) placed in the bottom half of the beam.

Result and Discussions

Spectra of accelerated ions of different species resulting from the interaction were diagnosed for different laser and target parameters over many shot. We detected not only ions of the main target components, but also, as usual in these experiments, several other ion species such as C, O, H present in surface contaminant layers. Instead of the quasi maxwellian energy spectra typically observed in case of TNSA, the spectra from thin targets contains a peaked feature towards the higher energy side.

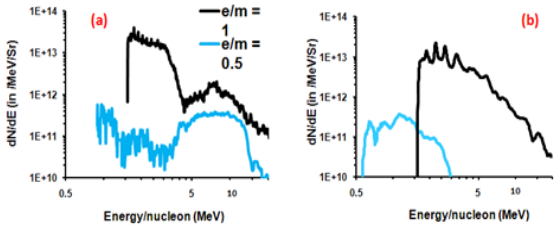

Fig 2. Experimental obtained spectra of two ion species for (a) thin (100 nm) and (b) thick (10 um) Cu targets irradiated at similar laser intensity

Since for the thin targets, the HB accelerated ions from the target front surface are expected to reach the target rear surface in less than the laser pulse duration (0.1 ps for the case shown in the fig. 2(a)), the remaining duration of the CPA pulse is spent in accelerating the ions in the LS regime. We believe that this is the cause of the peaked spectral feature observed in the spectra. On the other hand, for thicker targets we obtained exponential ion spectra (fig. 2 (b)) typical to TNSA mechanism.

It is most likely that the proton spectral profile in fig. 2(a) results from the overlap of a narrow band proton spectrum originated by the LS mechanism, with an exponential spectrum by TNSA mechanism taking place over an extended area (of several 100s of micron) on the target rear surface, due to recirculation of hot electrons [10]. However, such an exponential feature is not prominent in the spectra for the species with e/m=0.5 (which could correspond to fully ionized Carbon), as protons get preferentially accelerated by the TNSA mechanism. The dominance of proton acceleration in a "pure" TNSA scenario can in fact be seen in the fig. 2(b).

Ion energy attained by the LS mechanism scales with the ratio between laser intensity and target areal density, given by [7, 11, 12]

$$\beta_{LS} = \frac{(1+\psi)^2-1}{(1+\psi)^2+1} \quad , \text{ where } \psi = 2\pi \frac{Z}{A}\frac{m_e}{m_p}\frac{a_o^2\tau_{LS}}{\zeta}; \qquad (1)$$

Here $a_o = 0.85\sqrt{I\lambda^2/10^{18}\,Wcm^{-2}\mu m^2}$ is dimensionless laser amplitude; λ is the laser wavelength, , n_e and l are the electron density and thickness of the compressed layer. τ_{LS} is the duration of the laser pulse used for LS acceleration. Z and A are the atomic number and mass number of the target ions, and, m_e and m_p are the masses of an electron and proton respectively.

Using the laser and target parameters relevant to the case shown in the Fig. 2(a) in a simple numerical model based on the equation (1), we found that an ion energy of 8 MeV/nucleon is expected by the LS mechanism, which agrees well with the experimental data (see the data point 'A' in the Fig. 3). A particle-in-cell simulation carried out for scaled down laser and target parameters also shows a quasi-monoenergetic peak in the ion spectra at around 10 MeV/nucleon, which further substantiates the role of LS mechanism during the interaction.

The scaling of the spectral peak has been obtained by a methodical scan over a range of target thickness, density, laser intensity and polarization. Fig 3 shows the energy scaling of the ion peak with the relevant scaling parameter $a_o^2\tau_{LS}/\zeta$. We can also see that, there is a good agreement between experimental data and RPA estimations. The experimental data points show that the ion energy scales with $(a_o^2\tau_{LS}/\zeta)^{1.5}$, which is significantly faster than the TNSA scaling, $E \propto a_o$.

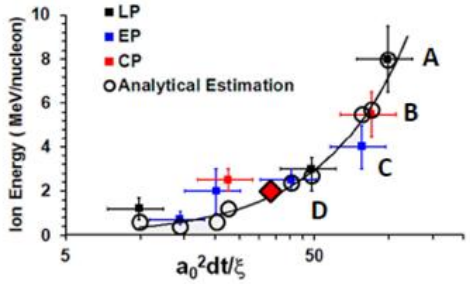

Fig 3. Graph showing the peak energy (/nucleon) of the ion species with e/m=0.5. The red diamond with the black outer line represents the previously reported experimental data by Henig et. al. [8]. The experimental parameter set (intensity, target material, target thickness) for the data points marked as A, B, C and D are (3×10^{20} W/cm^2, Cu, 0.1μm), (1.25×10^{20} W/cm^2, Cu, 0.05μm), (2.2×10^{20} W/cm^2, Cu, 0.1μm), (6×10^{19} W/cm^2, Al, 0.1μm) respectively. The circles represent the results from simple numerical modeling based on the eq. (1) . Data point 'A' corresponds to the case shown in the Fig. 2(a).

Conclusion

The role of the radiation pressure of an intense laser beam in the formation of narrow band proton and carbon spectra from thin foils has been discussed. The data presented suggests that the onset of the LS regime of RPA can be obtained, for suitably thin targets, at currently available laser intensities, in competition with the TNSA mechanism.

Acknowledgements

This work was funded by EPSRC (LIBRA Consortium, Grant No: EP/E035728/1) and by STFC Facility access. We acknowledge the support and contribution of the Target Preparation Laboratory, TAP laser staff and the Engineering workshop at CLF, RAL.

References

[1] E. L. Clark et al., Phys. Rev. Lett. 84, 670, (2000); A.Maksimchuk et al., ibid. 84, 4108 (2000).

[2] M. Borghesi *et al*, Fusion Science and Technology, 49, 412 (2006) and thereferences therein.

[3] B. M. Hegelich et al., Nature (London) 439, 441 (2006).

[4] H. Schwoerer et al., Nature (London) 439, 445 (2006).

[5] A. Macchi, F. Cattani, T. V. Liseykina, and F. Cornolt, Phys. Rev. Lett. 94, 165003 (2005).

[6] A. P. L. Robinson, M. Zepf, S. Kar, R. G. Evans, and C. Bellei, New. J. Phys. 10, 013021 (2008).

[7] B. Qiao, M. Zepf, M. Borghesi, and M. Geissler, Phys. Rev. Lett. 102, 145002 (2009).

[8] A. Henig *et. Al*, Phys. Rev. Lett. 103, 245003 (2009); C. Palmer et al, Phys. Rev. Lett, 106, ISSN:1079-7114 (2011)

[9] K. F. Kakolee *et. Al, CLF-RAL Annual Report 2010*.

[10] F. N¨urnberg *et al*, Rev. Sci. Instr., **80**, 033301 (2009).

[11] A. Robinson et. al., New. J. Phys. 10, 013021 (2008.

[12] A. Macchi et., al., Phys. Rev. Lett. 94, 165003 (2005); A. Macchi et. al, New J Phys., 12, 045013 (2010).

Reflectivity Measurements in Ultraintense Laser-Plasma Interactions

Contact *david.maclellan@strath.ac.uk*

D. A. MacLellan, D. C. Carroll, G. Scott* and P. McKenna

Department of Physics, University of Strathclyde, SUPA, Glasgow G4 0NG

M. J. V. Streeter, N. Dover, S. Nagel, C. Palmer and Z. Najmudin

Department of Physics, Imperial College London, LONDON, SW7 2AZ

S. Kar, R. Prasad, K. F. Kakolee, H. Ahmed, D. Doria and M. Borghesi

School of Mathematics and Physics, Queen's University Belfast, Belfast BT7 1NN

M. Notley, R. Heathcote and D. Neely

**Central Laser Facility, STFC Rutherford Appleton Laboratory, Oxfordshire, OX11 0QX*

J. Schreiber

Fakultät für Physik, Ludwig-Maximilians-Universität München, D-85748 Garching, Germany and
Max Planck-Institut für Quantenoptik, Hans-Kopfermann-Str. 1, D-85748 Garchin

1. Introduction

The physics of high intensity laser-plasma interactions is of fundamental importance to a number of applications that require an understanding of extreme states of matter, such as those present in ion acceleration [1] and the Fast Ignition [2] approach to Inertial Confinement Fusion.

However, the physics of front surface plasma dynamics is extremely challenging. The various absorption mechanisms, relativistic movement of the particles and complex energy transport provide a complicated backdrop in which to analyse experimental results.

When an ultraintense laser pulse of intensity $>10^{18}$Wcm^{-2} impinges on the surface of a solid target, the energy content of the pulse pedestal is sufficient to ionize the front surface of the target prior to the arrival of the main, high intensity pulse. This preformed plasma has unique properties such as high density, on the order of solid density, and high temperature (~10-100eV). The incident, high intensity laser pulse will propagate through this preformed, underdense plasma up until a critical density, where the laser frequency is equal to the electron plasma frequency. At this point, known as the critical density, the laser can no longer penetrate the plasma and is instead reflected. Measurement of spectral modulations of this reflected laser light gives an excellent diagnostic of plasma kinematics in the vicinity of the critical surface, and can highlight effects such as hole boring [3].

In this report, we describe spectral measurements of backreflected light from laser-plasma interactions at intensities $>10^{20}$Wcm^{-2}. We show that these measurements can give an indication of the the critical surface dynamics under intense laser drive. Preliminary examination of the underlying physics is given, as well as potential future directions for this research.

2. Experimental Setup

The experiment was undertaken using the Vulcan Laser, in the Target Area Petawatt (TAP) chamber. In the TAP configuration, the laser delivers 450J before compressor in approximately 1ps. For the experiment detailed in this report, the intensity on target is calculated to be approximately $4x10^{20}$Wcm^{-2}. The experimental chamber setup is shown in Figure 1. The incident, high intensity pulse is directed by a turning mirror to an f/3 off-axis parabolic mirror (OAP) where it is focused to a diffraction limited spot diameter of approximately 4μm. Measurements were made by collecting the laser light that is reflected from the surface of the interaction.

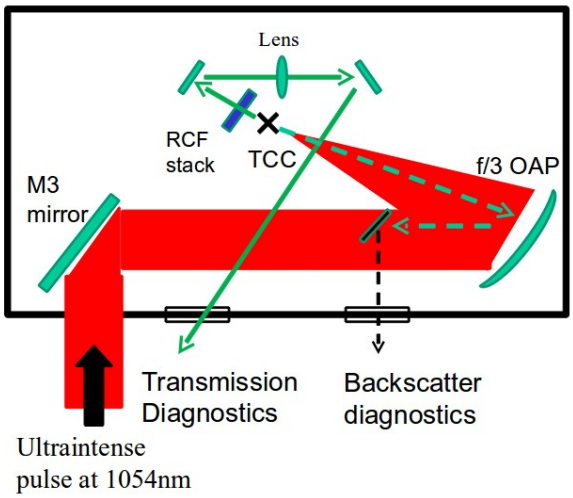

Figure 1 - Experimental Setup. The black cross defines TCC, with the reflected spectra being collected from the OAP and directed to external diagnostics. The RCF stack and transmission diagnostics are also shown.

The diagnostic arrangement used to collect the backscattered light is shown below in Figure 2.

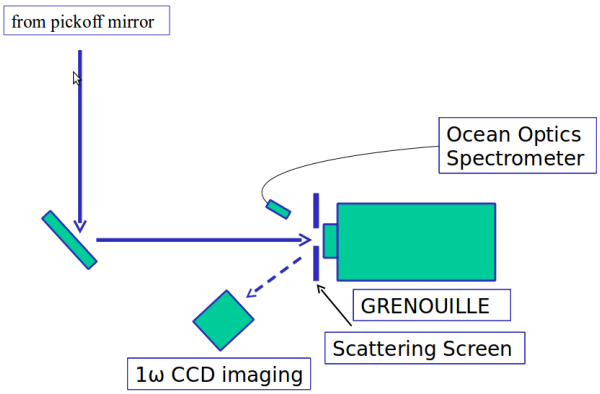

Figure 2 - Backscatter diagnostics, showing the backscattered laser light directed to the entrance of the GRENOUILLE, where the spectrum collected from a scattering screen.

A 2” silvered mirror, positioned in the shadow of the optical probe collection optics in the main beam, collects a portion of the light that is reflected back along the laser axis from the target and re-collimated from the OAP. This reflected beam is then directed outside the chamber to the diagnostics shown in Figure 2: a 1ω imaging Firewire camera, GRENOUILLE autocorrelator and a fiber spectrometer. The results in this report are obtained using the fiber spectrometer, which collects the diffusely scattered, backreflected light at 5cm from a scattering screen surrounding the GRENOUILLE entrance. The spectrometer is an Ocean Optics MayaPro 2000, with an HC1 grating with 300 lines/mm, a 10μm slit, an optical range of 200-1100 nm and a resolution of 0.32 nm/pixel .

In this experiment, the parameters that were varied were:

1. Target thickness and material
2. Contrast (clean pulse created by Plasma Mirror [4])
3. Polarization

This report will only consider the effect of target thickness on the backscattered spectrum. Analysis is currently ongoing to understand the effect of varying pulse contrast and polarization. The laser pulse parameters including p-polarization, pulse contrast (no plasma mirror), laser energy and intensity, and angle of incidence of 2° to target normal were kept fixed.

3. Results and Discussion

Before we consider the variation of target thickness, we first report on measurements of the incident pulse spectrum. This is shown below in Figure 3.

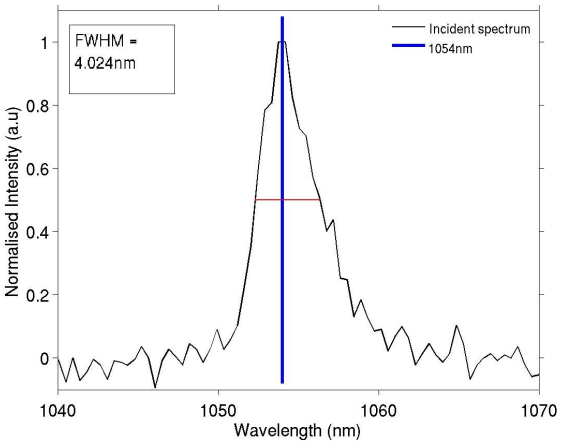

Figure 3 - Incident spectrum. The blue line represents the fundamental wavelength of 1054nm and the red line represents the FWHM of 4.025nm.

We see that the spectral shape of the incident pulse is centered at 1054nm with a FWHM of 4.024nm, as shown by the red line at the half maximum value. All subsequent analysis will be undertaken in reference to this incident pulse. In all these spectra, a positive (+) line shift represents red-shifting, where line shift corresponds to a shift of the peak intensity while linewidth corresponds to a broadening of the peak.

Results from different thicknesses of carbon target for the reflected fundamental and second harmonic are shown in Figure 4 and 5 respectively.

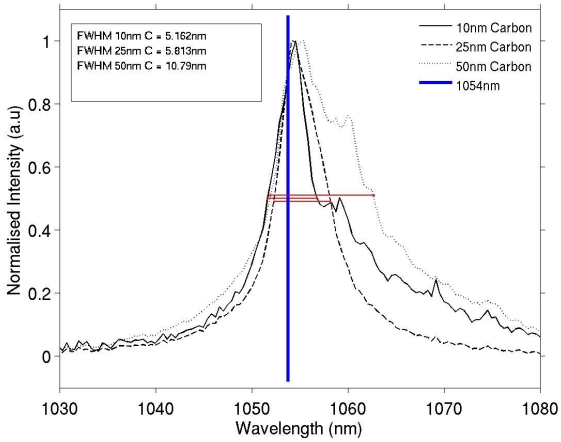

Figure 4 - Reflected fundamental wavelength from carbon targets of varying thickness. The blue line represents the central wavelength of 1054nm, while the red lines represent the FWHM of each target, displaced for clarity.

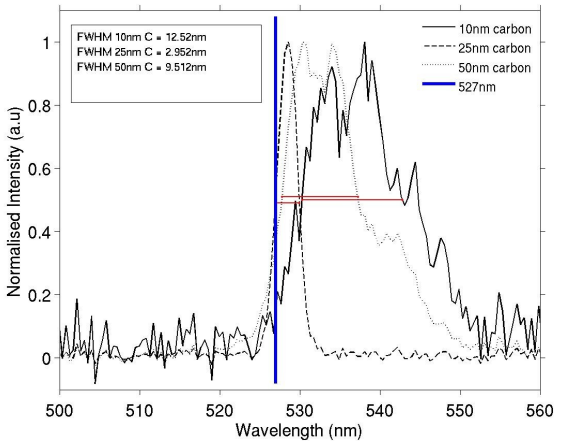

Figure 5 - Reflected second harmonic wavelength from carbon targets of varying thickness. The blue line represents the second harmonic wavelength of 527nm, while the red lines represent the FWHM of each target, displaced for clarity.

The experimental data are summarised below in Table 1.

Target Thickness (nm)	1ω		2ω	
	$\Delta\lambda_{1\omega}$ (nm)	$\delta\lambda_{1\omega}$ (nm)	$\Delta\lambda_{2\omega}$ (nm)	$\delta\lambda_{2\omega}$ (nm)
10	5.162	+0.55	12.52	+11.10
25	5.813	+0.10	2.952	+1.55
50	10.79	+1.40	9.512	+5.18

Table 1 - Experimental results for the reflected fundamental (1ω) and second harmonic (2ω) wavelengths. In this table, Δλ represents linewidth modulations and δλ represents line shifts.

Upon increasing target thickness, an increasing linewidth broadening and shifting of the fundamental harmonic spectra is observed. We see a steady increasing linewidth of 5.162nm to

10.79nm and line shift increase from +0.55nm to +1.40nm, with a slight reduction to +0.10nm for 25nm carbon. The increasing red shifting suggests an increasing hole boring velocity for thicker targets, while increasing linewidth suggests that acceleration is greater for thicker targets.

The second harmonic spectra are observed to be much more sensitive to spectral modulations and shifts than the reflected fundamental. This observation is consistent with previous literature [5, 6]. We will therefore analyse the line shifts of the second harmonic, as in previous work [5]. For the reflected second harmonic, we see a decrease in line shift from +11.10nm for 10nm to +5.18nm for 50nm, with 25nm displaying a red-shifted peak of +1.55nm. Using the relativistically corrected Doppler equation, this corresponds to recession velocities between $9x10^{7}cms^{-1}$ and $7x10^{8}cms^{-1}$. For increasing thickness, we observe a decrease in linewidth from 12.52nm at 10nm thickness, to 9.512nm at 50nm, with 25nm displaying the largest narrowing of 2.952nm. Again, the linewidth gives an indication of the acceleration profile of the critical density region.

In summary, for all of the reflected spectra we observe a significant departure from the 4.024nm FWHM of the incident pulse. This indicates that the critical surface movement is determined by a complex interplay between critical surface acceleration and transitions between blue-shifted coronal expansion and red-shifted hole boring.

4. Conclusions and Future Work

In conclusion, measurements are presented of backscattered spectra from laser-produced plasma. The measurements show spectral line shifts, linewidth broadening and spectral modulations for varying target thickness for both the reflected fundamental and second harmonic. These spectral shifts correspond to a Doppler hole boring velocity varying between $9x10^{7}cms^{-1}$ and $7x10^{8}cms^{-1}$ which is in agreement with previous experimental results [5, 6] and the current analytical model [3].

4.1 Future Work

From the results presented in this report, we can clearly see that reflectivity measurements in ultraintense laser-plasma interactions offer a promising diagnostic of the interaction environment in the vicinity of the critical surface. This report details a pilot study. In order to fully quantify the physics behind these processes, dedicated shots must be taken with parametric scans of target thickness and material for a wide range of thicknesses (from 10nm to 1μm), incidence angle, polarization and incident pulse contrast. We will also test the validity of the analytical model at intensities greater than those previously studied [4, 5], and study the effect that the transition to relativistic intensities has on the back reflected spectra. By extending the range of intensity, we may perhaps begin to enter regimes where Radiation Pressure Acceleration (RPA) [8] begins to dominate. This may be observed by an extreme red-shifted, backreflected spectra, as the light pressure of the incident pulse drives the macroscopic critical density surface inwards.

4.2 Chirp and Acceleration

While considerations of the critical surface movement by relating the red and blue line shifts to a Doppler velocity seem reasonable, recent research [7] has shown that we should consider the broadening of each peak instead of the instantaneous velocity that is given by the line shift. Depending on the linewidth and chirp of both our incident and reflected pulses, a measure of the acceleration of the critical density surface can be obtained, giving an indication of the direction and magnitude of the acceleration. Since we are collecting the reflected light from a moving source, a measurement of the chirp of the reflected light will give a measurement of the acceleration. Analysis is currently ongoing to determine the role that acceleration plays in critical density surface dynamics.

5. Acknowledgements

This work was supported by the Engineering and Physical Sciences Research Council. We acknowledge the support and contribution of the Target Preparation Group, Vulcan laser staff and the Engineering workshop at the Central Laser Facility, RAL.

6. References

1. M. Borghesi *et al.*, Fusion Science and Technology, vol. 49, p. 412 (2006)
2. R. Kodama *et al.*, Nature, 412 (6849): 798-802 (2001)
3. S.C. Wilks, W.L. Kruer, M. Tabak, and A. B. Langdon, Phys. Rev. Lett. **69**, 1383 (1992)
4. G. Doumy *et al.*, Physical Review E, vol. 69, p. 026402 (2004)
5. M. P. Kalashnikov *et al.*, Phys. Rev. Lett. **73**, 260 (1994)
6. M. Zepf *et al.*, Phys. Plasmas, **3**, 3242-3244
7. R . Saurbrey, Phys. Plasmas **3**, 4712 (1996)
8. A.P.L. Robinson *et al*., New Journal of Physics **10**, 013021 (2008).

Lattice structure effects on energetic electron transport in solids

Contact *david.carroll@strath.ac.uk*

D.C. Carroll, M.N. Quinn, X.H. Yuan[#], C.M. Brenner[*], M. Coury, P. Gallegos[*], R. J. Gray, O. Tresca, P. McKenna

SUPA, Department of Physics, University of Strathclyde, Glasgow G4 0NG, UK

[#]***present address:****Key Laboratory for Laser Plasmas (Ministry of Education) and Department of Physics,Shanghai Jiao Tong University,Shanghai 200240, China*

A. P. L. Robinson, K. Lancaster, D. Neely,

[*]*Central Laser Facility, STFC Rutherford Appleton Laboratory, Oxfordshire OX11 0QX, UK*

M. P. Desjarlais

Sandia National Laboratories, P.O. Box 5800, Albuquerque, New Mexico 87185, USA

M. Burza, C.-G. Wahlström

Department of Physics, Lund University, P.O. Box 118, S-22100 Lund, Sweden

X.X. Lin, Y. T. Li

Beijing National Laboratory of Condensed Matter Physics, Institute of Physics, CAS, Beijing 100190, China

Introduction

Improving our understanding of the physics of energetic (‘‘fast’’) electron transport in dense matter is critical for many applications in high energy density physics. Examples include the fast ignition approach to inertial confinement fusion [1], the development of laser-driven ion sources [2], and for laboratory astrophysics. During the interaction of an ultraintense ($> 10^{19}$ Wcm^{-2}) laser pulse with a solid target, a significant fraction of the laser energy is absorbed, producing a multimega-ampere current of relativistic electrons. Due to instabilities in the transport of this current, filamentation of the electron beam can occur during propagation. There are a number of plasma instabilities that can result in filamentation, including the Weibel [3,4], two-stream [5], and resistive filamentation instabilities [6].

It is well known from solid state physics that the conductivity of a material is strongly affected by its lattice structure [7]. The propagation of a high current of fast electrons in a solid target irradiated by a high energy picosecond laser pulse requires, by charge neutrality, a ‘‘return’’ current of thermal electrons which are collisional. This return current rapidly, on the order of picoseconds, heats the target to temperatures in the range 1–100 eV. Due to this rapid heating a nonequilibrium state of warm dense matter (WDM) occurs in which the electrons are ‘‘warm’’ (1–100 eV) but the ions remain essentially cold and maintain temporarily the structural arrangement they possessed in the condensed matter state. The conductivity of the material in this transient nonequilibrium state is strongly affected by the retained lattice structure of the ions.

In this report we demonstrate the effects of lattice structure on the electron propagation through a solid target. Using various allotropes of a single element, carbon, it is shown that lattice structure alone can determine whether or not fast electron beam filamentation occurs in solid targets irradiated by intense picosecond laser pulses. It is shown that for the highly ordered carbon allotrope, diamond, a metallic-like propagation of the electron beam occurs, indicating a transient state of diamond. In contrast, for the disordered allotropes of carbon, undergoing a similar laser interaction, it is shown that the electron beam suffers filamentation similar to that typically associated with plastic targets. The report presents an overview of the paper by McKenna *et al* [8]

Experiment

The experiment was performed using the Vulcan laser, delivering pulses of 1.053 μm wavelength light, with an energy of 200 J (on target) and duration equal to 1 ps, FWHM. The p-polarized pulses were focused to an 8 μm diameter FWHM spot, to a calculated peak intensity of 2×10^{20} Wcm^{-2}. The main target samples were three different allotropes of carbon: (1) single-crystalline diamond, (2) vitreous carbon (disordered), and (3) pyrolytic carbon. Pyrolytic carbon is similar to graphite but with some degree of covalent bonding between its graphene sheets, thus presenting an intermediate degree of atom ordering. Figure 1 illustrates these structural differences. Aluminium and plastic (Mylar) targets were also used as reference materials due to the differences in their ordering and room temperature electrical conductivity. The target size in all cases was 5 mm×5 mm and 500 μm thick.

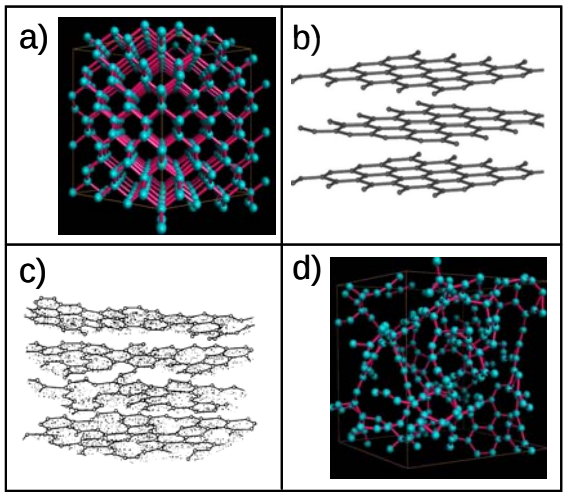

Fig 1. Different carbon allotropes: a) diamond with a tetrahedral crystalline structure with strong covalent bonds resulting in a very high room temperature electrical resistivity (image from quantum molecular dynamic calculations). b) graphite is stacked graphene layers that have strong bonds within the layers but weak bonds between the layers. These weak bonds enable graphite to be conducting parallel to the layers (image [9]). c) pyrolytic carbon is similar to graphite but the graphene layers are disrupted (image [10]). d) vitreous (glassy) carbon is highly disordered but the majority of bonds are covalent resulting in a higher resistivity than graphite (image from quantum molecular dynamic calculations).

The fast electron transport pattern was inferred by recording and analyzing the spatial-intensity profile of the proton beams accelerated from the target rear surface. The acceleration is a result of an electrostatic sheath field established by the fast electrons at the target rear surface [2]. Fuchs et al. [11] have previously demonstrated that modulations in the sheath field, as

a result of filamentation of the electron beam within the target, are mapped into the expanding proton beam spatial-intensity distribution. A stack of dosimetry film, which enables measurement of the dose deposited by the proton beam at discrete energies given by the stopping range of protons within the stack, is used to measure the proton beam profile. Each piece of film was optically scanned and the modulations within the proton dose were quantified.

Results

It was found that the different allotropes of carbon produce very different proton beam patterns indicating differences in the fast electron transport patterns. In figure 2 examples of the proton beam spatial-intensity profiles for diamond and vitreous carbon are shown. Notice the smooth spatial-intensity profile for diamond in figure 2a). This profile is normally associated with metallic targets, such as aluminium, rather than insulators. The highly structured proton beam profile, see figure 2b), for vitreous carbon is more typical of that associated with insulator targets. Figure 2(c) shows the variance in proton dose (normalized to the average dose level) for the range of targets explored against the targets room temperature electrical conductivities. Larger variance values correspond to a more structured proton beam and therefore more filamentation of the electron beam. In figure 2c) there is no clear pattern associated with room temperature electrical conductivity and beam variance. When the results are plotted, from left to right in figure 2d), in terms of increasing degree of initial order of the atoms in the target material a clear trend is observed. The proton beam becomes more uniform, indicating less electron beam filamentation, with increasing atom order. As noted above, heavy filamentation is observed for vitreous carbon while pyrolytic carbon, with an intermediate degree of atom ordering, produces intermediate levels of beam filamentation. Repeat shots were taken on each of the carbon allotropes and the results are fully reproducible, as shown in figure 2c) and d). These results are explained by the effect of lattice structure on electrical conductivity and the fact that the structure is temporarily maintained during rapid thermal excitation of the material [12].

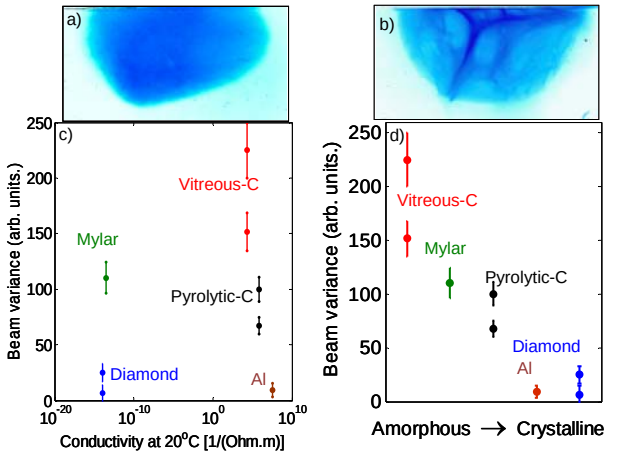

Fig 2. Spatial-intensity profile measurements (lower half) of the proton beam, at energy 10 MeV, for (a) diamond and (b) vitreous carbon. c) Variance in the proton signal (mean of 10 samples) near the centre of the proton beam, for given target materials with increasing room temperature conductivity left to right. d) Variance in the proton signal with increasing atom ordering from left to right. Error bars correspond to statistical variations over the multiple samples.

Modelling

To investigate this in more detail, the electronic structure and electrical conductivity of two different allotropes of carbon were modelled: diamond [tetrahedral lattice; figure 1a)] and vitreous carbon [disordered; figure 1d)] as a function of temperature. The electrical conductivities were derived using quantum molecular dynamics calculations as described in reference [8].

Figure 3a) shows the calculated conductivity as a function of temperature for both carbon allotropes. Diamond is strongly insulating at room temperatures due to the large gap between its valence and conductance bands. However, the electrical conductivity rises sharply with the electronic temperature as soon as the electrons are excited enough to reach above the band gap. In contrast, the conductivity of vitreous carbon, which is low but finite at ambient conditions, rises only weakly with increasing electronic temperature, even when heated in the same way. In the transient WDM regime (~10 eV), the electrical conductivity of diamond becomes nearly 2 orders of magnitude greater than that of the disordered carbon. At even higher temperatures (>100 eV), the conductivities rise sharply for both materials.

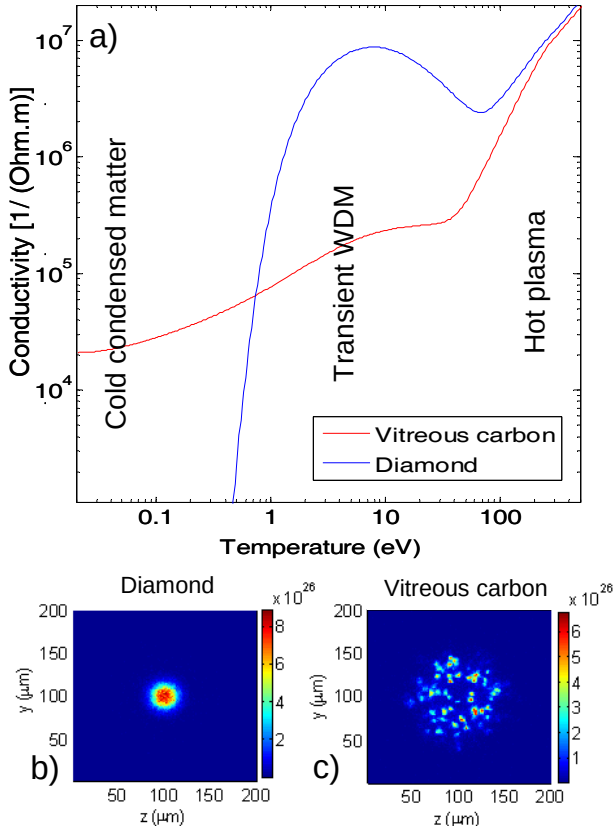

Fig 3. a) Calculated electrical conductivity as a function of temperature for diamond and vitreous carbon. Fast electron transport simulation results (electron density at the rear of the targets) for b) diamond and c) vitreous carbon after 1.5 ps (when the main part of the current has reached the rear surface). Smooth transport is observed with diamond, compared to heavily filamented transport in vitreous carbon.

The physical origin of the effects of atom ordering on electrical conductivity in the nonequilibrium regime centres on the electron mean free path in the material [7]. If the ions are highly disordered, then electrons will scatter incoherently and the electron mean free path will be limited to the mean interionic distance, leading to a low conductivity. If, however, the ions are in a well-ordered geometric lattice, then constructive interference of the scattering of the wave function from multiple ions results in a mean free path considerably longer than the mean interionic distance. Thus, for an ordered structure of ions the material conductivity is larger than for a disordered material of the same atomic element, and similar density. At very high temperatures (> 100 eV) the scattering cross sections diminish

rapidly with increasing mean electron momentum, typical of Coulomb scattering processes, and hence the conductivity increases irrespectively of atom ordering.

Next we consider how the calculated differences in electrical conductivity affect the propagation of fast electrons by performing simulations using the 3D ZEPHYROS particle-based hybrid code [13]. Simulation details can be found in McKenna *et al* [8] Example simulation results are shown in figure 3b-c), in which 2D slices of the fast electron density in the y-z rear plane are plotted (i.e. rear surface of target). In the simulation of diamond, the fast electron beam is smooth and nonfilamented along its whole length and in its transverse profile at the rear surface. In clear contrast to this, the results of simulations for vitreous carbon show a beam that is filamented along most of its length and exhibits a strongly filamented transverse profile at the rear surface. The simulations start at a temperature of 1 eV and the conductivity curves converge at >100 eV, and therefore the predicted differences in electron transport result entirely from the differences in conductivity of the two targets in the transient WDM regime.

Conclusions

In summary, these results show that in the interaction of a short high intensity laser pulse with a solid target the effects of lattice structure need to be considered. The electrical conductivity of the induced transient WDM state is shown to be determined by the atomic ordering in a material and plays a key role in the transport of fast electrons within the target. For the many potential applications of high power laser-solid interactions involving the conduction of large currents of energetic electrons these results have significant implications. It shows that the choice of allotrope of a given element is important, which impacts on the choice of materials used in the fabrication of advanced targets for applications such as the fast ignition scheme [14] for fusion and laser-driven ion acceleration. Further details can be found in McKenna *et al* [8].

Acknowledgements

We acknowledge the expert support of the staff at the Central Laser Facility of the Rutherford Appleton Laboratory and the use of computing resources provided by the STFC e-Science Facility. We also acknowledge discussions with Professor R. Bingham and Professor A. R. Bell. This work is supported by EPSRC (Grants No. EP/E048668/1 and No. EP/E035728/1), the Swedish Research Council, and by the National Basic Research Program of China (program 973; Grant No. 2007CB815101).

References

[1] M. Tabak *et al*., Phys. Plasmas **1**, 1626 (1994).

[2] M. Borghesi *et al*., Fusion Sci. Technol. **49**, 412 (2006).

[3] E. S. Weibel, Phys. Rev. Lett. **2**, 83 (1959).

[4] Y. Sentoku *et al*., Phys. Rev. Lett. **90**, 155001 (2003).

[5] B. Hao *et al*., Phys. Rev. E **79**, 046409 (2009).

[6] L. Gremillet, G. Bonnaud, and F. Amiranoff, Phys. Plasmas **9**, 941 (2002).

[7] J. M. Ziman, Adv. Phys. **16**, 551 (1967).

[8] P. McKenna *et al*., Phys. Rev. Lett. **106**, 185004 (2011).

[9] en.wikipedia.org/wiki/File:Diamond_and_graphite2.jpg

[10] C. S. Yoon, Thesis, Massachusetts Institute of Technology (1995)

[11] J. Fuchs *et al*., Phys. Rev. Lett. **91**, 255002 (2003).

[12] V. Recoules *et al*., Phys. Rev. Lett. **96**, 055503 (2006).

[13] S. Kar *et al*., Phys. Rev. Lett. **102**, 055001 (2009).

[14] R. Kodama *et al*., Fusion Sci. Technol. **49**, 316 (2006).

High-energy proton acceleration using an innovative plasma-based fast (f/0.6) focusing optic

Contact *motoaki.nakatsutsumi@polytechnique.edu*

M. Nakatsutsumi, B. Albertazzi S. Buffechoux, and J. Fuchs
LULI, École Polytechnique, CNRS, CEA, UPMC, route de Saclay, 91128 Palaiseau, France

A. Kon, M. Tampo and R. Kodama
Graduate School of Engineering, Osaka University, Suita, Osaka 565-0871, Japan

N.P. Dover, C.A.J. Palmer, M.J.V. Streeter, S.R. Nagel, and Z. Najmudin
Blackett Laboratory, Imperial College London, London SW7 2BZ UK

J. Schreiber
Max Planck Institute Quantum Opt., D-85748 Garching, Germany

R. Marjoribanks
Department of Physics,University of Toronto, Toronto, Canada

R.J. Clarke, R. Heathcote, J.S. Green, M. M. Notley and D. Neely
Central Laser Facility, STFC, Rutherford Appleton Laboratory, HSIC, Didcot, Oxon, OX11 0QX, UK

Introduction

Achieving ever-higher irradiance for lasers holds great promise as it opens access to applications ranging from extreme nonlinear physics to the generation of bright sources of coherent radiation and particles for *e.g.*, ultrafast (~10^{-18} sec.) atomic-scale imaging, fast ignition of fusion targets, or hadron therapy. Present-day highest irradiances are obtained using the CPA technique [1] and further enhancement is planned through laser energy increase and pulse-duration reduction. An alternate route would be to decrease the focused spot size, but this is limited by the impracticality of extremely low f-number (high NA) focusing optics for conventional parabolic reflectors. Recently, we demonstrated an f/# = 0.4 optic that is a plasma-based, compact (~ 1 cm^3), ellipsoidal reflector [2]. It reduces the spot size 5-fold compared to standard focusing, leading to substantial enhancement to both the laser intensity and the maximum energy of the resultant proton beam. Furthermore, this 'switching' mirror can increase the laser pulse temporal contrast, a crucial factor in accessing promising new interaction regimes [3,11,12]. Our ambition of this experiment at the Vulcan PetaWatt facility was to apply this novel plasma optic to accelerate the laser-generated protons to a much higher energy than previously observed. High-intensity laser driven ion acceleration is an extremely active area of research. Applications such as proton imaging [3] have already been realised, and it is hoped that future applications will include medical isotope production [4], proton oncology [5], injection into large-ion accelerators, and fast-ignitor beam for laser-driven fusion[6]. Among the challenges remaining for proton sources in these potential applications is to increase the numbers and/or energies of the protons accelerated.

In this report, we describe 2 main results we observed during the campaign.

I. Tight focusing utilizing a re-focusing plasma mirror
II. Almost constant maximum energy of protons observed from 25 nm to 100 µm thickness foil

Experimental setup

The experiment was conducted on the Vulcan PetaWatt laser facility at the Rutherford Appleton Laboratory, operating in chirped pulse amplification (CPA) mode. A sketch of the setup is given in Fig. 1: approximately 200 J of 1 µm wavelength, linearly-polarized laser light contained in a ~1 ps pulse duration were focused using an f = 3 off-axis parabola mirror (OAP) down to a 7 ± 2 µm full width at half maximum spot measured with reduced energy laser (LA4), attaining an expected peak intensity of 9 x 10^{19} W cm^{-2} on target.

Tight focusing utilizing a re-focusing ellipsoidal plasma mirror (EPM)

To reduce this spot size and to achieve increased focused laser intensity and proton acceleration, we placed a small ellipsoidal plasma mirror (EPM) after the OAP, with one of the foci of the EPM coinciding with the OAP focus, to receive the laser beam and then to relay it to the second focus of the ellipsoid. As shown in Fig. 1, this geometry transforms the beam's solid-angle, producing an extremely small f-number (here, f/0.6). The magnification of the spot from the first focal point (OAP focus) to the second one was measured using

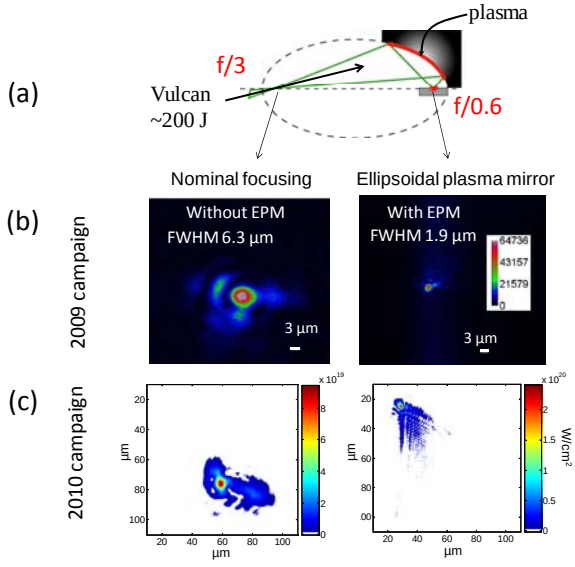

Figure 1 Experimental setup and measured focal spot with or without an ellipsoidal mirror. (a) Experimental setup for tight focusing of ultrahigh intensity Vulcan PW laser pulses by low f/# confocal ellipsoid plasma mirrors (EPM). Direct measurement of the focal spot using reduced energy LA4 alignment laser (thus without plasma on the EPM surface) shows that the focal spot size is reduced by a factor (b) ~3 in the 2009 campaign and (c) ~2 in the 2010 campaign.

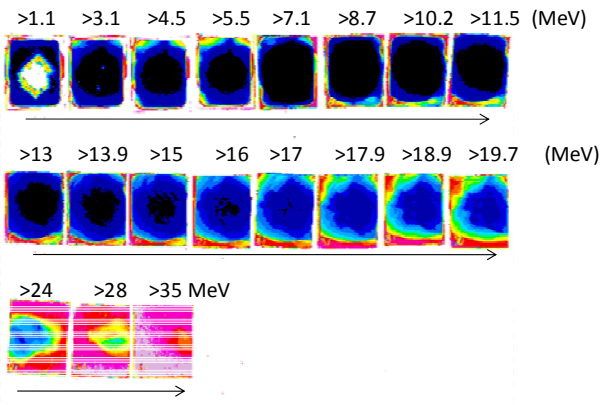

Figure 2 Angular distributions of protons measured by RCF films. 180 J, approximately 1 ps duration pulse is irradiated directly (no plasma mirror) on a 5.6 µm thick Al target. Up to 35-40 MeV protons are observed.

reduced laser energy (LA4), and gave a factor of ~0.3 of reduction in the 2009 campaign which was slightly reduced to a factor of ~0.5 in the 2010 campaign. Therefore the focal spot was reduced due to the EPM. This resulted in an enhancement of the focused laser intensity by a factor of ~2.5 compared to the case utilizing a flat plasma mirror as indicated in the fig. 1 (c). However, the factor is much less pronounced compared to a similar configuration measured at a different facility (100 TW laser facility, LULI, France) that gave a measured magnification of 0.2 []. Realignment of diagnostic optics (combination of a f/0.67 microscope objective with a f = 200 mm focusing lens) didn't improve the result. We note that the wavefront quality of alignment LA4 laser potentially affected the focus quality especially in such a tight f-number configuration.

Proton acceleration without Plasma Mirror

At first, we took a shot without any plasma mirrors (direct shot) that served as a reference shot. The laser of 415 J (43% of which only remained) after the OAP as measured with calorimetry) was irradiated on an Al target which was 5.6 µm thick and had transverse dimensions of 1 mm × 1 mm. For proton detection, we used stacked calibrated radiochromic films (RCF). The stack contained alternating layers of Gafchromic HD-810, MD-V2-55 and EBT2 type dosimetry film and indium or aluminum filters of varying thickness. The stack was placed ~27 mm behind the target foil in the normal direction. The RCFs measured the spatial distribution of the proton beam at discrete energies corresponding to the proton deposited energy in the form of Bragg peaks. Figure 2 shows a proton pattern that demonstrates up to 37 ± 2 MeV protons. The beam divergence half angle was 45° at 27 MeV and 15° at 37 MeV.

Proton acceleration with an ellipsoidal plasma mirror (EPM)

In order to enhance the focused intensity *and* suppress the intensity of amplified spontaneous emission and prepulses, we employed an ellipsoidal plasma mirror (EPM). The distance on the optical axis between the focal point of the OAP to the ellipsoidal surface was 20 mm. The reflectivity of the plasma mirror was measured to be ~70%. The maximum energy we observed utilizing the same target as a reference (direct) shot was 15 ± 2 MeV. Contrary to the prediction, it was much lower energy than the reference shot without any plasma mirror. To understand the reason of reduced efficiency of proton acceleration and to try to improve it, we performed several trials.

(1) Placed the target out of focus

(2) Changed the target thickness

(3) Used a gold-coated high-reflectivity EPM to change the temporal contrast of the laser

The results of these results are summarized in fig. 4.

Trial (1) Place the target out of focus

The purpose of the defocusing shot (trial (1)) was to check the longitudinal shift of the focal spot of the high-power laser compared to the LA4 alignment laser. There could be some variation due to the thermal lens effect in the laser chain, which could potentially modify the divergence of the laser. To evaluate the effect on the final focal spot after the EPM, we have performed a ray-trace calculation. The result is shown in Fig. 3. When the actual focal spot position of the OAP is shifted away from the OAP by 100 µm for the high-power shot, the spot size at the secondary focal point of the EPM becomes 6.3 µm. In this case, the effective best focus after the EPM comes 4 µm away from the ellipsoid focus. The spot size at this point is 0.7 µm, i.e., very good. Note that due to geometrical optics calculation, the focal spot size in the calculation could be smaller than the wavelength. Figure 3 (d) summarizes the focal spot diameter at the location of the EPM secondary focus when the incoming laser is focused away from the EPM primary focus (closed square). Also shown is the minimum focal spot size achievable when the misalignment is compensated by placing the target away from the EPM focus (open triangle). The open circles indicate the position of this effective best focus. The figure indicates that even if the OAP focus point is shifted longitudinally by 200 µm during the high-power shot, a focal spot size down to 1.5 µm would be achievable utilizing the EPM if the target was set 8 µm after the nominal EPM focus.

During the experiment, we performed 2 defocus shots; we put the target 25 µm and 100 µm after the nominal focus point of the ellipsoid, which correspond to 600 µm and 2.5 mm longitudinal shifts of the OAP focus. The value seems

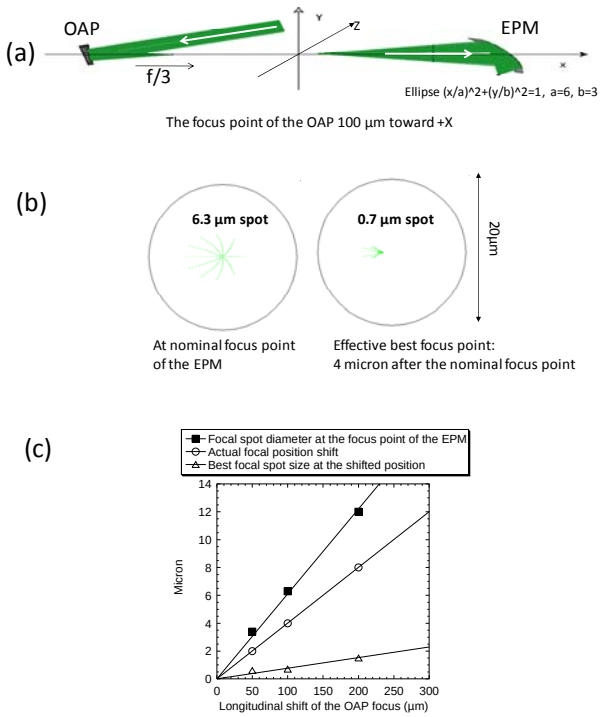

Figure 3 Evaluation of the influence on the final focal spot size when the OAP focus point is shifted longitudinally during a high-power shot. (a) Setup (b) left : Focal spot pattern at the secondary focus after the EPM when OAP focus point is longitudinally shifted by 100 µm. right : focal spot pattern at 4 µm after the EPM focus. (c) Summary of the calculation.

large compared to the calculation, but the observed results showed practically the same proton maximum energy for these defocus shots. We observed ~15 MeV for 25 μm out of focus and ~12 MeV for 100 μm out of focus. The result indicates the potential issue of the longitudinal shift of the OAP during high-power shot was masked by other problems.

Trial (2) Changing the target thickness

Reducing the target thickness helps to enhance the proton accelerating sheath field due to reduced spreading of the fast electrons which are responsible for creating the electrostatic sheath field which accelerate the protons. The minimum possible target thickness is limited by the temporal contrast of the interaction laser because the pedestal preceding the main laser pulse preheats the target plasma which inhibits the sheath field. We systematically changed the target thickness to scan the optimum condition for the proton acceleration. The target material was chosen to be aluminum, gold or diamond-like-carbon (DLC), as indicated by the fig. 4. Surprisingly, we observed practically no improvement or degradation of the proton maximum energy by changing the target thickness by 4 orders of magnitude. When we reduced the target thickness, down to 25 nm, the proton maximum energy remained ~15 MeV. We finally observed a slight improvement of energy up to ~25 MeV when shooting a 5 nm thick DLC foil. When increasing the thickness, the proton maximum energy stayed again ~15 MeV up to 100 μm thick target, then slightly decreased for a 500 μm thick target shot. The reason of this surprising result remains unclear. It is obvious that using the EPM, and hence improving the laser contrast helped for keeping good interaction conditions for the 5 nm foil. Indeed, when we shot a 5 nm thick foil without using the EPM (direct shot), we observed a significant reduction of the proton maximum energy (3 ± 1 MeV). This means that the pedestal preheated the foil and caused significant plasma expansion before the main pulse arrived.

When we increase the target thickness, we observed a clear reduction of proton divergence angle, which indicates a flat sheath field at the rear surface.

Trial (3) Using a gold-coated high-reflectivity EPM to change the temporal contrast of the laser

Despite changing the target thickness and placing the target out of focus, no improvement of proton energy was achieved, *i.e.*, we couldn't observe higher proton energy than the direct shot. It is known that in the very high temporal contrast regime, where the main laser pulse interacts with very steep density gradient plasmas, the effective electron temperature becomes lower than the value predicted by the ponderomotive scaling [7]. This is because in an overdense plasma the collisionless skin depth is less than the laser wavelength. At $I_L >> 10^{18}$ W cm^{-2} (relativistic), electrons traveling near the speed of light traverse a distance greater than the skin depth before acquiring the full ponderomotive potential [8]. To address this effect, we applied an Au coating to our EPM surface to enhance the reflectivity of the pedestal part of the pulse, which should provide a similar laser temporal contrast as the direct shots. However, contrary to our prediction, proton maximum energy was reduced to 12 ± 1 MeV when utilizing the highly reflective EPM. The target thickness was 5.6 μm for this shot.

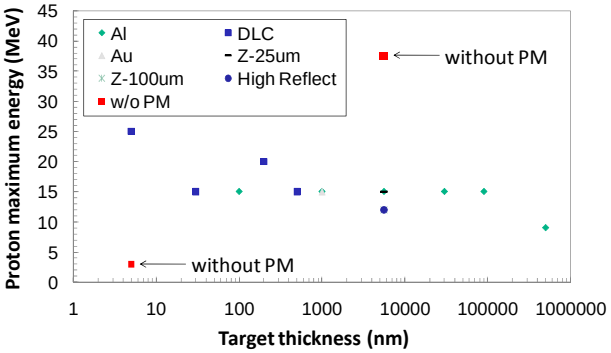

Figure 4 Summary of the experimental result. Experimentally observed proton maximum energy vs. target thickness when utilizing the EPM. Red squares indicate direct shot (without plasma mirror).

Conclusions

We performed an experiment utilizing a re-focusing ellipsoidally shaped plasma mirror (EPM) to increase the focused laser intensity of the Vulcan PetaWatt laser and thus facilitate proton acceleration to high energies. Despite the reduction of the focal spot size, we observed practically no improvement in proton energy when the EPM was employed. Changing the target thickness, defocusing or increasing the pedestal level did not improve the result. The most interesting result we observed was a constant proton maximum energy (~15 MeV) between 25 nm up 100 μm target thickness (4 orders of magnitude difference). The reason of this result has not yet been clarified. Reduction of the proton maximum energy compared to a direct shot (without a plasma mirror) was observed also when utilizing a plane plasma mirror (see the report by N. P. Dover *et. al.*). One potential reason for that might be due to the spatial intensity fluctuation of the near-field pattern of the laser, which could interfere with the ionization dynamics of the plasma mirror. Such an effect needs to be investigated in future campaigns.

Acknowledgements

The authors acknowledge the assistance of the Central Laser Facility staff at the Rutherford Appleton Laboratory in carrying out this work. This work was supported by CREST Japan Science and Technology and by the Laser Induced Beams of Radiation and their Applications (LIBRA) programme, which is funded by the EPSRC.

1 D. Strickland and G. Mourou, Opt. Commun, **56**, 219 (1985).
2 M. Nakatsutsumi *et al.*, Opt. Lett. **35,** 2314 (2010).
3 L. Romagnani *et al.*,, Phys. Rev. Lett. **95** 195001 (2005).
4 I. Spencer et al. Nucl. Instrum. Methods Phys. Res. B **183**, 449 (2001).
5 S. V. Bulanov *et al.*, Phys. Lett. A **299**, 240 (2002).
6 M. Roth *et al.*, Phys. Rev. Lett. **86**,436 (2001).
7 S. C. Wilks et al., Phys. Rev. Lett. 69, 1383 (1992).
8 M.G. Hains et al., Phys. Rev. Lett. **102**, 045008 (2009).

Measurements of Rayleigh-Taylor instability growth in a layered target heated by a high power short pulse laser

Contact *john.pasley@york.ac.uk*

A. K. Rossall, I. A. Bush, C.P. Edwards, G. J. Tallents, N. C. Woolsey, and J. Pasley
Department of Physics, University of York, Heslington, York, YO10 5DD, UK

K. Lancaster, T. Winstone, C. Spindloe, and H. Lowe
Central Laser Facility, STFC, Rutherford Appleton Laboratory, HSIC, Didcot, Oxon, OX11 0QX, UK

W. Nazarov
School of Chemistry, University of St Andrews St Andrews, KY16 9ST, UK

P. Morantz
Materials Department, Cranfield University Cranfield, Bedfordshire, MK43 0AL, UK

Introduction

The Rayleigh-Taylor (RT) instability occurs when a lighter fluid accelerates a heavier fluid, causing instability between two layers. The instability begins as slight irregularities between otherwise planar layers which increase in time, creating 'finger-like' ridges of dense material moving around bubbles of the less dense fluid [1]. The Rayleigh-Taylor instability in plasmas is observed in inertial confinement fusion [2], and in astrophysics such as within the outer portion of a collapsed, massive star [1]. The Rayleigh-Taylor instability in short pulse laser-produced plasmas has recently had to be taken into account in order to explain the expansion behavior of two layer targets of 25 and 50μm thickness [3]. In the experiment of Lancaster et al. [3], a target consisting of adjacent Cu and CH layers was found to be RT unstable as the copper layer cooled quickly via radiative emission and was then 'pushed' by the higher temperature, lower density plastic, leading to instability. For a laser-produced plasma experiment, this situation is unusual since the RT instability is not ablatively stabilized. This makes the situation more representative of many astrophysical situations, and also more akin to the stagnation phase of the instability seen in ICF capsule than the more commonly studied effect which occurs at the capsule surface.

The Rayleigh-Taylor Instability

The aim of this experiment is to further investigate the RT instability in a configuration similar to that used by Lancaster et al [3], by imaging titanium K_α emission through a RT unstable target. As in the Lancaster et al. experiment, plastic and copper layered targets were used to create the Rayleigh Taylor unstable plasma. In this experiment, however, the instability is seeded by introducing an approximately sinusoidal perturbation at the interface between the copper and the plastic. In order to achieve approximately uniform heating a more compact target of dimensions 200μm × 200μm x 27μm is used to encourage hot electron refluxing [4-7].

The RT instability will cause a sinusoidal interface, with wave number *k*, will grow such that its amplitude at a given time, *t*, will be proportional to $\exp(\gamma t)$ [8]. The growth rate, γ, is a function of the acceleration, *g.*, and the material properties of the target.

Experimental Set-up

The K_α back-lighter was created using a pulse from the VULCAN Nd:Glass laser system at the Rutherford Appleton Laboratory's Central Laser Facility to irradiate a titanium target of thickness 25μm. A chirped pulse amplified (CPA) pulse of duration 2ps and energy of 100J was focused to a spot ~ 200μm in diameter, using an f/3 parabolic mirror, giving an irradiance of ~ 2×10^{17} W cm^{-2}. A second CPA pulse of 3ps duration with energy of 300J was focused into a spot ~ 10μm in diameter (~ 1×10^{20} W cm^{-2}) onto the RT unstable target described in the following section. The delay between the heating pulse and the back-lighting pulse was varied between 50 and 150ps to study the evolution of the RT instability. A HOPG (highly ordered pyrolytic graphite) spectrometer was used to record the time averaged copper K_α (8.05 keV) spectrum to investigate the plasma conditions within the copper layer. A spherically bent SiO_2 quartz (2023) crystal with a radius of curvature of 38cm was used to image titanium K_α (4.51 keV) radiation generated from the back-lighter foil after passing through the RT unstable target onto an image plate. A schematic for the experimental layout showing the relative positions of the targets, the 2D crystal imager and the HOPG spectrometer is shown in figure 1.

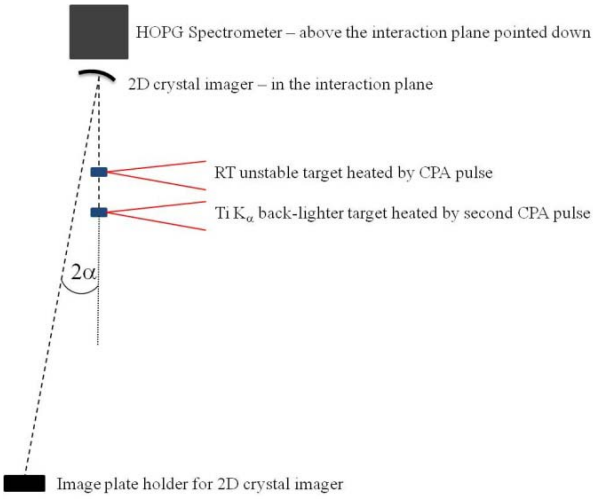

Figure 1. Experimental schematic showing the relative positions of the diagnostics where $\alpha = 90 - \theta_B$ and θ_B is the Bragg angle for Ti K_α.

Target Design

The RT unstable targets comprised 25μm thick plastic covered with a 2μm thick copper layer with a sinusoidal oscillation of thickness with amplitude 300nm and wavelength 30μm at the interface between the two layers (see figure 2). The oscillation between the layers varies the copper thickness by 600nm from peak to trough, thus varying the transmission of K_α photons through the target as shown in figure 2. The sinusoidal oscillation between the two layers seeds the Rayleigh-Taylor instability which grows on a timescale longer than the heating pulse when irradiated as illustrated in figure 2. It is expected that hot electron refluxing will reduce temperature gradients in the target substantially. As the instability grows the change in transmission across the target increases and by varying the time delay between the heating pulse and the pulse used to generate the Ti K_α back-lighter, the evolution of the instability can be

investigated. The expected variation in transmission across a cold target is shown in figure 3.

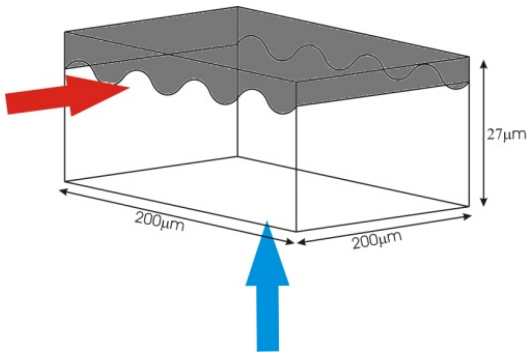

Figure 2. Rayleigh-Taylor unstable target design. Copper (dark region) of thickness ~ 2μm is coated onto plastic (light region) of thickness ~ 25μm with a sinusoidally oscillating interface of amplitude 300nm and wavelength of 30μm. Red arrow indicates direction of heating laser and blue arrow indicates direction of Ti K_α back-lighter.

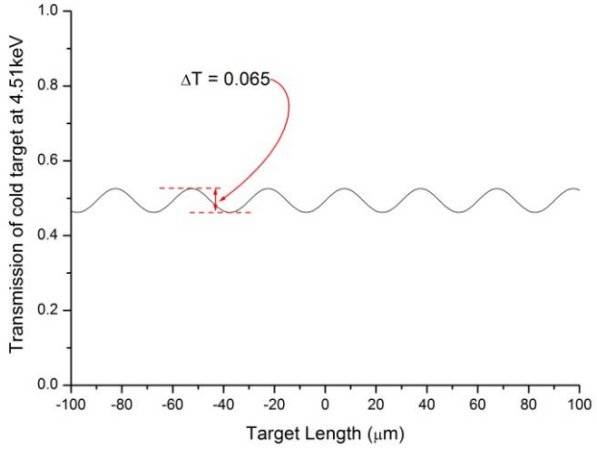

Figure 3. Variation in transmission across a cold RT target and the corresponding change in transmission across the target as the back-lighter passes through the varying thickness of copper. The theoretical change in transmission, ΔT, is calculated to be ΔT = 0.065 for a cold target.

The targets are prepared as 200 × 200 μm squares supported on a 50 μm wire. The sinusoidal oscillations run horizontally, parallel to the heating CPA pulse which is incident onto the front surface as shown in figure 2. In the vicinity of the interface, and toward the centre of the target, the laser pulse heats the two materials simultaneously to a similar temperature by hot electron propagation and refluxing. The denser copper cools more rapidly than the plastic due to stronger radiative cooling. The lighter and hotter plastic can then accelerate the denser, cooler copper, since it retains a higher pressure. Seeded by the initial perturbations, the RT instability will then rapidly grow. As the instability evolves, and the 'finger-like' columns emerge, the copper thickness can be expected to increase and decrease in different areas of the target, changing the transmission and thus the amplitude of the modulation in optical depth as penetrated by the back-lighter. By imaging the back-lighter at the RT target position at different times, the evolution of the instability can be investigated.

HOPG Spectrometer

The HOPG spectrometer was used to investigate the K_α and He-like spectrum of the copper. Figure 4 shows the spectrum containing the Cu K_α line (8.05 keV), He-like intercombination (x, y - 8.35 keV) and resonance (w - 8.39 keV) lines and Li-like satellites (e, f, u) around 8.30 keV. The standard letter designation is as defined by Gabriel [9].

The particle-in-cell (PIC) code LPIC++ [10] was used to simulate the laser interaction with a copper target. A hot electron temperature of T_h = 65 keV and a hot electron fraction of f_h = 0.28 are calculated. The spectral modelling code FLYCHK [11], was then used to simulate the He-like lines generated in the copper plasma. Using the values of T_h = 65 keV and f_h = 0.28 and varying the thermal temperature, T_c, and the electron density, n_e, the dependence of the line ratios upon these parameters is determined. The FLYCHK simulations indicate a temperature of between T_c = 300 - 400 eV and a density of $n_e = 10^{22} - 10^{23}$ cm^{-3}. As the recorded spectra are time averaged, the instantaneous peak in emission will be from a higher density.

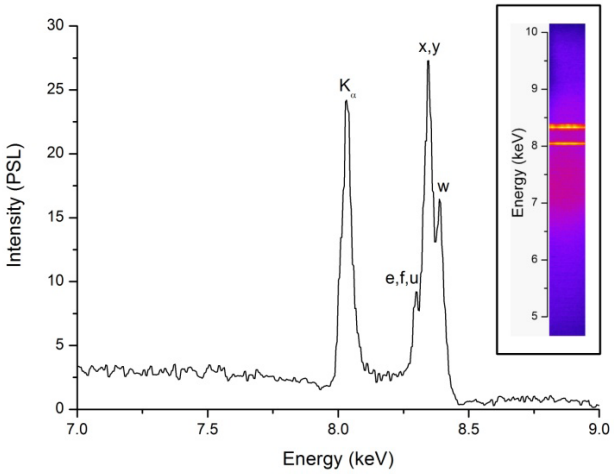

Figure 4. Calibrated spectrum obtained from HOPG crystal spectrometer showing the Cu K_α line, He-like resonance line (w), He-like intercombination line (x,y) and Li-like dielectronic recombination satellites (e,f,u). Letter designation is as defined by Gabriel [9]. Insert is an image of the raw HOPG spectrum.

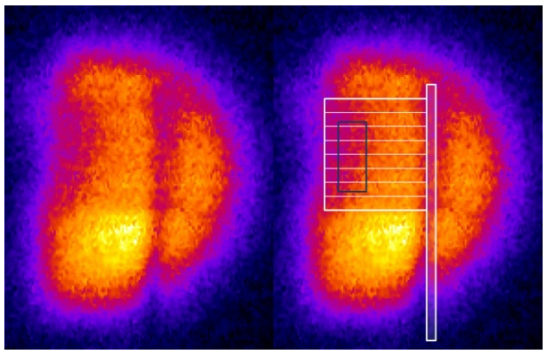

Figure 5. Sample images from 2D spherical crystal imager, left shows Ti K_α back-lighter passing through the RT unstable target, right shows the same image with a schematic of the target overlaid indicating the perturbation orientation. The delay between the heating pulse and the pulse to generate the Ti K_α back-lighter is 150ps and the heating laser is incident on the left hand side of the target. The blue box demonstrates the integration area (integration is parallel to the oscillation) for FFT analysis.

2D K_α Imager

A sample image of the Ti K_α back-lighter passing through the RT unstable target is shown in figure 5. The back-lighter signal over a section of the images was integrated along the direction of the grooves (see figure 5) so as to enhance the contrast of any perturbations present. The section of image selected for the integration is behind the laser interaction region, the size of which is shown in figure 5. A 1D fast Fourier transform (FFT) is then performed on the resulting line out, taken perpendicular

to the groove direction, in order to analyze any spatial frequencies present.

The portion of the back-lighter in each image which does not pass through the RT target is used to calculate a mean PSL (photostimulated luminescence) value for the initial back-lighter intensity which is then used to normalize the images with the original back-lighter intensity, $I_0 = 1$. The amplitude of the Fourier transform then represents the amplitude of the oscillation in terms of change in transmission, where $\Delta T = 2 \times$ FFT amplitude and ΔT is defined in figure 3.

As the sinusoidal oscillation within the target is restricted to a finite space (i.e. over the target length) the function must be thought of as a top hat function multiplied by a sine function. The resulting FFT shown in figure 6 is a sinc function originating from the top hat component convolved with a pair of antisymmetrical delta functions corresponding to the frequency and amplitude of the sinusoidal oscillation.

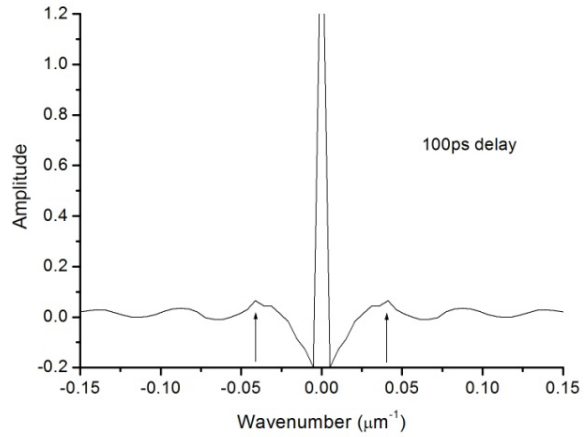

Figure 6. FFT of the Ti K_α image at a time delay of 100ps between the RT heating beam and the Ti K_α back-lighter beam. Arrows indicate the position of the peaks corresponding to the target oscillation.

For comparison purposes, the Ti K_α back-lighter was used to back-light a cold RT unstable target and the results are found to agree with the theoretical predictions for a cold target. The cold perturbation wavelength was calculated to be $\lambda = (24.5 \pm 6.1)$ μm and the change in transmission was $\Delta T = (0.062 \pm 0.007)$ in agreement with the information supplied by the target manufacturer ($\lambda = 30$μm with $\Delta T = 0.065$ arising from the thickness modulation).

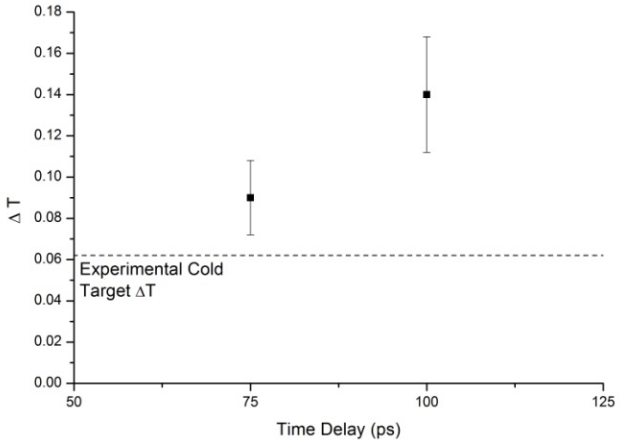

Figure 7. The ΔT values shown here are twice the amplitude from the FFTs and represent the total change in transmission from peak to trough of the target perturbation. The dashed line represents the experimentally measured value of ΔT for the cold RT target.

The transmission data indicates that exponential Rayleigh-Taylor growth occurs within the first 100ps of the interaction; an increase in ΔT means an increase in the oscillation between the two different layers. The measured increase in ΔT corresponds to an increase in copper thickness of 350 ± 100 nm. This results in an instability amplitude of 650 ± 100 nm after 100ps and gives a Rayleigh-Taylor growth rate (see equation 1) of $\gamma = 10 \pm 2$ ns^{-1}. This growth rate is approximately an order of magnitude higher than observed previously [12-14] at the lower absorbed irradiance of ~ 10^{13} W cm^{-2}. Figure 7 demonstrates the growth of ΔT as a function of time delay between the two beams.

Conclusions

A laser plasma of parameters; $T_c = 300$ - 400eV, T_h = 65keV and $f_h = 0.28$ is produced by heating a Rayleigh-Taylor unstable target using the Vulcan laser system with an irradiance of 1×10^{20} W cm^{-2}. A target, seeded with an initial perturbation of amplitude 300nm between layers of copper and plastic, demonstrated Rayleigh-Taylor instability in the first 100ps after the laser interaction with a growth rate of $\gamma = 10 \pm 2$ ns^{-1}.

Acknowledgements

The authors wish to thank the staff at the Central Laser Facility for their assistance during the experiment.

References

[1] D Sharp, Physica D: Nonlinear Phenomena **12**, 3-18 (1984).

[2] B.A. Hammel, S.W. Haan, D.S. Clark, M.J. Edwards, S.H. Langer, M.M. Marinak, M.V. Patel, J.D. Salmonson, and H.A. Scott, High Energy Density Physics **6**, 171-178 (2010).

[3] K. L. Lancaster, J. Pasley, J. S. Green, D. Batani, S. Baton, R. G. Evans, L. Gizzi, R. Heathcote, C. Hernandez Gomez, M. Koenig, P. Koester, A. Morace, I. Musgrave, P. A. Norreys, F. Perez, J. N. Waugh, and N. C. Woolsey, Physics Of Plasmas **16**, 056707 (2009).

[4] M N Quinn, X H Yuan, X X Lin, D C Carroll, O Tresca, R J Gray, M Coury, C Li, Y T Li, C M Brenner, A P L Robinson, D Neely, B Zielbauer, B Aurand, J Fils, T Kuehl, and P McKenna, Plasma Physics and Controlled Fusion **53**, 025007 (2011).

[5] P. M. Nilson, W. Theobald, J. Myatt, C. Stoeckl, M. Storm, O. V. Gotchev, J. D. Zuegel, R. Betti, D. D. Meyerhofer, and T. C. Sangster, Physics Of Plasmas **15**, 056308 (2008).

[6] J. Myatt, W. Theobald, J. A. Delettrez, C. Stoeckl, M. Storm, T. C. Sangster, A. V. Maximov, and R. W. Short, Physics Of Plasmas **14**, 056301 (2007).

[7] S. Baton, M. Koenig, P. Guillou, B. Loupias, A. Benuzzimounaix, J. Fuchs, C. Rousseaux, L. Gremillet, D. Batani, and A. Morace, High Energy Density Physics **3**, 358-364 (2007).

[8] K. Rifai, F. Vidal, and T. W. Johnston, Physics Of Plasmas **14**, 082311 (2007).

[9] A. H. Gabriel, Mon. Not. Astron. Soc. **160**, 99 (1972).

[10] R. E. W. Pfund, R. Lichters, and J. Meyer-ter-Vehn, AIP Conference Proceedings **426**, 141-146 (1998).

[11] H. Chung, M. Chen, W. Morgan, Y. Ralchenko, and R. Lee, High Energy Density Physics **1**, 3-12 (2005).

[12] M. Emery, J. Gardner, and S. Bodner, Physical Review Letters **62**, 694-694 (1989).

[13] M. Emery, J. Gardner, and S. Bodner, Physical Review Letters **57**, 703-706 (1986).

[14] R. Whitlock, M. Emery, J. Stamper, E. McLean, S. Obenschain, and M. Peckerar, Physical Review Letters **52**, 819-822 (1984).

Proton beam steering from ultra-thin foils irradiated by intense laser pulses

Contact *rprasad01@qub.ac.uk*

R. Prasad, H. Ahmed, D. Doria, K. Kakolee, S. Kar, M. Zepf, M. Borghesi

Centre for Plasma Physics, Queen's University of Belfast, Northern Ireland, UK, BT71NN

D. C. Carroll, D. Maclellan, P. McKenna

SUPA, Department of Physics, University of Strathclyde, Glasgow, UK

N. P. Dover, S. Nagel, C.A.J. Palmer, M.J.V. Streeter, Z. Najmudin

The Blackett Laboratory, Imperial College, London, UK

C. M. Brenner, G. Scott, M. Galimberti, J. S. Green, R. Heathcote, M. Notley, D. Neely

CLF, Rutherford Appleton Laboratory, STFC, Oxfordshire, UK

Introduction

Laser interaction with thin solid foils at the intensities currently available (> 10^{20} W/cm^2) has opened up several novel and exciting avenues of research, including the development of compact ion accelerators with potential, high impact applications in medicine, science and industry [1-5]. Since intense laser driven multi-MeV proton beams were discovered, nearly a decade ago [6, 7], substantial experimental and theoretical effort has been aimed to the understanding of the underlying acceleration mechanism, as well as to improving beam characteristics in order to meet the conditions required for the envisioned applications. Although the broad energy spectrum and divergence of such beam has been beneficial for proton probing applications [8, 9], they pose significant concern for other applications demanding high flux at a reasonable distance from the target. Control of beam properties, such as energy spectrum, directionality and divergence are highly topical areas of current research. Several techniques have been investigated so far in order to control the beam characteristics, for instance, simultaneous energy selection and beam focusing by electrostatic micro-lenses [10] and ballistic focusing of poly-energetic protons by employing curved targets [11].

The main acceleration mechanism responsible so far for accelerating the multi-MeV protons/ions is the so called Target Normal Sheath Acceleration (TNSA). In this process, hot electrons generated at the target front surface due to the interaction of the intense laser pulse, propagate through the target and create a sheath field at its rear side. The strength of the sheath field is typically of the order of TV/m, and lighter ions (for example the protons, created by ionisation of hydrogen atoms present in the target contaminant layers) are preferentially accelerated to MeV energies in this sheath field. During this process, the ions are generally accelerated along target normal. However in a number of recent observations it has been found that the high energy proton beam steered away from the target normal under certain conditions. Modifying the level of ASE and its duration, the direction of beam emission for oblique laser incidence could be varied (or even controlled) from thin solid foils of a few micron thickness [12, 13]. These observations were discussed still in terms of TNSA, but in combination with a laser-controllable shock wave locally deforming the target rear surface.

In this report we present recent results also featuring a deviation of the proton beam emission direction from the target normal. This was observed during an experiment in which the VULCAN PW was focused onto sub-micron Cu foils over a range of laser incidence angles on target and for various target thicknesses. Even for normal incidence a substantial deviation (~15°) from the target normal was observed, and the dependence of deflection angle on incidence angle follows an unexpected pattern, different than observed in the experiments mentioned above. These measurements were taken with a high contrast laser pulse, by using a plasma mirror [14] before the target. On the other hand, either at lower contrast (without the plasma mirror) with thin targets (<500nm), or, high contrast and thick targets (>2μm), this steering effect was not observed. Detailed analysis of the data is currently under progress. However, preliminary discussion is made based on the possible role of non-uniform near field profile of the laser (as measured during the experiment and due to damages in the optics in the compressor and target chambers) on the plasma mirror performance, modifying the temporal profile of the laser incident on the target.

Experimental set up

The experiment was carried out on the Vulcan laser facility at the Rutherford Appleton Laboratory, which delivered ~400J energy in 750fs. A plasma mirror was used to enhance the contrast (ratio between intensities of main CPA pulse to ASE/prepulses) of the laser to ~10^9. The measured reflectivity of the plasma mirror was ~70% for p-polarization. An f/3 off axis parabola was used to focus the beam down to a ~8μm FWHM spot size, with peak intensity >10^{20} W/cm^2. Radiochromic films (RCF) were used to monitor the beam profile. The RCF stack was divided in two parts (6cm x 2cm each) with a gap of 3mm between them, in order to allow the central section of the beam to be diagnosed by Thompson parabola spectrometers. The stacks were placed normal to the laser axis at a distance of 6cm from the target plane. A schematic of the experimental set up is shown in fig.1.

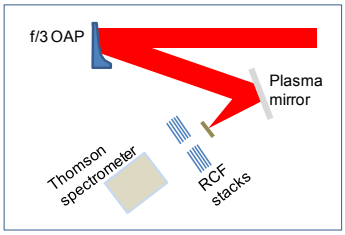

Fig.1 Schematic of the experimental set up.

Results and discussion

The dependence of the proton beam steering effect from the laser incidence angle on the target is illustrated in fig.2, by simple schematics followed by experimental data and graphs. 100nm Cu foil targets were irradiated by linearly polarised laser pulses with high contrast, enhanced by a plasma mirror. In the schematics shown in figs (a)-(c), the emergence direction of the proton beam with respect to the target normal is sketched for three different laser incidence angles. One can see that at 0° incidence angle the beam is steered about 15° (see fig a). The proton beam is steered by ~ -15° (where '-' sign corresponds to anti-clockwise rotation from the top) for a laser incidence angle of -15° (see fig b). However, interestingly when the laser incidence angle was 15°, the beam was steered by 30° (see fig c). In the schematics, the RCF stacks were mounted normal to the laser axis direction. The raw RCF images obtained from these shots, illustrating the beam steering, are shown below the schematic of each case. The deviation angle of the high energy component of the proton beam (>4MeV) with

respect to target normal direction is plotted as a function of laser incident angle on the target in fig 2(g). We see that by varying the incidence angle from 0° to 15°, the beam was steered to ~ 30° from target normal while at -15° incidence the beam steered to the other side of the target normal, as described above. We have also plotted (in fig.2 (h)) the deviation angle measured with respect to laser axis direction as a function of laser incidence angle on the target. In this case, one can see that by changing the incidence angle from 15° to -15° the beam steered from 15° to 0°, i.e. along the laser axis.

In an attempt to clarify the underlying mechanism for the beam steering, we tried shots by changing different parameters. For instance, the red squares shown in the fig (g) and (h) are the measurements taken with circularly polarised laser on target at 0° incidence, keeping all other laser and target parameters unchanged. As clear from the graphs, the beam steering appeared to be independent of incident laser polarisations.

Similarly, in order to clarify the role of prepulses behind the beam steering, as exploited by Lindau et.al, [12] for beam manipulation, we made the same measurement with a high reflective front coated plasma mirror (PM). In this case, the low intensity prepulses /ASE of Vulcan laser are fully reflected to the target due to the high reflective coating of the PM. As the intensity reaches plasma formation threshold, the PM starts reflecting the main laser pulse in the same way as an anti-reflective coated PM, used in the cases described above. Blue squares in the fig (g) and (h) show the measurements taken with the high reflective PM. As one can see, the measurements are identical for the two different types of PM coating, which suggests that the observed steering effect is unlikely to be due to shock formation by the the ASE of the laser.

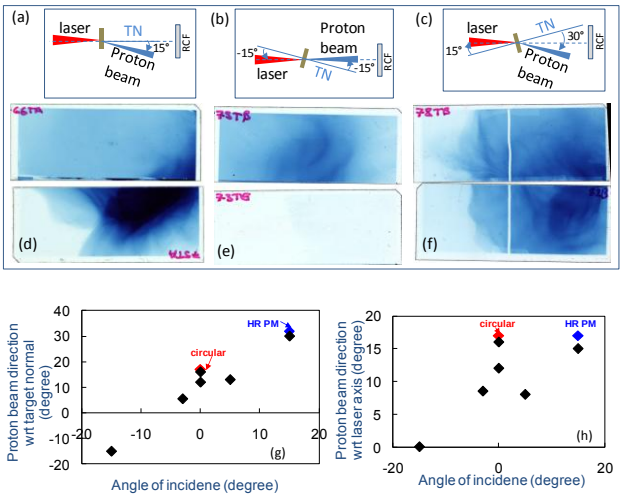

Fig.2 (a)-(c) show schematics of the observation for three different angles of laser incidence on target, with indication of the proton beam deviation measured with respect to the target normal (TN) direction. In figs (d)-(f) the beam imprints on RCF corresponding to figs (a)-(c) are shown. The gap between the top and bottom parts of the RCF layers allows to employ Thomson spectrometers for spectral measurements and the stacks were mounted normal to the laser axis. The vertical line in fig (f) is the shadow of a fiducial wire attached to the RCF stack in order to define the laser axis. In (g) the proton beam deviation with respect to TN is plotted as a function of laser incidence angle. Fig (h) shows deviation with respect to the laser axis as a function of laser incidence angle.

The deviation of the proton beam from the target normal was also investigated by varying the target thickness at high contrast. In fig.3 the dependence of the deviation angle on target thickness is shown. In this case the laser incidence angle was 0°. We see that the deviation increases sharply for target thickness <500 nm.

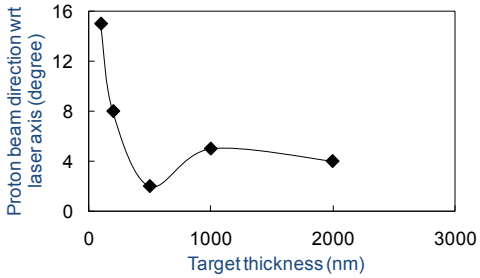

Fig.3 Deviation of proton beam measured with respect to target normal as a function of target thickness. Laser incidence angle was 0° for all thicknesses.

Finally, the same shots were taken by removing the plasma mirror and irradiating directly the target. Intriguingly, in these shots the proton beam emerged along the target normal direction for all thicknesses and incidence angles investigated (while in principle ASE-induced shock deformation should become stronger in this case).

Summarizing the above discussion, the steering effect was observed only for very thin targets when a plasma mirror was in operation. Measurements of the near field profile of the laser before the plasma mirror revealed that it was strongly non-homogeneous. Due to severe damages in the optics inside the compressor and target chambers, half of the beam had double the intensity of the other half (see schematic in fig.4). In principle, this can modify the laser pulse temporal profile because of different switch-on times of the PM on the two halves of the beam. Although the dynamics of the interaction under these non ideal conditions are far from clear, this effect can modify the hot electron population and its propagation through the target, and subsequently the sheath field profile at the rear of the target. Detailed analysis of the data is currently under progress.

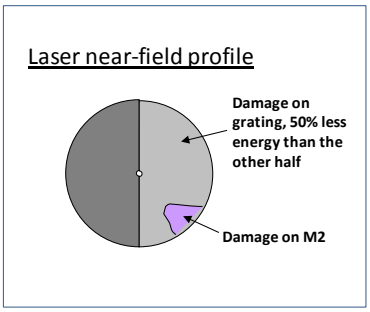

Fig.4 Illustration of near field profile of the laser pulse in our campaign, as the beam enters the target chamber.

Summary

In summary we have reported on observations of proton beam steering from the target normal direction using high contrast laser pulses from the VULCAN PW laser. With 100nm Cu targets beam deviations from target normal of up to 30º were observed, which showed a correlation with the laser incidence angle. The steering effect was not observed without PM, and became progressively weaker for thicker targets. The phenomenology of the results does not fit easily with explanations provided for previous, similar observations [12-13], based on shock perturbation of the target rear surface. It appears likely that the results are related to non-ideal PM operation due to a strongly uneven near field profile. Further analysis and modelling is required in order to clarify how this affects the ion acceleration dynamics.

Acknowledgement

This work was supported by EPSRC grants EP/E035728/1 (LIBRA Consortium) and EP/F021968/1. We acknowledge the support of the CLF staff at RAL.

References

1. M. Borghesi et al., Fusion Sci Technology **49**, 412 (2006)
2. J. Fuchs et al., Nature Phys. **2**, 48 (2006)
3. S. Bulanov *et al.*, Phys. Lett. A, **299**, 240 (2002)
4. T. Cowan *et al.*, Phys. Rev. Lett. **92** 055003 (2004)
5. M. Temporal et.al., Phys. Plasmas **9**, 3098 (2002)
6. R. Snavely *et al.*, Phys. Rev Lett., **85** 2945 (2000)
7. E.L Clark et. al., Phys. Rev Lett., **84**, 670 (2000)
8. M. Borghesi *et al.*, Phys. Plasmas **9**, 2214 (2002)
9. L. Romagnani et. al., Phys. Rev Lett., **95**, 195001 (2005)
10. T Toncian et. al., Science **312**, 410 (2006)
11. S. Kar et. al., Phys. Rev. Lett. **106**, 225003 (2011)
12. F. Lindau et. al., Phys. Rev. Lett. **95**, 175002 (2005)
13. K Zeil et. al., New Journal Phys. **12**, 045015 (2010)
14. B. Dromey et. al., Rev. Sci. Instrm, **75**, 645 (2004)

Formation of channels in underdense plasma with a 30 ps laser pulse

a.rehman07@imperial.ac.uk

A. Rehman, Z. Najmudin, A.E. Dangor
Blackett Laboratory, Imperial College London, SW7 2BZ

K.L. Lancaster, R.H.H. Scott, P.A. Norreys
STFC Rutherford Appleton Laboratory, Chilton, OX11 0QX

G. Sarri, M. Borghesi
School of Mathematics and Physics, Queens University Belfast, BT7 1NN

H.Chen
Lawrence Livermore National Laboratory, Livemore, California 94551, USA

J. R. Davies, J. Jiang, N. Lopes, C. Russo
GoLP, Instituto de Plasmas e Fusão Nuclear – Laboratório Associado, Instituto Superior Técnico, Lisbon, Portugal

K.A. Tanaka, N.Kageiwa, Tsuyoshi Tanimoto

Graduate School of Engineering, Osaka 565-0871, Japan

M. Tatarakis, S. Hassan, E.L. Clark
Technological Educational Institute of Crete, Chania GR 710 04 Greece

Abstract

We report experimental observations of plasma channels created by focusing a 30 ps pulse with a peak intensity of 3×10^{18} Wcm^{-2} into a deuterium gas jet. The size of the plasma channel was measured to be ~ 2 mm in length and the diameter of the plasma channel was ~300 μm for higher densities.

Introduction

The propagation of an intense laser pulse through fully ionised plasma has been investigated extensively in the last decade (1). There are a number of applications that require the formation of a stable channel in underdense plasma. These include high-quality laser wakefield acceleration of electrons (2), high brightness x-ray generation in laser wakefields by betatron oscillations (3) and the fast ignition variant of inertial confinement fusion (4). In the Fast Ignition (FI) scheme, Tabak et al. (5) proposed adding a longer intense pulse (duration ~ 100 ps) ahead of an ignition pulse in order to generate a channel in the underdense corona surrounding a fusion pellet in order to push the critical surface of the plasma closer to the dense core. This scheme has several advantages as compared to adding an external guide as in the cone-guided concept (6). It requires less sensitive target fabrication, and may therefore be easier to implement. It also decreases the cost of targets and may lead to more efficient coupling of laser energy to the core for fast ignition.

Relativistic channelling in underdense plasma has been studied both computationally (7) and experimentally (8). Different plasma densities, laser powers and pulse shapes have been considered for the process of plasma creation and channelling. In the high intensity regime ($a_0 \geq 1$), the ponderomotive force (9) and relativistic effects (10) dominate the laser plasma interaction. Theses forces can modify the refractive index of the plasma leading to self-focusing and filamentation. These studies also show that high intensity laser plasma interactions also leads to other detrimental instabilities, such as longitudinal modulation, induced by self focusing (11), and long wavelength hosing (12). Therefore an experiment to investigate these issues was conducted at the Rutherford Appleton Laboratory. The aim of the experiment was to study laser channelling in underdense plasma by laser pulses of comparatively long duration, emulating the one proposed by Li et al. (1), focused into a supersonic deuterium gas jet at various densities. It is shown that even when the laser power is below the threshold for relativistic self-focusing the ponderomotive force is able to create a longitudinally smooth channel.

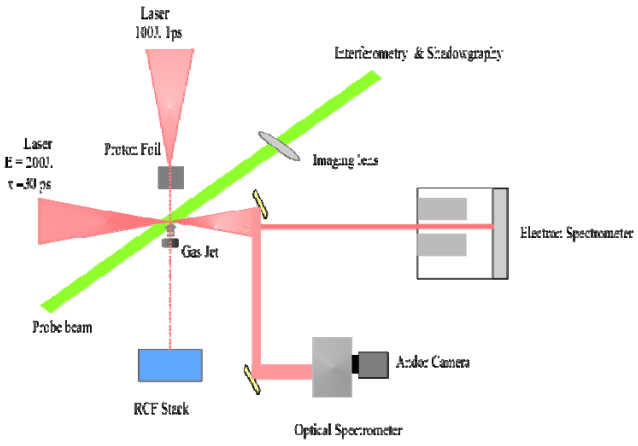

Figure 1 Sketch of experimental setup.

Experimental method

The experimental work presented here was conducted using the Vulcan laser at the Central Laser Facility at Rutherford Appleton Laboratories. The central wavelength of Vulcan is 1054 nm. For this wavelength, the non-relativistic critical electron density is $n_c = 1\times10^{21}$ cm^{-3}. The laser channelling experimental setup is presented in figure 1. In this experiment, plasma was produced by field-ionisation of the gas jet by the driver laser pulse itself. The laser pulse, of duration τ = 30 ps full-width half-maximum (E = 200 J, $I\lambda^2 = 3\times10^{18}$ Wcm^{-2}μm^{-2}), was focused at the edge of a supersonic, 2 mm wide deuterium gas jet. This compares to the Rayleigh range, $z_R \approx 2$ F $w_0 \sim 42$ μm, for a measured focal spot size of $w_0 \sim 5$ μm and *F*-number of F ~ 3. The focal spot contained about 35% of energy within a (FWHM) diameter of 7 μm.

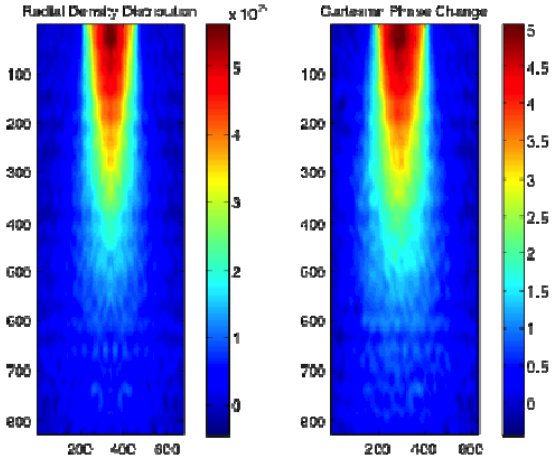

Figure 2 Phase and Radial density maps taken from 2mm nozzle at a gas line pressure of ≈ 30 bar

The neutral density profile was characterised before the experiment at Imperial College London using interoferometric techniques .(13). The resultant inferred density profile is shown in figure 2. The plasma electron density created in the gas jet density was varied by changing the backing pressure from 1 to 100 bar. This resulted, once fully ionised, in electron densities of 10^{18} - 10^{20} cm^{-3}, which is 0.001-0.1 times the critical density $n_{cr} = \varepsilon_0 m_e \omega^2/e^2$. The parameters ($P_L$= 6 TW) were such that the laser would exceed the threshold for relativistic self-focusing for a Gaussian laser beam ($P_L > P_{cr} = 17\,(n_{cr}/n_e)$ GW(14)) for an initial plasma density of $n_e \approx 2\times10^{18}$ cm^{-3}. Even below this threshold, guiding of the laser pulse can still take place due to ponderomotive effects alone.

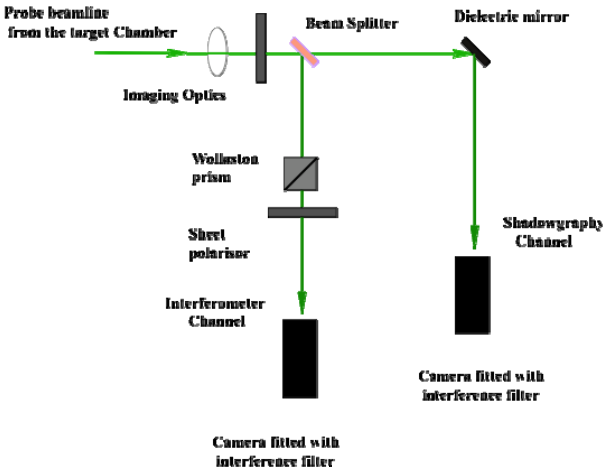

Figure 3 The probe beamline diagnostic channels showing the interferometry and shadowgraphy channels

In order to obtain interferograms and shadowgraphs of the plasma, a collimated frequency-doubled pulse of wavelength 532nm was directed perpendicularly to the interaction laser beam, and then sent into separate diagnostic channels using a beam splitter outside the chamber. The setup for shadowgraphy and interferometry is shown in figure 3. The rays of the optical probe beam are deflected by the refractive index of the plasma. Shadowgraphy gives information about the size of the deflecting plasma, whilst interferometry can give quantitative information on the density profile. By varying the timing of the pulse beam an examination of the plasma channel formation, in the form of a series of snapshots, was made possible.

The interaction was also diagnosed via proton radiography. A secondary laser pulse τ = 1 ps, of E ≈ 100 J, I = 10^{19} Wcm^{-2} interacted with a 20 μm thick aluminium foil to create a broad energy spectrum of protons. These were then directed through the interaction, to give spatial and temporal measurements of the plasma, by viewing the deflection of the protons by the plasma in different velocity ranges. This data has already been published in (15). The spectra of the transmitted light in the forward direction and accelerated electron emerging from the gas jet were also studied as shown in figure 1.

The collimated forward electromagnetic spectra coming out of the chamber was directed onto an optical spectrometer and then recorded with an Andor CCD camera. The accelerated electrons were measured in the direction of the laser propagation (i.e. at 0˚) by a magnetic spectrometer, which was placed outside the

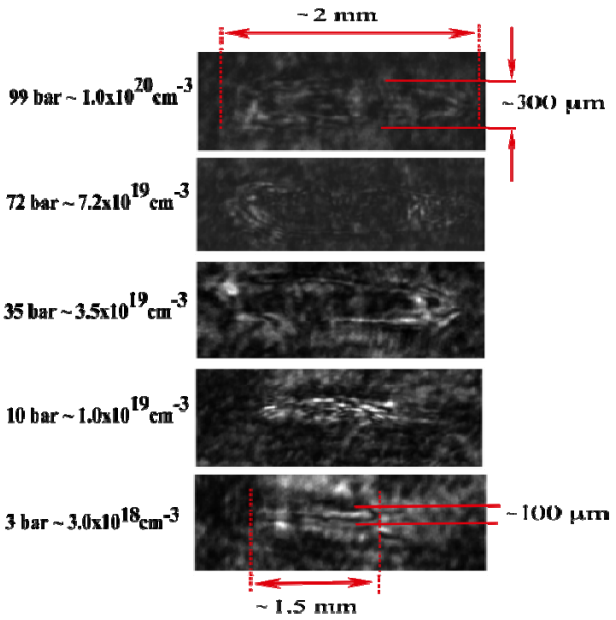

Figure 4 Images of plasma channel created in a deuterium plasma (with given densities) by 6TW, 30ps laser pulses.

main target chamber. After being deflected by the magnetic field the deflected electrons were recorded on image plates, which produce high-resolution 2D images of the dose deposited by the electrons passing through the detector plane. In order to convert the electron spectra from the image plate data, a tracking code written in Matlab was used. The field strength used enabled measurement of electrons with energies between 0 and 25 MeV.

Results and Discussions

Figure 4 shows five shadowgrams of the plasma formed on different shots of varying densities (from n_e = 3.0 × 10^{18} cm^{-3} - 1.0 × 10^{20} cm^{-3}) using 6 TW, 30 ps duration laser pulses. The images were taken 150 ps after the passage of the drive laser beam and in each case show an area of extended plasma formation, with relatively constant transverse profile, as would be expected if the laser was being guided through the plasma. A number of different techniques were used to remove unwanted spatial inhomogeneities in the probe images presented here. These types of problems arise from the imperfect spatial quality of the probe beam. However due to the poor beam quality, none of these methods can completely remove the unwanted noise.

At higher densities (~10^{20} cm^{-3}), the measured channel length is ~2 mm with diameter ~300 µm, and at lower densities (~3×10^{18} cm^{-3}) the measured length is ~ 1.5 mm with diameter ~ 100 µm. The calculated Rayleigh length (z_R = 42 µm), so for the given densities the channel length varied from (35 z_R - 45z_R) as shown in figure 4.

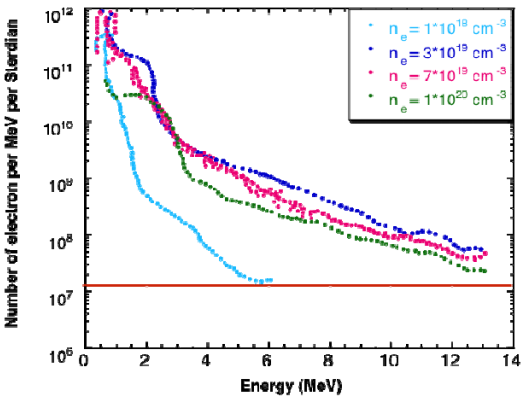

Figure 5 Electron spectra from 2mm nozzle, for various n_e.

Figure 5 shows electron spectra for different given densities n_e. They were fitted with a quasi-Boltzmann distribution function $n(E) = A \exp(-E/T_e)$ to define the temperature T_e in MeV. In these experiments, the spectra always exhibit two-temperature distribution. Therefore, the spectrum gives two characteristic temperatures, T_1 at low electron energy and T_2 for the higher energy electrons. Figure 6 is a representative shot, taken at a density of n_e = 6.4 × 10^{19} cm^{-3}, showing temperatures T_1^* ~ 0.6 MeV and T_2^* ~ 1.7 MeV.

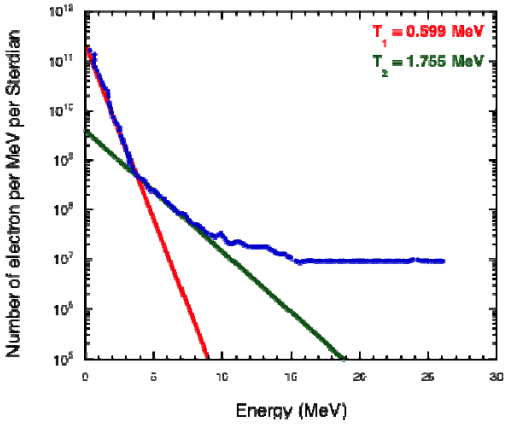

Figure 6 Electron spectrum plot at given n_e = 6.4 × 10^{19} cm^{-3} shows temperature fit T_1 and T_2 for low and high energy electron populations respectively.

Figure 7 shows the variation of the temperatures from the two-temperature fits to the electron spectra as a function of density. Surprisingly, there is only a weak correlation of the temperatures with density with the lower electron temperature in the range T_1 ~ 0.4-0.6 MeV, and the other in the range T_2 ~ 1.5–2 MeV. This is quite different from the case of hot electron production in the short pulse regime (τ < 1 ps) (16).

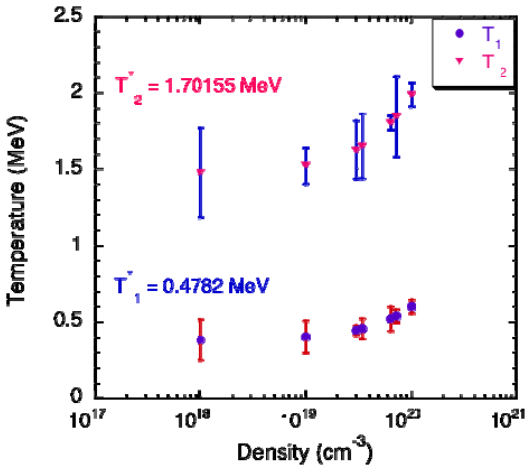

Figure 7 Electron temperatures in MeV at different pressures where T_1^* and T_2^* shows average temperatures over the given density range.

A typical transmitted light spectrum recorded during the experiment is plotted in figure 8. There were two clear peaks; one of them at the main laser fundamental wavelength of 1054 nm and a secondary peak corresponding to hydrogen line emission at 656 nm. There is also a possible signature of self-modulation at 900 nm, but at 3 orders of magnitude lower than the transmitted main laser pulse, one can see that the effect of self-modulation is quite small. Again this contrasts strongly with the case of transmitted laser spectra observed when using shorter laser pulses of similar power (17).

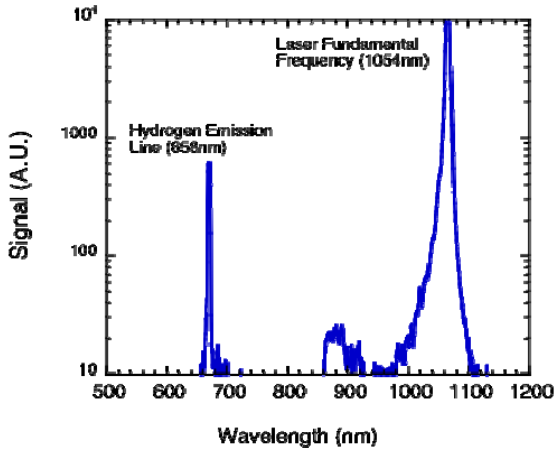

Figure 8 Forward Scatter Spectrum of deuterium gas for $n_e = 3 \times 10^{19}$ cm^{-3}. The spectrum exhibits a main maximum centered at the laser wavelength.

Conclusions

In conclusion, we have presented experimental observations of the propagation of high intensity 30 ps laser pulses through underdense deuterium plasma. Propagation was investigated by optical shadowgraphy and proton radiography. Here we have shown the formation of a straight, stable and long channel for low electron densities. At relativistic intensities, the ponderomotive force and relativistic effects will cause the laser pulse to self-focus. The effect of these two forces can guide the laser pulse through the plasma over many Rayleigh lengths ($35z_R - 45z_R$). The generation of energetic electrons (~ MeV) was also observed, but with relatively little dependence on density. This also implies that the formation of the channel has the ability to reduce instabilities associated with the propagation. Hence, the observed characteristics of the channel have implications for both laser wake field accelerators and fast ignition inertial confinement fusion.

Acknowledgements

The authors wish to warmly thanks to the staff of the Central Laser Facility for their invaluable help, support and discussions during the experiment.

References

1. G. Li et al., Laser Channeling in Millimeter-Scale Underdense Plasmas of Fast-Ignition Targets. Physical Review Letters. 100:125002 (2008).
2. M.I.K. Santala et al.,Effect of the Plasma Density Scale Length on the Direction of Fast Electrons in Relativistic Laser-Solid Interactions. Physical Review Letters. 84:1459 (2000).
3. S. Kneip et al., Observation of Synchrotron Radiation from Electrons Accelerated in a Petawatt-Laser-Generated Plasma Cavity. Physical Review Letters. 100:105006 (2008).
4. T.M. Antonsen et al., Self-focusing and Raman scattering of laser pulses in tenuous plasmas. Physical Review Letters. 69:2204 (1992).
5. M. Tabak et al., Ignition and high gain with ultrapowerful lasers@f. Physics of Plasmas. 1:1626-1634 (1994).
6. R. Kodama et al., Fast heating of ultrahigh-density plasma as a step towards laser fusion ignition. Nature. 412:798 (2001).
7. N. Naseri et al., Self-channelling of relativistic laser pulses in large-scale underdense plasmas. Physics of Plasmas. 17:033107-033111 (2010).
8. M. Borghesi et al., Relativistic Channeling of a Picosecond Laser Pulse in a Near-Critical Preformed Plasma. Physical Review Letters. 78:879 (1997).
9. J. Fuchs et al., Dynamics of Subpicosecond Relativistic Laser Pulse Self-Channeling in an Underdense Preformed Plasma. Physical Review Letters. 80:1658 (1998).

10. P. Kaw et al., Filamentation and trapping of electromagnetic radiation in plasmas. Physics of Fluids. 16:1522-1525 (1973).
11. V.K. Tripathi et al., Plasma effects in a free electron laser. Plasma Science, IEEE Transactions on. 18:466-471 (1990).
12. Z. Najmudin et al., Investigation of a channeling high-intensity laser beam in underdense plasmas. Plasma Science, IEEE Transactions on. 28:1057-1070 (2000).
13. S. Semushin et al., High density gas jet nozzle design for laser target production. Review of Scientific Instruments. 72:2961-2965 (2001).
14. P. Sprangle et al.,Laser wakefield acceleration and relativistic optical guiding. Applied Physics Letters. 53:2146-2148 (1988).
15. G. Sarri et al., Observation of Postsoliton Expansion Following Laser Propagation through an Underdense Plasma. Physical Review Letters. 105:175007 (2010).
16. S.P.D. Mangles et al., Electron Acceleration in Cavitated Channels Formed by a Petawatt Laser in Low-Density Plasma. Physical Review Letters. 94:245001 (2005).
17. A. Modena et al., Electron acceleration from the breaking of relativistic plasma waves. Nature. 377:606 (1995).

Characterisation of debris emission from PW laser solid interactions

Contact: *olivier.tresca@strath.ac.uk*

O. Tresca, D. C. Carroll, X. H. Yuan[1], M. Coury, R. J. Gray, M. N. Quinn, C. M. Brenner*, and P. McKenna

SUPA, Department of Physics, University of Strathclyde
Glasgow, G4 0NG, UK

K. L. Lancaster and D. Neely

**Central Laser Facility, STFC Rutherford Appleton Laboratory*
Didcot, OX11 0QX, UK

[1]*Current address: Key Laboratory for Laser Plasmas (Ministry of Education) and Department of Physics, Shanghai Jiao Tong University, Shanghai 200240, China*

Introduction

Understanding shrapnel and debris production in the interaction of ultra-intense laser pulses with solid targets is important to prevent damage to expensive optics and components positioned close to the target region. A number of experimental studies have been carried out at laser intensities in the range 10^{12}-10^{14}Wcm^{-2} for metallic targets [1-4]. The debris plume generated consists of mainly solid (shrapnel) or particulates with size in the 10s to 100s of micron range. The high energy shrapnel and debris generated is typically captured using gel cells and glass witness plates.

In this report we present measurements on the characterisation of debris from the front and back surfaces of solid irradiated by Vulcan PW laser pulses.

The experiment

The Vulcan PW laser generates pulses of light at a wavelength of 1.054 µm with duration of 0.7 ps. The pulse energy on target was 130 J, in a 3.8 µm spot (FWHM), giving an intensity of 4 x 10^{20} Wcm^{-2}. The laser incident angle was varied between 0° and 15° by rotating the target in its mount. A plasma mirror was positioned 3 cm from the target to enhance the intensity contrast of the laser pulses. Due to the small focal spot, the resulting shock expand spherically within the target.

Debris emission from several different target materials were investigated, including plain 100 nm-thick Cu foils and layered targets of Al-Cu-Al and Al-Cu-CH with thicknesses varying from 20 µm up to 1000 µm.

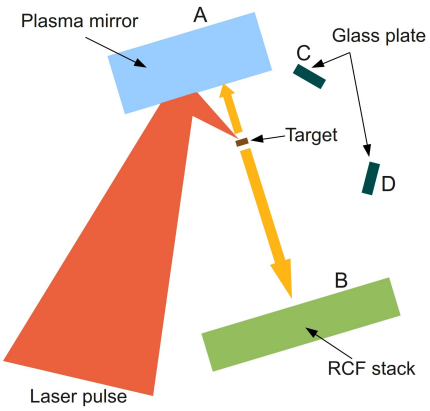

Figure 1: Experimental setup. Debris is collected on the plasma mirror witness plate and a shield positioned in front of the RCF stack.

Debris was collected using the plasma mirrors for the front surface emission, and the aluminium foil used to protect the RCF (dosimetry film) stacks for the back emission. The plasma mirrors are optical quality glass slabs of 2 cm by 10 cm, placed 3 cm in front of the target. A shield was placed in front of the plasma mirror to protect the unused surface from the debris emitted from the target. The aluminium shield positioned in front of the RCF stack is a 13 µm thick foil. It is positioned 5 cm from the target and the exposed area is 2.5 cm × 5 cm. In addition, glass witness plates were positioned to capture debris emitted in the laser specular direction and in the laser direction, at 5 cm from the target. Figure 1 shows the experimental set-up. The distribution of debris on the Al foil, plasma mirror and witness plates is characterised using a flat-bed scanner.

Direction of emission

Debris emission was collected in four directions with respect to the target: (A) the front normal direction (collected by the plasma mirrors), (B) the back normal direction (aluminium foil), (C) the laser specular reflection direction (glass plates), and (D) along the laser axis (glass plates), in Figure 1. Debris is consistently observed in positions (A) and (B), but no significant debris emission was recorded in directions (C) and (D), indicating that the main debris emission occurs along the normal direction of the target both at the front and at the rear.

To confirm this, the incidence angle of the laser on the target was varied between 0° and 15°. The targets (plain 100 nm Cu foils) were simply rotated and the position of the debris deposition measured with respect to the normal incidence case. The expected position of the debris deposition on the plasma mirror is also calculated assuming that the debris is emitted along the direction normal to the target. The results are shown in Figure 2.

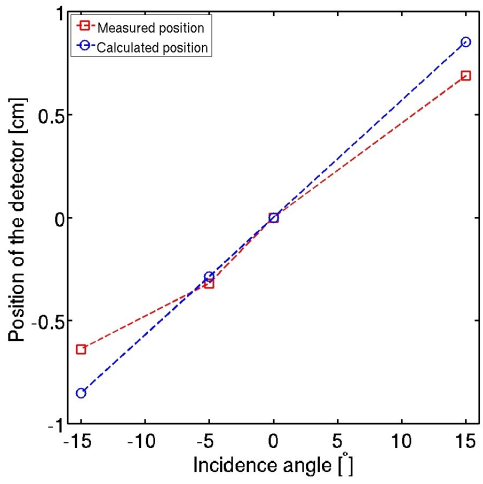

Figure 2: Front surface debris emission direction as a function of the laser incident angle, red symbols. Blue symbols, calculated position assuming that the debris is emitted along the target normal direction.

The negatives angles shown in Figure 2 represent a counter clockwise rotation of the target, if viewed from the top, and the positive angles a clockwise rotation. We can clearly see from Figure 2 that the measured debris position and the calculated one are in good agreement, confirming that the debris is principally emitted along the direction normal to the target.

Effect of target thickness on the back surface debris emission

Next we consider effects of varying the target thickness on the debris emitted from the target back surface (direction B). Two types of targets are used, *L* µm Al - 7 µm Cu - 1.5 µm Al, with *L* = 20, 100, 500 or 1000, and *L* µm Al - 7 µm Cu - 500 µm CH, with *L* = 20, 100 or 500.

As shown in Figure 3 (a), a clear increase in the maximum and average size of the debris particulate is measured with increasing target thickness, while the minimum size measured remains approximately constant. This is explained by the fact that the region of the target affected by the shock wave is larger for thicker targets, due to the lateral spreading of the shock. We also measured the density of the debris collected on the Al foil. The variations of the debris density with varying target thickness are shown in Figure 3 (b). A significant increase in the density of the debris measured with increasing target thickness is observed for the two target types used. This observation is consistent with an increasing area of the target surface being affected by the shock spallation as the thickness is increased.

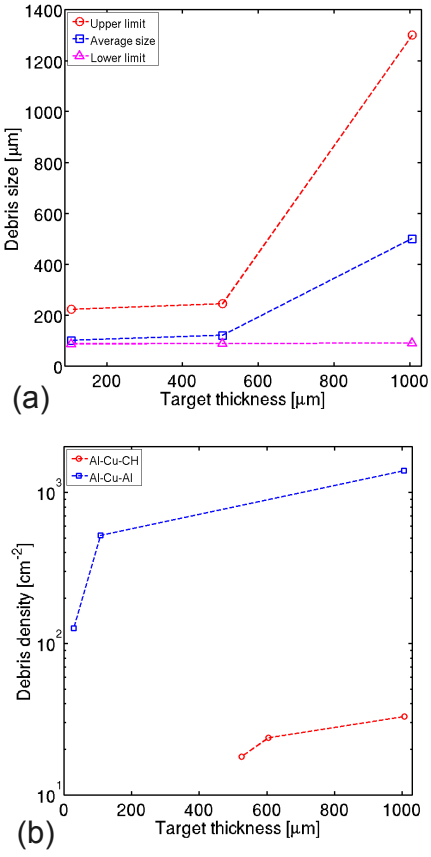

Figure 3: (a) Variations of the size of the debris particulate measured on the Al protective foil (direction B) with varying target thickness for the Al-Cu-Al type target. The red symbols show the largest debris diameter measured, the magenta symbols the smallest ones and the blue line represents the average size. (b) Variations of the density of the debris deposition on the Al foil with varying target thickness for the two target types.

Next we consider the angular distribution of the debris emitted in direction B for different target thicknesses, using the Al-Cu-CH target type. As shown in Figure 4(a), the debris is emitted in a ring-like distribution. The central region, containing only a small number of impacts is extending over a radius of ~1.5 cm and centred on the centre of the Al foil corresponding to the target normal direction. The debris is evenly spread across the ring over a width of ~0.5 cm and is concentrated in the apex region of the ring. Figure 4(b) shows a measure of the position of the impact with the origin taken in the bottom left corner. The solid lines are parabolic fit of the recorded positions and show good agreement with the data. The red solid line represents the best fit to the data, while the green and blue lines represent the boundaries of the width of the ring containing 95% of the debris impact.

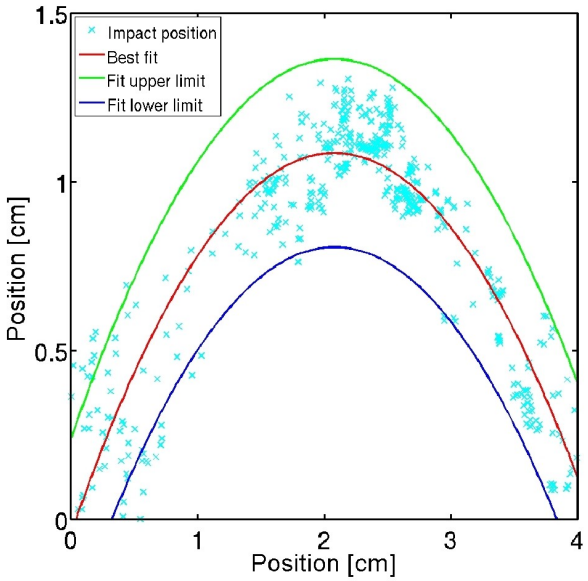

Figure 4: (a) Example of the measured debris distribution for a 600 µm thick target. (b) Record of the position of the debris impact, cyan symbol. The red solid line represents the best fit to the distribution; the blue and green lines are the limit of the area containing 95% of the impacts.

The debris particulate observed with this type of target seems to mainly result from liquid debris, as some of the craters formed are filled with solidified liquid droplets. The material embedded in the Al foil is most likely molten CH as it is the forming the back surface of the target.

Figure 5 shows the variation of the maximum radius of the debris distribution as a function of target thickness. The radius is measured in the horizontal direction using the different fits and taken at half the maximum width in the vertical direction. The red line corresponds to the radius measured with the best fit to the data, while the green and blue one correspond to the limit of the region containing 95% of the impacts. We can see from Figure 5, that the radius of the debris distribution increases linearly with increasing target thickness.

Assuming the divergence of the debris emitted by the spallation of the shock at the rear surface corresponds to the divergence of the spherical shock launched inside the target, and assuming a constant divergence of the shock wave, we measure a divergence half angle of approximately 16° using the data shown in Figure 5.

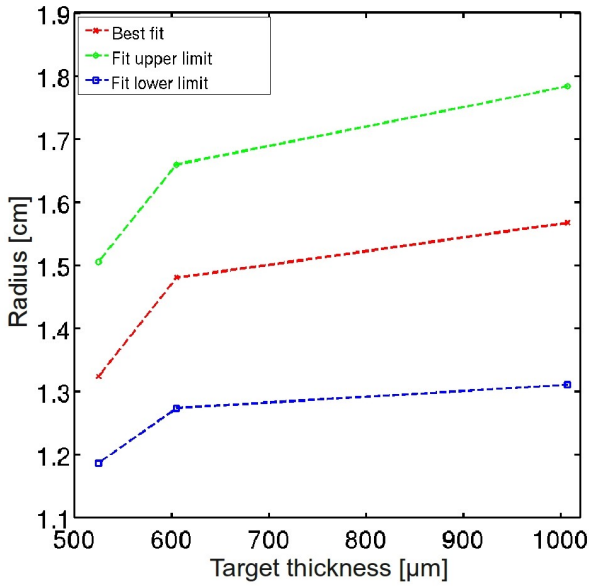

Figure 5: Debris impact distribution size as a function of the target thickness.

Buried layer ejection

As shown in Figure 6, large pieces of Cu can be found embedded in the Al foil when layered Al-Cu-Al targets are irradiated. The dimensions of the target is approximately 5 mm x 5 mm and the size of the shrapnel shown in Figure 6 is measured to be ~3.6 mm long. This indicates that most of the buried layer survives the interaction of the laser with the target and is ejected at high velocity in the target normal direction.

Figure 6: Cu shrapnel produced by a 100 μm Al – 7 μm Cu – 1.5 μm Al target embedded in the Al protective foil. The shrapnel is ~3.6 mm long.

Conclusions

We have reported on the characterization of particulate debris produced by PW laser pulse interactions with solid targets. It has been shown that the debris emission is mostly directed along the target normal direction, for both the emission coming from the front and rear surface. The size and density of the debris particulates increase with increasing target thickness. It was found that liquid debris is emitted in a ring like distribution centered on the target normal direction. The radius of this ring is found to increase approximately linearly with target thickness. This observation indicates a constant divergence of the debris corresponding to the divergence of the shock wave inside the target. The divergence half angle of the rear surface debris emission is found to be ~16°. It was also found that in the case of layered targets, large portions of the buried layer can survive the laser interaction and be ejected in the target normal direction.

Acknowledgements

The authors would like to acknowledge the expert support of the CLF staff. This work is supported by EPSRC (grant numbers EP/E048668/1 and EP/E035728/1) and the LIBRA consortium.

References

1. E. Lescoute *et al,* Appl. Phys. Lett. **95** 211905 (2009)
2. E. Lescoute *et al*, J. Appl. Phys. **108** 093510 (2010)
3. G. Morard *et al*, Phys. Rev. B **82** 174102 (2010)
4. T. de Rességuier *et al,* J. Appl. Phys. **102** 073535 (2007)

Exotic x-ray spectra from ultra-intense laser driven hollow atom transitions

Contact spikuz@gmail.com & nigel.woolsey@york.ac.uk

S. A. Pikuz and A. Ya. Faenov

Joint Institute for High Temperatures RAS, 13-2 Izhorskaya St, Moscow, 125412 Russia

T. Kämpfer, K. S. Schulze and I. Uschmann

Institut für Optik und Quantenelektronik, Friedrich-Schiller-Universitat Jena, Max-Wien-Platz 1, D-07743 Jena, Germany and Helmholtz-Institut Jena, Helmholtzweg 4, D-07743 Jena, Germany

C. R. D. Brown, S. F. James and D. J. Hoarty

AWE, Aldermaston, Berkshire RG7 4PR, UK

R. J. Gray and P. McKenna

SUPA, Department of Physics, University of Strathclyde Glasgow, G4 0NG, UK

N. Booth and K. L. Lancaster

Central Laser Facility, STFC Rutherford Appleton Laboratory, Didcot, Oxfordshire, OX11 0QX, UK

O. Culfa, R. J. Dance, A. K. Rossall, E. Wagenaars and N. C. Woolsey

York Plasma Institute, Department of Physics, University of York, York, YO10 5DQ, UK

Introduction

The fundamental science of high intensity interaction with atoms and molecules is a large and rich area of study with the relativistic regime ($I\lambda^2 > 10^{19}$ W cm^{-2} μm^2) remaining relatively unexplored. Hollow atoms are atoms or ions with an empty inner shell and occupied outer shell [1], and K-shell hollow atoms have an empty principal quantum number $n = 1$, innermost, shell. These exotic ions are short-lived and are created by K-shell double ionization with photon, electron or ion collisions, and in nuclear α, β, electron capture (EC) decays. Hollow atom states are of fundamental interest and an example of systems far from equilibrium. Double photo-ionisation is of great interest as the advent of intense, tunable free-electron lasers in the soft x-ray region offers the possibility of creating large populations of hollow atoms.

In an ultra-intense laser-target interaction, the laser electric field is of sufficient strength to generate double photo-ionisation of inner shells [2]. In addition, as the fast electron currents are intense, the creation of multiple inner-shell vacancies, i.e. hollow atoms, through electron impact may be significant offering new diagnostic opportunities [3].

Identification of hollow atoms in excited materials is possible using methods of high resolution x-ray spectroscopy (see for example [4]). Radiative transitions from multi-charged hollow atom ions leads to the generation of x-ray emission with the specific energy and differs from the x-ray emission energy radiated from ions with mostly populated inner shells. Analysis of spectra containing hollow atom lines is challenging yet possible using forefront methods of non-local-thermal-equilibrium (non-LTE) atom kinetics. This approach enables the determination of plasma parameters as well as a fundamental investigation of atomic properties of exotic atomic states (see for example [5]).

As hollow atom spectral emission is expected to lie close to resonance transitions, and be of much less intensity than lines, high performance spectrometers are essential. One of the key experimental requirements is the provision of spectroscopic diagnostics incorporating very high spectral resolution ($\lambda/\Delta\lambda \sim 3000$ or more), with reasonable spectral range and high luminosity.

Curved Bragg diffracting crystals, such as the Focusing Spectrometer with Spatial Resolution (FSSR) are ideal. The FSSR design [6] utilizes two aspects of a spherically bent crystal to serve as a highly resolving dispersion element with high luminosity and spatial resolutions.

In the plane of diffraction, Bragg's law determines the dispersion.

$$n\lambda = 2d_n \sin\theta_B,$$

where λ is the wavelength, n is the reflection order, d_n is the interplanar distance of the crystal for n-th order of reflection, and θ_B is the Bragg angle for the diffracting wavelength. The optical (focusing) properties of a spherical mirror, in the sagittal plane which lies perpendicular to the plane of spectral dispersion, is described by

$$1/a + 1/b = 2\sin\theta_B/R,$$

where R is the radius of curvature of the spherical surface, a is the distance between the source and the crystal and b is the distance from the crystal to the object plane (detector).

The combination of these aspects provides an instrument with very high spectral resolution ($\lambda/\Delta\lambda$ up to 10,000) with high luminosity and 1D or 2D spatial resolution. The spectral resolution is crystal or detector limited and the spatial resolution is usually detector limited.

Experiment

The measurements of the K-shell spectra were recorded on the Central Laser Facility Vulcan Petawatt at the Rutherford Appleton Laboratory [7]. The Vulcan Petawatt provides a beam using optical parametric, chirped pulse amplification (OPCPA) technology [8] with a central wavelength of 1054 nm and a pulse full-width-half-maximum (FWHM) duration of 0.7 ps. The OPCPA approach enables an amplified spontaneous emission (ASE) to peak-intensity contrast ratio exceeding 1:10^9 several nanoseconds before the peak of the laser pulse [9]. The laser pulse, with up to 160 J of energy on target, was focused with an f/3 off-axis parabola of focal length 30 cm. The maximum laser irradiance of 5×10^{20} W cm^{-2} was achieved with a laser focus containing approximately 30% of the energy in an 8 μm (FWHM) diameter spot. The horizontally polarized laser beam was incident on target at 40° from the target surface normal. The measurements reported here were from thin, 20 μm thick, foil targets of either aluminium (atomic number, Z =13) or chromium (Z =24) cut to 1 by 1 mm squares. The foils were attached to a target holder using 10 μm diameter copper stalks and a two-component epoxy adhesive.

A pair of FSSR spectrometers fitted with spherically bent mica (K_2O-$3Al_2O_3$-$6SiO_2$-$2H_2O$) crystals with a radius of curvature of R = 150 mm. The (002) crystallographic plane with $2d(n=1)$ = 19.840 Å was aligned to recorded K-shell spectra of multicharged Al and Cr ions, taking advantage of the high integrated reflectivity of mica in many orders. Both

spectrometers were aligned with the same target-to-crystal, crystal-to-detector distances at an angle of 45° to the target surface normal. One FSSR recorded emission from the front, laser irradiated surface, of the target the other from the rear surface of the target. The target-to-crystal distance of 558 mm led to a demagnification factor of 5.0 for the diffracting system in sagittal plane.

The FSSR spectrometers were aligned to observe Al K-shell spectra in 7.0 – 8.4 Å wavelength range (energy 1.47 – 1.77 keV) by operating in 2nd order of mica crystal (002) reflection. In 7th order this alignment was suitable for the 2.0 – 2.4 Å (5.16 – 6.2 keV) range, which corresponds to K-shell radiation from Cr. It is important to note that a mica crystal maintains high reflectivity at orders above 7th and continues to at least 12th order [10]. This needs accounting for as any measurement may contain a superposition of reflections from many orders and "spectrum" maybe composed of spectral components from different ions and ionisation states.

Background fogging and crystal fluorescence due to intense fast electrons was limited using a pair of 0.5 T permanent magnets that formed a slit 10 mm wide in front of each crystal.

Spectra were recorded on Kodak Industrex AA400 and Biomax MS photographic x-ray film. For our experiments, Biomax MS demonstrated a higher absolute sensitivity, however Industrex AA provided the best signal-noise ratio and for this reason this film was preferred. The x-ray film detector was made light tight using two layers of 1 µm thick polypropylene $(C_3H_6)_n$ coated with 0.2 µm Al, or with 25 µm thick beryllium foil. Additionally, Mylar $(C_{10}H_8O_4)$ filters of 1 to 13 µm thickness were used to reduce the noise level and to prevent the saturation of the x-ray film.

Spectral measurements

Figure 1 shows three aluminum K-shell spectra obtained from foil and buried layer targets. The spectra were recorded from the front surface of the target. The on target laser energy was similar in each shot and in the region of 160 - 170 J (the maximum available).

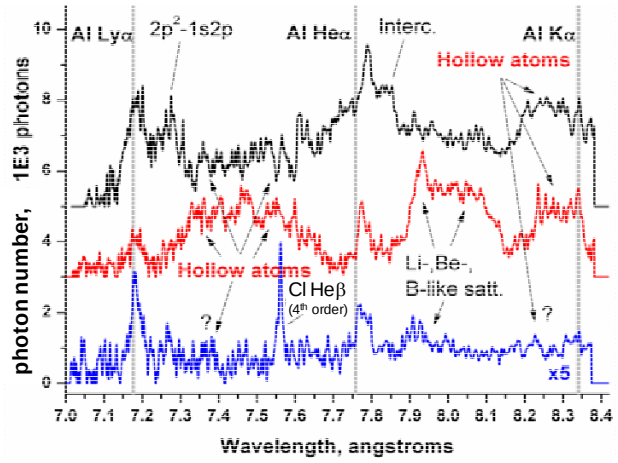

Fig 1. Aluminium K-shell spectra recorded using the FSSR spectrometer from the front (laser irradiated) surface. The upper (black), middle (red) and lower (blue) spectra show emission from a 20 µm thick aluminium foil, a 1.5 µm thick aluminium foil, and a 0.1 µm thick aluminium layer buried in 3 µm of n-type parylene respectively. The vertical lines (grey) indicate the Al Ly-α (7.17 Å) and He-α (7.76 Å) resonance line transitions and the aluminum K-α (8.34 Å) transition.

The figure consists of spatially integrated measurements taken from 3 different targets. A "thick" target (black line), which was a 20 µm thick pure aluminium foil, a "thin" target (red line), which was a 1.5 µm thick pure aluminium foil, and a "buried" target (blue line), which was 0.1 µm thick aluminium layer buried between two layers of 3 µm of n-type parylene (C_8H_8). The vertical axis shows the absolute number of photons. This information is extracted from the exposure level on film. The data is corrected for filter transmission, crystal aperture and reflectivity of the spherically curved mica crystal. Film, and film scanner sensitivity were also taken into account. This enables a comparison of the absolute and relative emission from each target.

The peaks in the spectra correspond to resonance transitions of H- and He-like ions of aluminium. The tabulated wavelengths for aluminium Ly-α (7.17 Å), He-α (7.76 Å) resonance lines and the K-α (8.34 Å) line are indicted by the vertical grey lines. The measured resonance line centres are shifted to longer wavelength with respected to the tabulated values by 10 and 20-25 mÅ. This is most likely due to multi-charged acceleration and following Doppler effect as demonstrated by K. Eidmann *et al*. and Andiel *et al*. [11,12].

Hollow atom spectral lines are anticipated in the spectral range between Ly-α and He-α resonance lines 7.17 to 7.76 Å, and also on the short wavelength side (blue edge) of the K-α line < 8.34 Å. For the case of the "thin" aluminium target, intense and broad spectral line groups are observed in these positions. These groups are indicated in Fig 1. Currently, there is no other explanation for these lines, as the spectral line positions do not match known transitions for any ionisation stage of aluminium with populated inner shells. Thus, we conclude that a large population of hollow atoms is created.

The "thick" aluminium target gives, as expected, the most intense spectrum. The hollow atom transitions identified in the "thin" target spectrum are clearly seen, although the intensity relative to the resonance transitions intensity is lower. In addition, the He-like $2p^2 - 1s2p$ satellite to the Ly-α, the He-α intercombination line are observed.

As the spectrum obtained from a "buried" target is weak in comparison to the "thin" and "thick" results, the intensity of the spectrum shown in Fig 1 has been multiplied by a factor of 5. The "buried" target spectrum shows hollow atom features, but of very low intensity and in some cases almost disappearing. The buried layer of aluminum is protected from direct laser radiation by a 3 µm plastic coating, suggesting that the observed hollow atom transitions are not due to the laser and may be due to fast electrons accelerated in the plasma at the front surface of the target. The intense hollow atom emission observed in the "thin" and "thick" targets suggest a preliminary conclusion that these hollow atoms are mostly likely generated by direct laser, or photonic, multiple ionisation, rather than by the impact with fast electrons.

The "buried" target data shows intense and narrow chlorine ($Z = 17$) He-β (3.79 Å) and He-γ (3.60 Å) lines in the region of hollow atom emission, the region between the aluminium Ly-α and He-α resonance lines. These lines are reflected from the 4th order of mica and are superimposed on the aluminium spectrum. The chlorine lines appear only in the "buried" target spectra suggesting this contamination is associated with the n-type parylene coating process.

Conclusions

Aluminium K-shell spectra showing intense hollow atom emission have been observed on the Vulcan Petawatt facility. The use of spherically curved crystal spectrometers enabled collection of good quality high spectral resolution data. A first analysis shows extremely intense hollow atom emission from simple aluminium foil targets, and for thin targets (1.5 µm), the hollow atom emission dominates the resonance line emission. The dominant hollow atom excitation process is probably due to direct laser ionisation of the inner electrons. In comparison, the laser does not interact with aluminium in a buried layer target. Measurement shows significantly weaker K-shell emission, and

the hollow atom emission is weak in comparison to the resonance lines. In this situation, hollow atoms excitation is probably due to fast electrons penetrating the target. This conclusion demands further investigation and interpretation supported with plasma and atomic kinetics physics simulations.

Acknowledgements

The authors acknowledge the expertise and help provided by staff of the Central Laser Facility. This work was funded by the UK Science and Technology Facility Council, the Engineering and Physical Science Research Council, and the Centre of Inertial Fusion Studies. OC acknowledges funding from the Turkish Government.

References

1. J. P. Briand *et al.,* Phys. Rev. Lett. **65**, 159 (1990)
2. J. Colgan *et al.*, Laser and Particle Beams 26, 83 (2008)
3. R. G. Evans *et al.,* Appl. Phys. Lett. **86**, 191505 (2005)
4. J. Dunn *et al.*, Rev. Sci. Instrum. **79**, 314 (2008)
5. J. Colgan *et al.*, High Energy Density Physics **6**, 295 (2010)
6. A.Ya. Faenov *et al.*, Physica. Scripta **50**, 333 (1994)
7. C. N. Danson *et al*.,, Laser Part. Beams **23**, 87 (2005)
8. I. N. Ross *et al.*, Opt. Commun. **144**, 125 (1997)
9. I. Musgrave *et al*., Appl. Optics **49**, 6558 (2010)
10. G. Hoelzer *et al.*, Physica Scripta **57**, 301 (1998)
11. K. Eidmann et al., JQSRT **65**, 173 (2000)
12. U. Andiel *et al.*, Europhys. Lett. **60**, 861 (2002)

---

[1] J. P. Briand et al., Phys. Rev. Lett. 65, 159 (1990)
[2] J. Colgan *et al.*, Laser and Particle Beams 26, 83 (2008)
[3] R. G. Evans *et al.,* Appl. Phys. Lett. 86, 191505 (2005)
[4] J. Dunn *et al.*, Rev. Sci. Instrum. **79**, 314 (2008)
[5] J. Colgan *et al.*, High Energy Density Physics **6**, 295 (2010)
[6] A.Ya. Faenov *et al.*, Physica. Scripta **50**, 333 (1994)
[7] C. N. Danson *et al*.,, Laser Part. Beams **23**, 87 (2005).
[8] I. N. Ross *et al.*, Opt. Commun. 144, 125 (1997)
[9] I. Musgrave *et al*., Appl. Optics **49**, 6558 (2010)
[10] G. Hoelzer *et al.*, Physica Scripta **57**, 301 (1998)
[11] K. Eidmann et al., JQSRT **65**, 173 (2000)
[12] U. Andiel *et al.*, Europhys. Lett. **60**, 861 (2002),